1.2 million years of climate change, globally and in the Mediterranean

Tiuri Konijnendijk

Promotor
Prof.dr. L. J. Lourens

Copromotor:
Dr. M. Ziegler

This work was financially supported by the Netherlands Organization for Scientific Research (NWO), under grant 865.10.001

1.2 million years of climate change, globally and in the Mediterranean

High resolution isotope stratigraphy from the Mediterranean reconciled with open ocean isotope chronologies and climate records

1,2 miljoen jaar klimaatverandering, mondiaal en in de Middellandse Zee

Isotopenstratigrafie in hoge resolutie uit de Middellandse Zee in overeenstemming gebracht met klimaatreconstructies van de wereldoceanen.

(met een samenvatting in het Nederlands)

PROEFSCHRIFT

ter verkrijging van de graad van doctor aan de Universiteit Utrecht
op gezag van de rector magnificus, prof. dr. G. J. van der Zwaan,
ingevolge het besluit van het college voor promoties in het openbaar te verdedigen
op dinsdag 25 augustus 2015 des ochtends te 10.30 uur

door

Theodoor Yuri Martijn Konijnendijk
geboren op 10 november 1985 te Rotterdam

Promotor
Prof.dr. L. J. Lourens

Co-promotor:
Dr. M. Ziegler

Examination committee
Prof. dr. David Hodell
University of Cambridge, United Kingdom

Dr. K. Grant
Australian National University, Australia

Prof. dr. D. Kroon
University of Edinburgh, United Kingdom

Prof. Dr. G. de Lange
Utrecht University, the Netherlands

Prof. Dr. G. J. Reichart
Utrecht University, the Netherlands

ISBN 978-90-6266-403-0

Published by Faculty of Geosciences, Utrecht University, the Netherlands, in:
Utrecht Studies in Earth Sciences (USES), ISSN 2211-4335

Cover: '*Ocean*' by Pawel Kuczynski. Used with the artist's permission.
Layout by T.Y.M. Konijnendijk, with thanks to Margot Stoete of GeoMedia

Printed in the Netherlands by CPI - Koninklijke Wöhrmann, Zutphen.

Copyright © 2015 T.Y.M. Konijnendijk

All rights reserved. No part of this publication may be reproduced in any form, by print or photo print, microfilm or any other means, without written permission by the author.

Utrecht Studies in Earth Sciences 91

1.2 million years of climate change, globally and in the Mediterranean

High resolution isotope stratigraphy from the Mediterranean reconciled with open ocean isotope chronologies and climate records

Tiuri Konijnendijk

Utrecht 2015

Faculty of Geosciences, Utrecht University

For everything there is a season, and a time to every purpose under heaven.

Ecclesiastes 3:1

Contents

1.	**Introduction and synopsis**	**1**
1.1	General introduction on climate change research	1
1.2	Astronomical cycles and the ice ages	3
1.3	Monsoons	5
1.4	The Mediterranean Sea	6
1.5	Ti/Al tuning	8
1.6	Problems addressed in this thesis and thesis outline	9
2.	**Chronological constraints on Pleistocene sapropel depositions from high-resolution geochemical records of ODP Sites 967 and 968**	**13**
2.1	Introduction	13
2.2	Material and Methods	14
2.3	Age model	16
2.4	Evaluation of the Late Pleistocene sapropel Chronology	21
2.5	Discussion	22
2.6	Conclusions	24
3.	**On the timing and forcing mechanisms of late Pleistocene glacial terminations: Insights from a new high-resolution benthic stable oxygen isotope record of the eastern Mediterranean.**	**29**
3.1	Introduction	29
3.2	Materials and Methods	33
3.3	Results	36
3.4	Discussion	42
3.5	Conclusions	48
4.	**On the timing of late Pleistocene terminations: Inferences from benthic $\delta^{18}O$ records of the Atlantic, Pacific, and Mediterranean basins**	**51**
4.1	Introduction	51
4.2	Materials and Methods	52
4.3	Results	54
4.4	Discussion	60
4.5	Conclusions	61
5.	**A new MedStack – 1.2 million year history of Eastern Mediterranean Hydroclimate**	**63**
5.1	Introduction	63
5.2	Materials and Methods	65
5.3	Results	69
5.4	Discussion	77
5.5	Conclusions	81

6. Methane variations on orbital timescales: a transient modeling experiment **83**
6.1 Introduction 83
6.2 Models and methods 85
6.3 Main sources and controls of wetland methane emissions 89
6.4 Summary, discussion and conclusions 95

Appendices **98**

References **108**

Samenvatting in het Nederlands **120**

Acknowledgements **125**

If you can't explain something to a first year student, then you haven't really understood it.

Richard Feynman

Chapter 1

Introduction

1.1 General introduction on climate change research

In this thesis I make a detailed reconstruction of climate changes based on materials from the Mediterranean Sea. Not only does this provide new insights in climate changes in the Mediterranean region, the aim is to improve our understanding of global climate changes as well. As we will come to see, the Mediterranean offers a rare combination of circumstances that enable us to better gauge the age of major climatic shifts in Earth's past.

In this first chapter, I provide very general background information on climate change, the research area and time frame, methodology, and terminology. The following chapters each have a more detailed and specific introduction of their own. A short summary of the main scientific findings is provided in Dutch at the end of this thesis.

1.1.1 Climate change in the Pleistocene

This thesis is a discussion of the earth's climate of the last 1-1.5 million years (Ma). The studied interval, from the Middle to Late Pleistocene, is one where climate was dominated by large ice sheets in the high latitudes growing and melting away again: the so called ice ages. During warmer periods (interglacials) the ice sheets and mountain glaciers retreated and global conditions were similar to those we have today. During the colder periods (glacials), ice sheets and glaciers expanded to cover large areas in northern Europe, Siberia (the Eurasian ice sheet) and North America (the Laurentide ice sheet). This had dramatic effects on the rest of the climate system, with vegetation retreating to the warmer lower latitudes, and greatly affecting precipitation patterns and temperatures on land. In addition, sea levels dropped significantly, up to 120 meters below current levels in the coldest of glacials, and ocean currents (e.g. the Warm Gulfstream) were changed, stopped, or relayed, and their individual characteristics were different from today.

The climate of the past have left traces in the environment that we can use to reconstruct the circumstances that created them. Deep sea sediments form an exceptionally rich archive of past climate change. Their relatively stable position, with only the slowest of currents, allows for usually undisturbed deposition of particles sinking down from the water column. Dust blown in from the land and clay carried by rivers form the base of a slow but continuous rain of new material on the ocean floor. This material can, under the right circumstances, be very informative about conditions on earth. Within the sediment, all sorts of organisms can be found living on the seafloor mud, and in it, as well as in the water above it. When an individual organism dies, it sinks down to the seafloor and is buried, conserved until such a point where a scientist takes a sediment core in order to study it.

All these species of marine organisms adapt, in a number of ways, to the changes in environment over time. Things like the temperature of the water, the salt content, etc. have effects on the composition of the calcite in shells of these creatures that we can measure. In absence of someone holding a thermometer and telling us the result, we therefore use methods as measuring the calcite composition of creatures, as a *proxy* for climatic change millions of years ago.

1.1.2 $\delta^{18}O$: a method to study climate in the past

A very common proxy for paleoclimate is the $^{18}O/^{16}O$ composition of calcium carbonate ($CaCO_3$) in the shells of unicellular organisms called foraminifers. This method measures how much of the common isotope of oxygen (^{16}O, with 8 protons and 8 neutrons in the atomic core) is present versus the relatively rare isotope ^{18}O (with 8 protons, but 10 neutrons in the core). The ease with which ^{18}O is incorporated in the calcite is dependent on temperature (Epstein et al., 1951). This feat was used by Emiliani (1955) in his groundbreaking work, showing that *changes* in the $^{18}O/^{16}O$ ratio relative to present or $\delta^{18}O$, can therefore be used to reconstruct changes in temperature in the oceans.

Since then, the amount of ice present on the earth's poles and in the giant ice caps of the Pleistocene have also been found to have an effect on the $\delta^{18}O$ recorded in foraminifer calcite (Shackleton and Opdyke, 1973). Water (H_2O) carrying the lighter isotope ^{16}O is more easily evaporated than its heavier counterpart. The snowfall accumulating to form glaciers comes from this water that evaporated from the oceans, and the ice sheets and glaciers are therefore composed primarily of the lighter isotope, ^{16}O. If the ice sheets grow large enough, the effect on the $^{16}O/^{18}O$ composition of water becomes noticeable, and it is recorded in foraminifer calcite. Salinity of the water also has an effect on ^{18}O-incorporation in the calcite. All of these effects generally point in the same direction during ice ages: more (fresh water) ice, lower temperature and saltier oceans all direct towards a higher $\delta^{18}O_{calcite}$. Although it can be quite a puzzle how much of the change must be attributed to any which effect. NB: for ease of interpretation, the scale of $\delta^{18}O$ is usually printed upside down, with higher values representing lower temperatures and/or sea levels.

Foraminiferal $\delta^{18}O$ records generated over the last decades have provided us a wealth of insight into changes in the earth's oceans over millions of years of geologic time. Especially the calcite of foraminifers living in the deep sea, where temperature and salinity changes are limited, records changes in global ice volume well (Shackleton, 1987). The method has been so successful that benthic (bottom dwelling) isotopes are now commonly used to correlate different records to each other. By aligning the fluctuations in the $\delta^{18}O$ record of various sites, you can be fairly sure you are looking at the same time frame. To this end, Lisiecki and Raymo (2005) established a stack of 57 benthic $\delta^{18}O$ records from the Atlantic, Pacific and Southern Oceans. This stack gives a valuable picture of climate change: local signals (temperature etc.) are averaged out, and a long, high resolution global climate record is the result. It provides a worldwide framework which serves as a reference for new records. Of course, there are also drawbacks to this approach, which I will explain in more detail later in this introduction and in this thesis. One problem is the still limited spatial coverage: the Atlantic is well represented and the Pacific (in the low latitudes) as well. But the Mediterranean, the Indian Oceans are lacking, as well as a number of other sites. Also, while the age estimates for the climate changes recorded in the LR04 stack (Lisiecki and Raymo, 2005) are considered fairly robust, there is no good independent method of checking them, and their age model can be refined and/or revised.

1.1.3 A unique climate record from the Mediterranean Sea

This thesis focuses on the Mediterranean Sea. This ancient basin is a remnant of the Tethys Ocean that connected the North Atlantic and West Pacific Ocean before the Indian and African continents moved towards Eurasia. We (my co-authors and I) have generated a long (1.4 Ma) record representing regional and global climate circumstances using deep sea sediments from the eastern Mediterranean, just south of Cyprus. These sediments were recovered using a drill ship during a mission of the Ocean Drilling Program in 1995, at ODP Sites 967 and 968.

Although the Mediterranean is studied intensively, no-one before has generated such a long term, high-resolution $\delta^{18}O$ record before. We set our unique findings in the context of the existing research based on sediments from this region, but we also use our benthic $\delta^{18}O$ record to comment on the global isotopic stratigraphy, and the import of the Mediterranean therein. The setting of the record makes it ideal for our purpose, because it provides an additional method of estimating the age of the recorded climate changes. But studying this basin also has its own downsides, all of which will be described in the next sections.

1.2 Astronomical cycles and the ice ages

1.2.1 First evidence for episodic ice ages

Geology was practiced in the early 19th century as a pastime for the well-to-do with a lot of free time, such as second sons of noblemen and church ministers. It became more of a science with the publication of Charles Lyell's *Principles of Geology* in 1830, a book which amongst others inspired Darwin on his voyage with the Beagle. With the advent of proper geological practice, evidence mounted that giant glaciers must have episodically covered large parts of the American and Eurasian continents in the not-too-distant geological past (Louis Agassiz, in a succession of publications and speeches, in conjunction with others). The question what controlled the growth and decay of these ice sheets has occupied (and baffled) scientists ever since.

The first to suggest that the ice ages had something to do with variations in the earth's orbit was Joseph Adhémar. He was familiar with the precessional cycle (see next section), which had been known since the ancient Greek astronomers, and argued that if the timing of winter coincided with the far point in earth's elliptical orbit each year, this would make winters colder and promote the growth of ice sheets. James Croll expanded upon this idea and included the notion that a surface covered with white snow would reflect more solar irradiation (*insolation*) back to space, hence reinforcing the cooling effect (a so called *positive feedback loop*). All of these theories assumed that winter temperature is driving the changes in ice volume. Yet none of these theories could fit the astronomical cycles to the evidence well enough to satisfy all the data.

It was Milutin Milankovic who first came up with the correct solution in his 1930 text "*Mathematische Klimalehre und Astronomische Theorie der Klimaschwankungen*". He argued that it is not winter insolation that drives the ice ages: it is the summer insolation. On the one hand, a cool winter preserves ice sheets, but it also limits the amount of evaporation and in consequence snowfall and ice accumulation as well. On the other hand: the summer insolation controls the rate of melting, and this relation is much stronger. A few degrees warmer summer provokes an exponential increase in the amount of ice that melts, strongly reducing the size of the ice sheets. Milankovic calculated the development of earth's orbit over the past 650,000 years and showed how the ice ages related to the changes in insolation resulting from this develepment, especially around 65°N latitude where the Laurentide and Eurasian ice sheets are positioned. Although his theory has been refined, this work forms the foundation of the astronomical theory of the ice ages.

1.2.2 the astronomical cycles

The Milankovic theory describes three elements that affect the orbit of the earth; each element acts on its own time scale. A simple illustration (figure 1.1) will help with this short introduction of the topic. It shows the orbit of the earth around the sun. The orbit is not circular but elliptical; hence the distance of the earth to the sun is different depending on the time of year. It also shows that the earth's north-south axis is not perpendicular to this orbit. There is a certain degree of tilt,

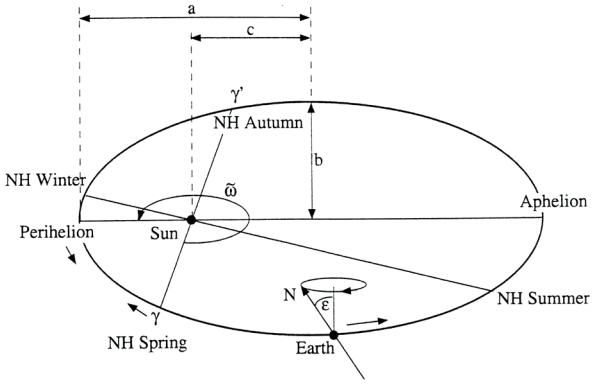

Figure 1.1: the orbital parameters of the earth (from Paillard, 2001).

or obliquity. This tilt of the earth's axis is why we experience the four seasons over the year. If the North end points towards the sun, it is summer on the Northern Hemisphere. Half a year later, the earth is at the other end of the sun, and the North end is pointed away from the sun: winter. The figure indicates that the north end currently points to the upper left, which is the direction of the pole star (hence the name). However, this direction changes over time, just like a spinning top on a table does, and given enough time the axis will be pointing towards completely different stars. This process, which takes ~25,000 times round the sun (or 'years') for a full cycle, is called the *precessional motion* of the axis, and it affects the timing of the seasons. If summer and winter coincide with the position of the earth in the far and near end of the earth's orbit, this influences the amount of sunlight during summer/winter, which is what Adhémar was referring to in the previous section. Note that precession is defined so that minimum precession is the situation where the 21st of June – midsummer´s day for the Northern Hemisphere – coincides with the shortest distance to the sun (perihelion: see figure 1.2). So *minimum* precession corresponds to a *maximum* summer temperature at 65°N, and the terms 'precession minimum' and 'insolation maximum' are used interchangeably.

The second variable affecting earth's insolation is the obliquity. This is a measure for how far the angle of the earth's axis is tilted. Right now, this angle is ~23.4°, which is the latitudinal distance between the tropics and the equator, and how far the polar circles are away from the poles. In the past, this angle has varied between ~22.0° to 24.5°, with an average period of 41,000 years. A higher angle implies more pronounced seasonality: warmer summers and colder winters.

The last variable is eccentricity, a measure for how elliptical the earth's orbit is. Although this doesn't make a lot of difference for how much total sunlight is received by earth over a whole year, it affects the distribution between when the earth is close to the sun and when it is far away. In combination with precession it is therefore a powerful factor controlling summer insolation at 65°N. The eccentricity of the earth's orbit varies on timescales of ~100,000 years between almost circular (allowing little precession influence) and ε=0.06, or quite ellipsoid (allowing pronounced precession influence).

1.2.3 Astronomical tuning

The ideas of Milankovic were expanded upon by André Berger (1978), and later Jacques Laskar (1993, 2004) who, with the aid of computers, calculated the orbits of all the planets in the solar system and their gravitational influences on each other to great detail. Using the work of Cesare

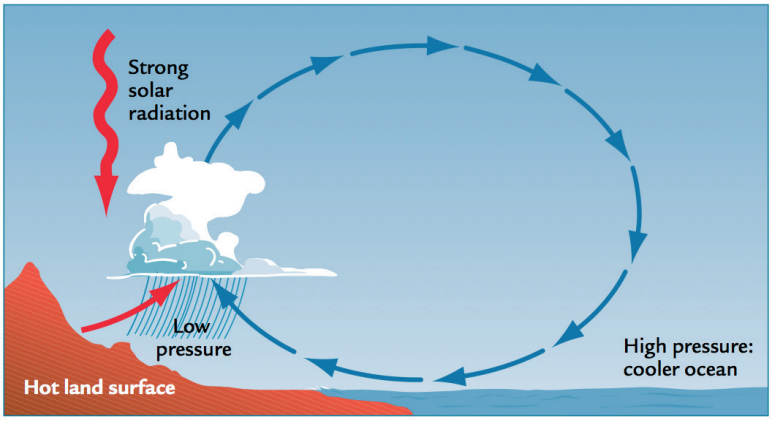

Figure 1.2: schematic representation of a monsoon system (from Earth's Climate: Past and Future, 3e by William F. Ruddiman, Copyright 2014 by W.H. Freeman and Company. Used by permission of the publisher.)

Emiliani and the relation of $\delta^{18}O$ with the global ice volume/climate, the link between these and the astronomical cycles was decisively shown by Hays et al. (1976). Since then, comparing the behavior of $\delta^{18}O$ records to summer insolation at 65°N has been common practice and is often still the easiest and most accurate way of estimating the age of the record, with precision within few thousand years of uncertainty millions of years back in the geologic past.

1.3 Monsoons

Naturally, the ice sheets are not the only part of the climate system sensitive to variations in insolation. An important part of the climate in lower latitudes are the monsoon systems that govern rainfall in especially North Africa and India, and to a lesser degree China, the Amazon and the North American farm belt. Here I will briefly explain how monsoon systems work, and how they are affected by Milankovic cyclicity, because the North African monsoon is of great importance for our study site in the Mediterranean.

On a year to year basis, every area in the world is affected by the seasons: they warm up in summer and cool down in winter. The areas that undergo yearly monsoons are all areas that have large landmasses near the tropics on one side of the equator (like India), and ocean on the other side of the equator (the Indian ocean). A monsoon is, simply put, a system with strong winds carrying rain from the ocean to land in summer, and a reversed pattern in winter (Ramage, 1971). This phenomenon is the result of the different heat capacity of land versus sea (figure 1.2).

In summer the land warms up much faster than the water in the adjacent ocean, which needs to absorb a lot of energy before heating substantially. This results in a strong contrast between warm land versus cool ocean surfaces. The warm air over land starts to rise higher into the atmosphere, and is replaced with moist air from the adjacent ocean. This carries a lot of moisture to the warm continent. The warm, moist air rises up to where pressure is lower and the atmosphere is much cooler. This causes the moisture to precipitate, resulting in lots and lots of rain. The low molecular weight of water (a molecule of H_2O weighs less than a molecule of N_2 or O_2) only reinforces the effect because it makes it easier for moist air to rise. At the end of summer, evaporation over land slows down and the monsoon system stops: the system reverses in winter, when the air over land is significantly colder than the ocean.

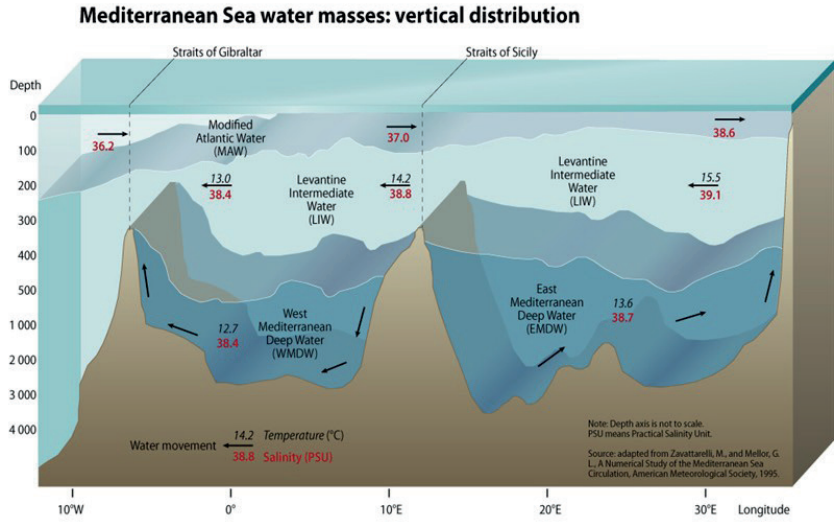

Figure 1.3: sea water masses in the Mediterranean (credit: GRID-Arendal)

Considering the importance of summer insolation for a monsoon, it is not hard to see how the Milankovic cycles can affect the working of this system. In fact, around ~9,000 years ago, when the great northern ice sheets were rapidly melting away, the North African monsoon was enhanced by the precession cycle so much that most of what is now the Sahara Desert was covered with vegetation and likely inhabited by early prehistoric human settlements (Larrasoaña et al., 2013).

1.4 The Mediterranean Sea

1.4.1 Oceanographic basics of the Mediterranean

The Mediterranean basin is a semi-enclosed basin that is only connected to the open (Atlantic) ocean through the narrow and shallow Strait of Gibraltar. Because of the low latitude setting, water evaporates from the basin faster than it precipitates back: a net evaporation of ~600 mm (Mariotti et al., 2002). This means sea level would drop rapidly if it weren't for additional water sources. Limited fresh water comes in from the Rhône and Po rivers as well as from the Black Sea through the Bosporus. More fresh water is carried by the Nile from the south, but most of all: surface water from the Atlantic Ocean flows in through the Strait of Gibraltar (figure 1.3). As this Atlantic surface water flows eastwards it undergoes evaporation, which removes water but conserves the salt. The salinity of the surface current therefore increases until it reaches its maximum near Israel and the Levant, in the eastern Mediterranean. the surface water cools during winter and becomes denser, sinks down to form Levantine Intermediate Water (LIW), flowing back into the rest of the basin between ~200-500 meters depth (Wüst et al., 1961). This process brings oxygenated surface water down in the Mediterranean water column. The LIW is cooled further by cold winds from the European mainland blowing over the Adriatic Sea, where it sinks further down and forms Eastern Mediterranean Deep Water (EMDW).

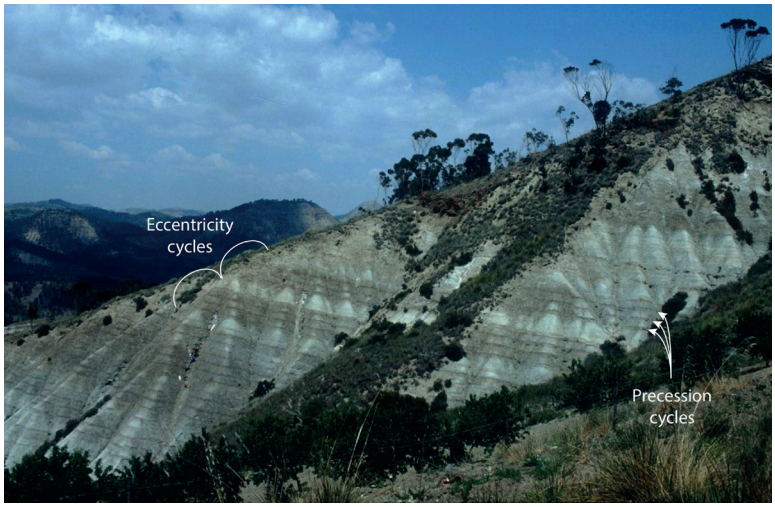

Figure 1.4: regular sapropel deposition in the Mediterranean at the Gibeliscemi section, Italy (photo credit: Luc Lourens)

1.4.2 Monsoon influence on Mediterranean deep water formation and sapropels

The first step of deep water formation takes place in the easternmost part of the Mediterranean basin. This is also the region where the Nile delivers its discharge of fresh water. While recently this discharge has been quite modest (especially since the construction of the Aswan Dam), it is significantly enhanced when an amplified monsoon causes increased rainfall over the Nile source area. It has been hypothesized (Rossignol-Strick, 1985) that enhanced outflow of the Nile river could disrupt the formation of LIW. The fresh water is less dense than the seawater, and flows over it instead of immediately mixing. This can create a lid covering the Mediterranean surface water and preventing it from sinking and cooling down. The result would be an interruption of deep water formation, stopping the advection oxygenated water to intermediate and deep parts of the basin. This is called the Nile Hypothesis of sapropel formation (Rossignol-Strick, 1985: Rohling, 1994), and it explains why there are episodic depositions of black, organic rich layers in the Mediterranean called *sapropels*.

During the deposition of sapropels, organic matter that sinks down from the surface ocean is no longer broken down before it is buried under the sediment. This could point at an increased organic matter flux, but that is unlikely in the oligotrophic (food limited) Mediterranean. Instead, it is probably due to reduced oxygen supply – like a stop in deep water formation – which kills everything in the deep sea and limits the breakdown of organic material.

These sapropels occur with such regularity (figure 1.4) that a link to astronomical cycles seems obvious, and the Nile Hypothesis neatly explains both the occurrence and the regularity of the depositions. With the understanding of the mechanism behind sapropels came the realization that they can also be used to estimate age. Hilgen (1991) made a detailed tuning of Pleistocene sapropels to astronomical precession, and refined the age estimates for several reversals of the earth's magnetic field – which had until then been important age markers themselves for many scientific studies. Lourens et al. (1996) showed the role of obliquity, and demonstrated that the sapropel deposition pattern fits the astronomical variables best if they respond to insolation with a delay of ~3,000 years. This agrees well with the most recent sapropel ("S1"), which has been 14C-dated: it

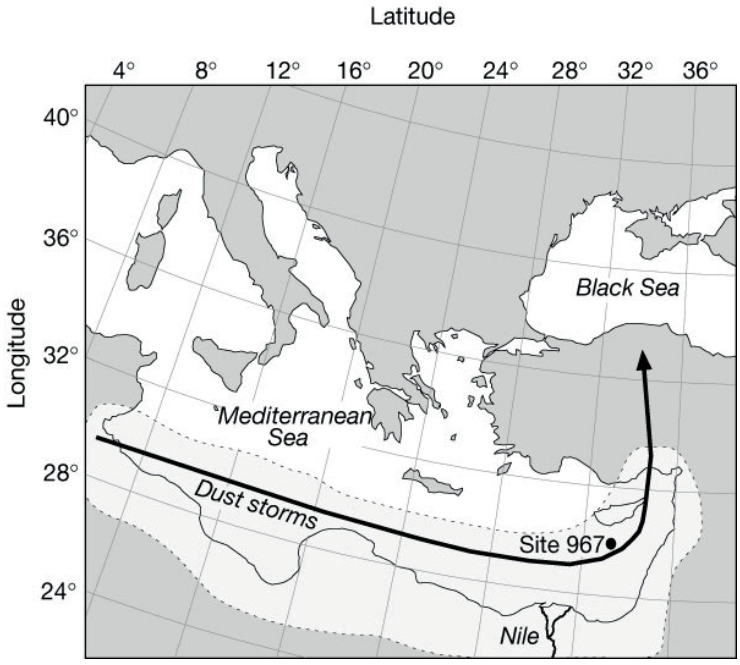

Figure 1.5: Both dust storms and the nearby Nile river delta influence our study sites (ODP Sites 967 and adjacent Site 968; after Lourens et al., 2001)

was deposited between 6,200 and 10,800 years ago (de Lange et al., 2008). This means the average (8,500 years ago, or 8.5 ka) lags 3,000 years (3 kyr) behind the most recent insolation optimum (11.5 ka). This lag is inherently part of the system and represents how fast the monsoon responds to insolation, and how long it takes for the deep sea to become anoxic. Tuning sapropels to insolation is considered so reliable, that the sapropel age model underpins part of the official chronology for the Neogene (Gradstein et al., 2004).

1.5 Ti/Al tuning

The advantage of our study site in the eastern Mediterranean extends one step further than isotopes and sapropels. The location puts it in the way of storm tracks over the Mediterranean, carrying Saharan dust from the North African continent which is deposited in the sediments of our drill site (Lourens et al., 2001). On the other hand, most of the deposits here come from sediments carried by the river Nile (figure 1.5). However, the windblown dust is enriched in a number of elements compared to the river clay (Wehausen and Brumsack, 2000). Elements like iron and titanium are present in the windblown dust, while all but absent from the clay minerals that make it to our study site in the deep sea near Cyprus. Using the ratio of titanium to aluminum (or Ti/Al) therefore indicates how much windblown dust reaches our site, versus to total (mostly river carried) sediment.

During the enhanced monsoons, when the astronomical configuration is right, there is much more vegetation covering the Sahara preventing erosion of the soil. This means that less dust (and associated titanium) is available for pickup and transport. Meanwhile, the Nile river discharge is

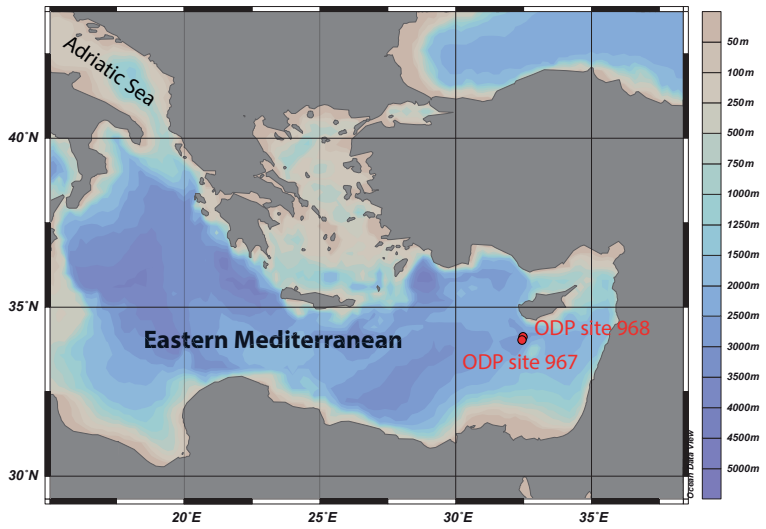

Figure 1.5: the position of ODP Site 967 (2,554m depth) and Site 968 (1,961m depth) in the eastern Mediterranean

enhanced, carrying aluminum-rich clay to the sea. That means that the Ti/Al ratio is a decent proxy for activity of the North African Monsoon in relation to astronomical climate forcing. In fact, Lourens et al. (2001) show that this ratio has an almost linear response to summer insolation at 65°N during the Early Pleistocene and Pliocene at this site.

We measure the titanium and aluminum content of the sediments at ODP Sites 967 and 968 and tune the ratio to insolation. This provides a direct estimate of monsoon activity (rather than the indirect estimate of sapropel deposition, which is a proxy for anoxic conditions in the deep sea). With that, we have a robust new method of estimating the age of our entire record. This gives us the unique opportunity to comment, not only on the existing estimates for sapropel deposition, but also on the age of changes in the benthic $\delta^{18}O$ record and how fast the ice sheets respond to insolation.

1.6 Problems addressed in this thesis and thesis outline

In the next chapter I will discuss how I created a single record from the data of ODP Sites 967 and 968 (figure 1.6). The process of creating an age model and tuning the Ti/Al ratio to insolation is explained in detail. Then, the age of the sapropels in our record according to the Ti/Al age model is presented, and the previously available sapropel age model (Emeis et al., 2000; Lourens et al., 2004) is revised.

In chapter three, I present our high resolution benthic $\delta^{18}O$ record for the last 1.2 Ma. I compare the Mediterranean record with the LR04 benthic stack of open ocean records. I discuss the age of major changes in our record and how they compare to LR04 estimates based on direct tuning of the isotope changes to insolation. Uncertainties and drawbacks of a benthic isotope record in the Mediterranean are also covered.

In chapter four, I briefly address the issue of local influences on $\delta^{18}O$ records, and how the signal of rapid deglaciation is propagated differently at each site. The focus lies on the last deglaciation, and I compare our deep Mediterranean site to a close by benthic $\delta^{18}O$ record that

bathed by LIW to reconstruct each water mass separately. Special attention goes to the question whether the Mediterranean $\delta^{18}O$ reflects the signal of deglaciation (in terms of temperature as well as ice volume) in the same way as the open ocean records. This is important for the question if we can use a Mediterranean $\delta^{18}O$ record to comment on the open ocean stack of LR04 at all.

In chapter five, I present a revision of the MedStack record of Lourens et al. (2004). This is a compilation of planktic $\delta^{18}O$ records reflecting surface ocean salinity, temperature, and global ice volume for the last 5.3 Ma. We have added the very high resolution records of ODP Sites 967 and 968, which improves both the resolution and spatial coverage of the stack for the last 1.2 Ma. In addition, the Ti/Al age model improves our understanding of the changes and removes some inaccuracies. I compare the Mediterranean deep sea record to the surface ocean record, commenting on freshwater signals during sapropels and several other features.

Chapter six is more of a stand-alone paper. It is the end result of a climate modeling study using results from Climber-2, a low resolution climate model with great potential for paleoclimate research. Because of its robust setup but low resolution it can be run over long timescales, simulating global climate. Despite the low resolution, large scale systems like monsoons are captured quite well (Braconnot et al., 2007). I use the model run (representing 650,000 years of climate change) to simulate the existence of wetlands on the Eurasian continent versus the monsoon areas. I simulate the production of CH_4 – an important greenhouse gas – in these wetlands, and compare them to the data of atmospheric CH_4 concentrations found in air bubbles of the Antarctic ice cores. The paper is different in the sense that it is a global climate modeling study. It is connected to the rest of this thesis in the sense that it addresses monsoon behavior on Milankovic time scales.

Find a watch in the desert, and you can infer the existence of a watchmaker.

William Paley

Chapter 2

Chronological constraints on Pleistocene sapropel depositions from high-resolution geochemical records of ODP Sites 967 and 968

We completed and merged an existing high-resolution X-Ray Fluorescence (XRF) data set derived from Ocean Drilling Program (ODP) site 968 with new data from adjacent ODP site 967. An astronomical age model spanning the last 1.05 Myr was constructed for the spliced record using the highly linear relation between the elemental ratio of titanium and aluminum in the sediment (Ti/Al) and insolation. This rendered detailed ages for sapropel deposition in the Eastern Mediterranean. Our results imply major revisions of previous sapropel age models below MIS 11, with changes of up to two precession cycles in the interval ~450-850 ka of the ODP 967 sapropel chronology. Based on the Ti/Al age model, we find that color reflectance – used as an indicator for sapropels in this interval of ODP site 967 and 968 – is highly incongruent with the Ti/Al proxy as well as insolation forcing during periods of minima in the 405 kyr eccentricity cycle. Our findings indicate that the use of color reflectance as a proxy for so-called ghost sapropels in these intervals is not reliable. Lastly, we demonstrate the presence of a strong obliquity signal in the Ti/Al record that lags obliquity forcing by 4 ± 0.7 kyr. This time lag is only marginally longer than the adopted 2.7 ± 1.1 kyr for the dominantly precession-tuned age model, and is hence much shorter than the generally accepted ice sheet response time to insolation forcing. This suggests that the obliquity-bound changes in Ti/Al are not glacial controlled and most likely reflect changes in low-latitude climate oscillations, such as the monsoon.

published as: Konijnendijk, T., Ziegler, M., and Lourens, L., 2014. Chronological constraints on pleistocene sapropel depositions from high-resolution geochemical records of ODP sites 967 and 968. *Newsletters on Stratigraphy*, Vol. 47/3, 263–282. DOI: 10.1127/0078-0421/2014/0047

2.1 Introduction

Sapropel deposition occurs periodically in the Mediterranean Sea (Rossignol-Strick, 1983; Hilgen, 1991; Lourens et al., 1996). This process is paced by the precession cycle of the Earth's rotational axis, and is thought to occur as a result of stagnating circulation in the Mediterranean basin through increased stratification. A freshwater cap at the surface of the Mediterranean Sea during sapropel formation is commonly linked to increased discharge from the river Nile, resulting from increased amount of rainfall in the Nile's catchment area through an intensified North African Monsoon (NAM) (Rossignol-Strick 1983). Sapropels occur mainly in the eastern Mediterranean

and are used as tools for correlating sediment cores and for studying Mediterranean climate and ocean circulation (e.g. Lourens, 2004).

The link between sapropel formation and the precession-bound periods of high summer insolation at the Northern Hemisphere allows us to establish accurate age depth relationships of sediment cores and land-based sections. This method is the principle behind the astronomically tuned time scale for the late Neogene (Hilgen et al., 1993; Lourens, 2004). Accordingly, the stratigraphic midpoints of sapropels are tuned to maxima in the June 21st 65°N insolation curve with a lag of 3000 years (3 kyr) to obtain an age model (e.g. Hilgen, 1991; Emeis et al., 2000; Lourens, 2004). The 3 kyr time lag is based on ^{14}C AMS dating of the Early Holocene sapropel S1, the midpoint of which falls at 8.5 ka – 3 kyr behind the corresponding insolation maximum at 11.5 ka. This lag is assumed to be inherent to the processes behind sapropel formation and is commonly kept constant when tuning sapropels to insolation (Lourens et al., 1996; Emeis et al., 2000).

The astronomical tuning of sapropels to insolation can be tested by comparing the resulting age model to that derived by other methods. For instance Lourens et al. (1996) validated their sapropel tuning by comparing planktic foraminiferal stable oxygen isotope results with those of benthic foraminifera derived from the open ocean. In addition, Lourens (2004) and Ziegler et al. (2010) evaluated the late Pleistocene sapropel chronology against the results of amongst others Langereis et al. (1997) by using tephras, magnetochronology and a number of other proxies. In this paper, we elaborate on the tuning strategy of Ziegler et al. (2010) by extending the high-resolution geochemical data sets of ODP Site 968 and merging them with new data from ODP Site 967 over the past 1050 ka. Unfortunately, the interval at ODP site 968 below core A3 is heavily disturbed, forcing us to incorporate the adjacent site, ODP 967, for a continuous record. The tuning approach is based on elemental ratios in the bulk sediment composition, which reflect regional climate. The resulting data provide an alternative, independent age model for the cores involved and will be used to test and evaluate previous sapropel chronologies (e.g. Emeis et al., 2000; Lourens, 2004).

2.2 Material and Methods

Our study uses data from ODP Sites 967 and 968 (figure 1.6) from the Eastern Mediterranean. ODP Site 967 (34°04'N, 32°43'E) was drilled south of Cyprus; near the Eratosthenes seamount at a water depth of 2,554 m. ODP 968 (34°20'N, 32°45'E) was drilled on the Eratosthenes seamount at a water depth of 1,961 m (Emeis et al., 1996).

2.2.1 Revised splice 967 section

The splice of ODP 967 (table 2.1, figure 2.1) is a revision of the original splice created by Sakamoto et al. (1998). The revised composite depths (rmcd) that are used in this paper will thus differ from previously published data of ODP 967. To enable comparison, we list shipboard meters below sea floor (mbsf) as well as rmcd here. The topmost 30 mbsf of our splice contains only minor deviations.from the Sakamoto splice. These are of little consequence because we incorporated only data From ODP Site 968 in this part of the composite (section 2.2.2). The changes to the initial splice become more substantial, however, below 30 mbsf. Notably, below the interval of core B4 ending at 29.38 mbsf our splice reverts to core C4 at 29.56 mbsf (33.05 rmcd), rather than core A4, which was heavily sampled in prior studies. At 36.10 mbsf (39.72 rmcd) our splice jumps from core C4 to core B5 at 35.68 mbsf. Here it rejoins the initial splice for a short interval, though at 40.56 mbsf (44.56 rmcd) it jumps to core C5 at 39.52 mbsf, 260 cm above the point of the initial splice.

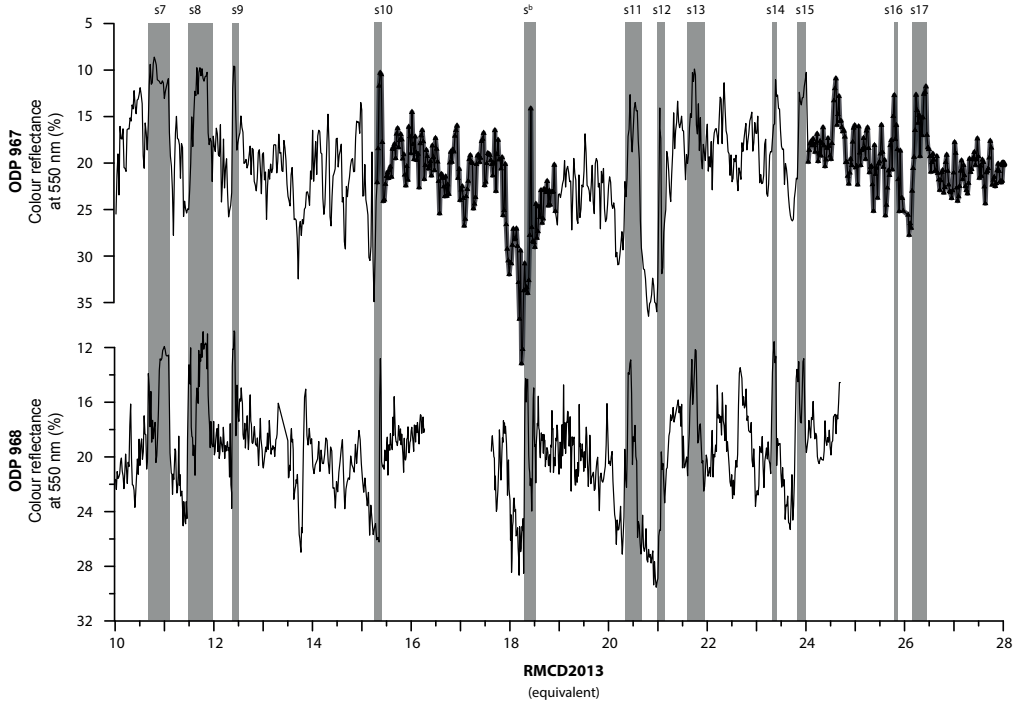

Figure 2.1: the color reflectance records of ODP cores 967 and 968, set to core 967 RMCD (equivalent). The sampled interval in core 967 to complete the existing 968 record is indicated with a thick line and markers. Sapropels as defined by Emeis et al. (2000) are marked with grey bars.

2.2.2 Composite section 967/968

In order to merge the existing data obtained from ODP 968 with the new data of ODP 967, the shipboard color reflectance (CR) data was used to align the cores. The reflectance values at 550 nm of the separate splices were plotted on the revised composite depth scale of ODP 967 (appendix I and II; figure 2.1). The wavelength 550 nm is typically indicative of organic matter content and is therefore useful in detecting nutrient cycles (Emeis et al., 1996). This proxy exhibits ample variability that is largely similar up to minute details in both cores due to their proximity.

Tie points, such as sapropels, were identified (Appendix III). The ODP 968 data was transferred to a new depth scale by fitting characteristic features to ODP 967 and applying linear interpolation between tie points (table 2.1). In a next step we identified the interval in ODP 967 that covered the gap between ODP 968 cores A2 and A3, and sampled it with sufficient overlap to tie the records of ODP 967 and 968 together. Characteristic features in Ti/Al and Ba/Al were used to determine the splice tie points between data from ODP 967 and 968. Similarly, the lowest part of ODP 968 A3 was identified in ODP 967 and sampled with overlap. This resulted in a single, continuous record through the combination of the two sites. The result is a splice of the combined ODP cores (figure 2.1; table 2.1).

2.2.3 XRF measurements

The combined splice of ODP 967 and 968 was sampled at 2 cm intervals. The samples of 3-5 grams were freeze-dried and then ground and homogenized. The powdered sediment was placed

Table 2.1: the combined splice of ODP 967 and ODP 968 cores. Rmcd depth values are according to the revised splice for ODP 967 as presented in appendix I and II. For ODP 968, the rmcd values represent their ODP 967 analogue depth

site	hole	core	sect	Top (cm)	Depth (mbsf)		site	hole	core	sect	Top (cm)	Depth (mbsf)	depth (rmcd2013) ODP 967 (equivalent)
968	A	1w	1	10	0.1								0.71
968	A	1w	5	80	6.8	-->	968	B	2w	1	54	5.94	5.39
968	A	2w	4	38	13.88	<--	968	B	2w	6	144	14.34	12.36
968	A	2w	7	80	18.8	-->	967	C	2H	4	30	14.3	16.14
968	A	3H	1	4	18.54	<--	967	C	2H	5	22	15.72	17.62
968	A	3H	CC	20	28.34	-->	967	A	3H	4	16	23.46	24.70
967	B	4H	1	114	25.44	<--	967	A	3H	6	114	27.44	28.70
967	B	4H	4	58	29.38	-->	967	C	4H	1	106	29.56	33.05
967	B	5H	2	38	35.68	<--	967	C	4H	6	10	36.1	39.72
967	B	5H	5	74	40.54	-->	967	C	5H	2	2	39.52	44.50
967	B	6H	2	114	45.94	<--	967	C	5H	5	148	45.48	51.10
967	B	6H	5	94	50.24								54.95

in a furnace and heated stepwise to 100˚C, 450˚C, 550˚C, 800˚C and 1000˚C. At each interval the relative weight loss was measured to obtain residual water content, organic matter content and carbonate minerals, respectively. The residue of this treatment was then made into glass beads for XRF scanning. 600 mg of the sample powder was mixed with 6000 mg lithium tetraborate ($Li_2B_4O_7$), and fused to glass beads. The beads were analyzed by a Philips PW 2400 X-ray spectrometer. Analytical precision was determined by parallel analysis of one international standard (ISE 921) and one in-house standard to be better than 2% for Al and Ti.

2.3 Age model

2.3.1 0- 340 ka

To create a detailed chronology for the composite ODP967/968 record we made stepwise improvements to the initial age model of Lourens et al. (2004), who correlated sapropel midpoints to their inferred 65˚N summer insolation maxima, including a fixed 3-kyr time lag. We followed Ziegler et al. (2010), who dated the youngest 350 ka of the record in detail by correlating the remarkable similarity between variations in CR and the ratio of titanium versus aluminum (Ti/Al) in ODP 968 to the speleothem oxygen isotope ($\delta^{18}O_{speleothem}$) records of the Sanbao/Hulu caves (Wang et al., 2008). The Ti/Al in the sediments at ODP sites 967 and 968 is considered to be determined by two major sources: Nile River suspended matter and windblown dust (Wehausen and Brumsack, 2000; Lourens et al., 2001). Because the suspended particles that contain titanium

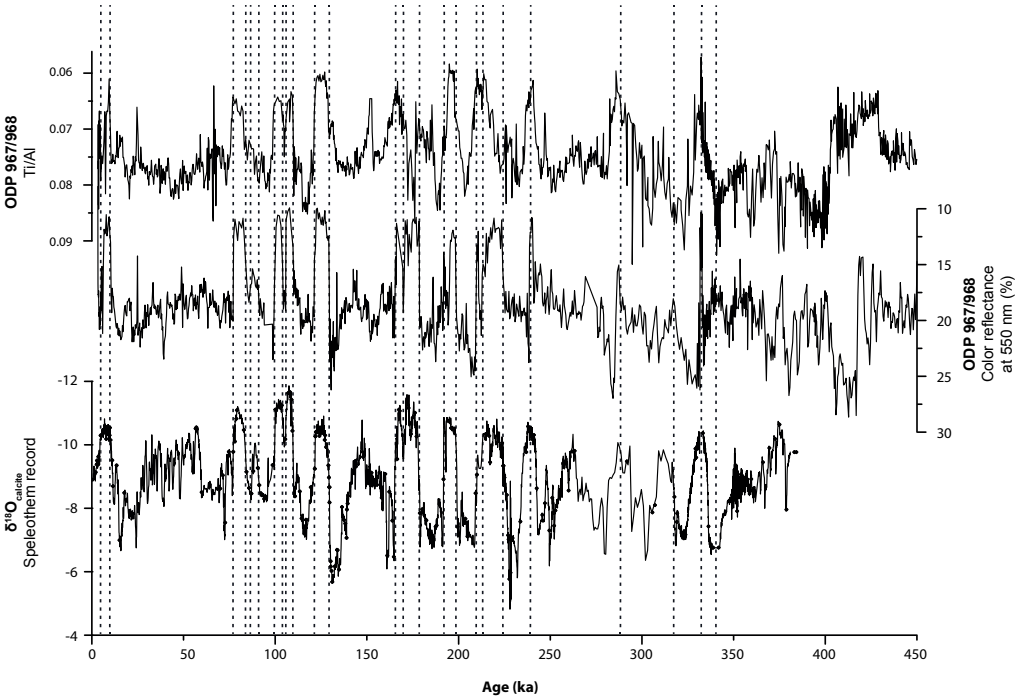

Figure 2.2: Age model construction for the interval 0-340 ka of the composite Ti/Al record, tuned to the U/Th dated speleothem record of Cheng et al. (2009). Dashed lines indicate tie points between the records. Black dots in the speleothem record indicate U/Th dates

will be heavier, they will be preferentially deposited close to the river mouth. The river derived sediment in ODP site 967 and 968 will therefore have been depleted in titanium before deposition at the drill sites, and the titanium in the sediment will therefore be predominantly of aeolian origin. Windblown dust is estimated to contribute between 65% and 95% of the titanium in the sediment (Lourens, 2001). The aeolian input depends on the availability of dust for windblown transport from the Northern Sahara. This is mainly controlled by vegetation cover of the surface (Ehrmann et al., 2013) in a tight relation with North African precipitation (Claussen et al., 2013). The observed Ti/Al changes at ODP sites 967 and 968 are therefore linked to monsoonal-induced humidity changes in Central to North Africa.

The $\delta^{18}O_{speleothem}$ record of Wang et al. (2008) reflects primarily insolation-driven monsoon activity in East Asia and is yet one of the best U-Series dated climate records covering the past 340 ka. As such, this record can be used to constrain leads and lags in the climate system to astronomical forcing and hence to test the assumed 3-kyr time lag between monsoon intensity and the formation of Mediterranean sapropels.

Figure 2.2 shows the correlation between the Ti/Al and color reflectance records of ODP 968 to the U/Th-dated $\delta^{18}O$ record of the SB-Hulu speleothems (Ziegler et al., 2010). The tuning is straightforward for the upper 340 kyr. Frequency and cross-spectral analysis using Analyseries (Paillard et al., 1996) reveals that the 23kyr signal in the speleothem record, and hence the Ti/Al record, lags 21 June 65°N insolation by about 2.7 ± 1.1 kyr, which means the 3-kyr lag adopted by Lourens et al. (1996) is within error.

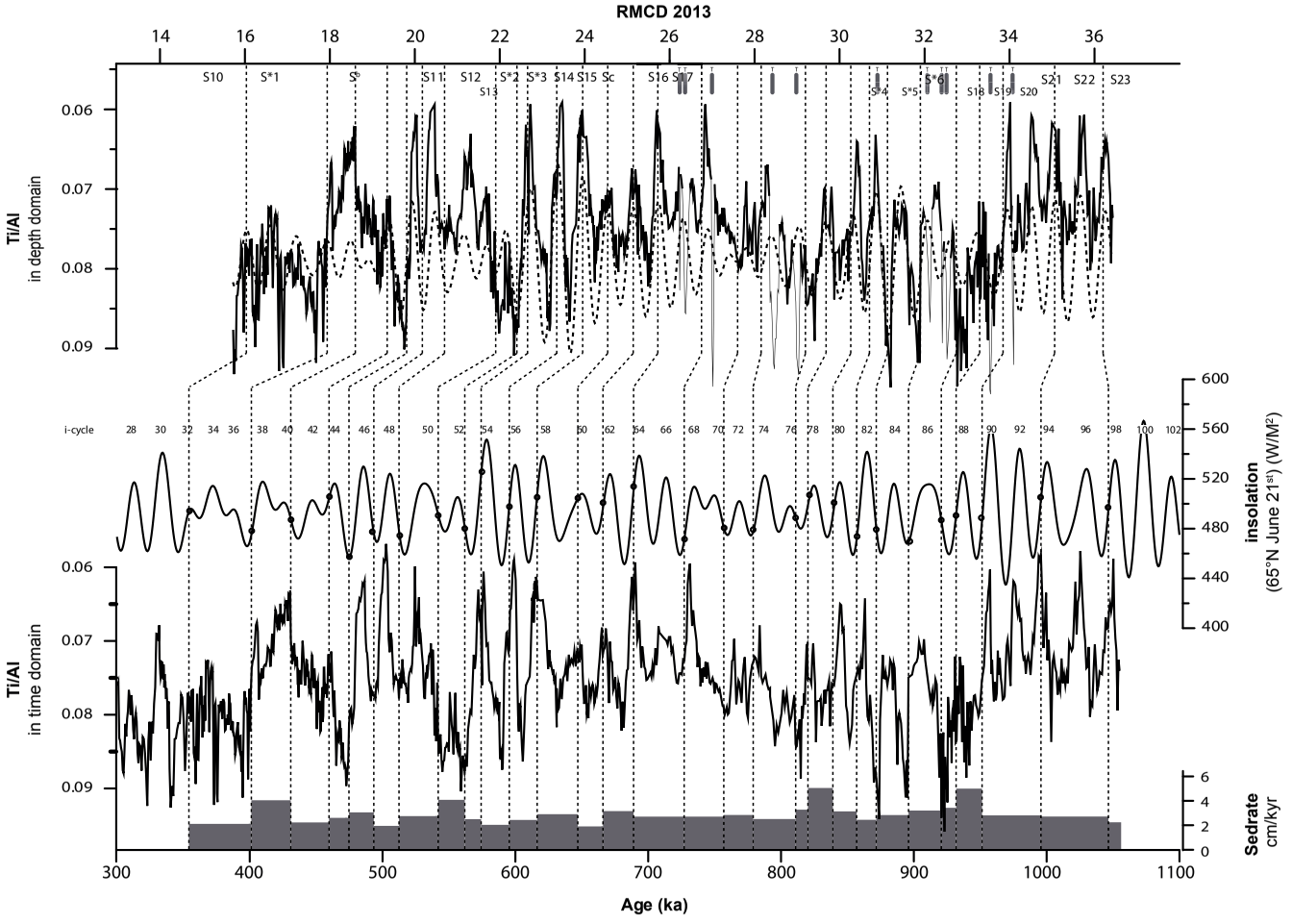

Figure 2.3: age model construction for the interval 340-1050 ka of the Ti/Al record matched to 65°N June 21st insolation. The filtered dominant signal in the depth domain (dashed line; top) was used to mathematically determine midpoints or, alternatively, maximum slope. Dashed lines connect the tie points in the records from depth to time domain. Variations in the record are tied to the insolation target curve with a 2.7 kyr lag. Where the dashed lines cross the insolation curve, closed dots indicate a midpoint was used, open dots for slope. Grey vertical bars at the top indicate turbidites. Note that in the bottom Ti/Al record, turbidites are removed from the data.

Rossignol-Strick and Paterne (1997) suggested the 3-kyr time lag between the S1 and the Holocene insolation optimum was partly explained by the occurrence of the Younger Dryas cold spell, delaying deglaciation warming and triggering cold, dry conditions in the Mediterranean region at that time – adversely affecting vegetation development. Ziegler et al. (2010) accordingly argued that the phase lag found in the Late Pleistocene African monsoon response to insolation results from North Atlantic cold spells, associated with Heinrich events. They reasoned that the lag would most likely be smaller or absent in the Early Pleistocene as the ice caps were smaller and the cold spells were less intense and less frequent. The timing of this proposed shift is still largely uncertain.

A Ca/Sr-based proxy for ice rafted debris (IRD) of the North Atlantic ODP Site U1308 showed for instance that the occurrence of Heinrich events was most likely negligible prior to ~650 ka, whereas proxies for IRD low in carbonates (of different source area), such as Si/Sr, revealed however that Heinrich events occurred until at least ~1350 ka (Hodell et al., 2008). At present we cannot exclude the possibility that this mechanism might have influenced monsoon climates throughout the Pleistocene and we therefore choose to keep the 2.7 kyr lag constant for the tuning of our record prior to 340 ka.

Table 2.2: tie points used to define the age/depth relation for the combined splice.

depth (rmcd2013) ODP 967 (equivalent)	Target age	Correlated feature	depth (rmcd2013) ODP 967 (equivalent)	Target age	Correlated feature
0			16.0	354.5	mid i-cycle 32
1.06	5.1	top s1	17.9	401.5	end i-cycle 38
1.25	10.2	bot s1	18.6	431.2	mid i-cycle 41
4.18	77.3	top s3	19.4	460.0	mid i-cycle 44
4.44	83.9	bot s3	19.8	475.0	end i-cycle 46
4.53	86.6	top prec s3	20.2	494.0	end i-cycle 48
4.77	91	bot prec s3	20.7	513.0	mid i-cycle 49
5.19	99.6	top s4	21.9	542.5	onset i-cycle 50
5.26	104	bot s4	22.4	562.5	mid i-cycle 53
5.37	105.9	top prec s4	22.7	574.8	mid i-cycle 54
5.42	109.7	bot prec s4	23.3	596.0	mid i-cycle 56
7.16	121.4	top s5	24.0	617.0	mid i-cycle 58
7.77	129.5	bot s5	24.5	646.0	mid i-cycle 60
9.41	165.5	top s6	25.1	667.0	mid i-cycle 62
9.65	169.8	dip s6	25.7	689.0	mid i-cycle 64
9.84	178.5	bot s6	26.7	728.0	end i-cycle 68
10.67	191.9	top s7	27.6	758.0	mid i-cycle 71
11.1	198.5	bot s7	28.2	780.0	end i-cycle 74
11.47	209.5	top s8	29.2	812.0	onset i-cycle 76
11.65	213	dip s8	29.7	821.5	mid i-cycle 78
11.88	224.1	bot s8	30.3	840.0	end i-cycle 80
12.38	239	mid s9	30.7	857.2	end i-cycle 82
13.88	288	mid s*	31.1	871.7	mid i-cycle 83
14.94	317	onset i-cycle 28	31.9	897.2	onset i-cycle 85
15.36	332	mid s10	32.8	922.0	end i-cycle 87
15.73	340	onset i-cycle 30	33.3	933.0	mid i-cycle 88
			33.8	952.6	end i-cycle 90
			35.1	997.2	mid i-cycle 94
			36.2	1048.0	mid i-cycle 98

2.3.2 Age model construction for 340-1050 ka

Prior to 340 ka, our new astronomically-tuned age model was constructed by correlating the precession-related variations in the Ti/Al record to the June 65°N insolation time series (Laskar et al., 1993) with a fixed 2.7 kyr time lag (figure 2.3). For this purpose, we first performed a Blackman-Tukey spectral analysis on the Ti/Al series in the depth domain using the Analyseries program (Paillard et al., 1996) on the lower part of the record (>15 rmcd). The analysis revealed a dominant frequency at 1.70±0.2 cycles/m, which we attributed to the imprint of the precession cycle. Using a Gaussian filter, we extracted this precession-related frequency and determined the successive minimum and maximum values to tie them to their inferred insolation extremes (table 2.2). In some cases we chose as tie points the intervals of maximum rate of change, in particular when the interference between obliquity and precession results in exceptionally broad insolation maxima (e.g. at 540 ka; figure 2.3). Tuning of the Ti/Al record to 65°N June 21st insolation curve is overall straightforward, especially in intervals with pronounced eccentricity.

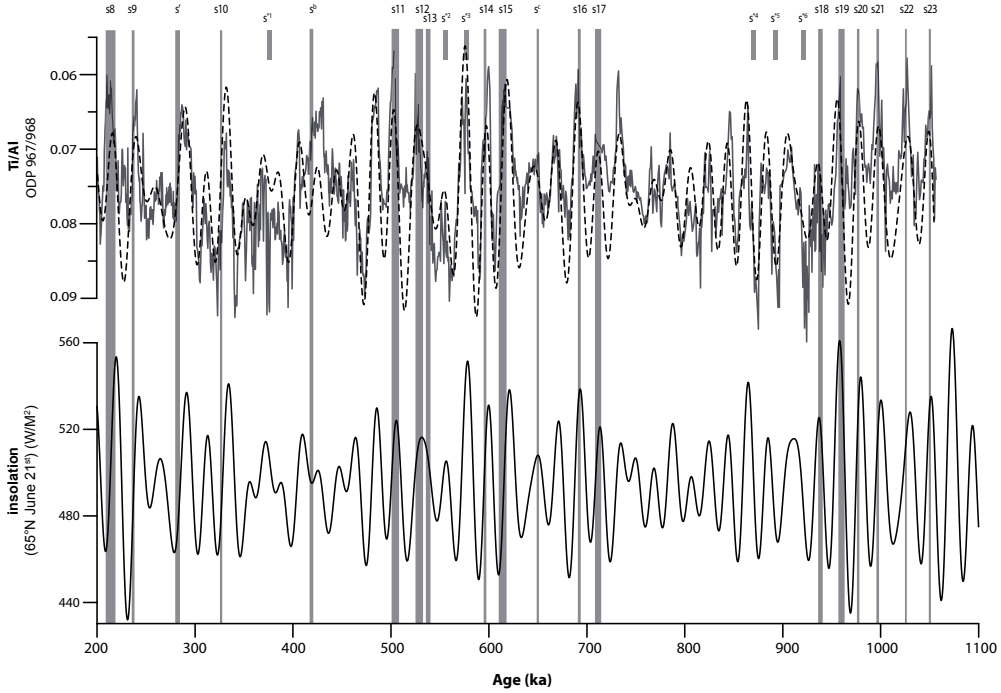

Figure 2.4: the extended composite Ti/Al record, tuned to 21 june 65°N insolation (Laskar et al. 1993). The dashed line is the combination of 21 kyr and 41 kyr variability filtered out of the Ti/Al record using Analyseries (Paillard et al. 1996). Sapropels as defined by Emeis et al. (2000), set on the Ti/Al age model, are marked with grey bars.

2.3.3 Turbidites

For our final time series, we eliminated a number of turbiditic layers in the sediments of ODP 967 aged between 650 to 950 ka (appendix IV). These layers, though not always apparent from the core surface, are identifiable through sudden and extreme enrichment (depletion) of the elements Ti, Si, Zr (Ca), and to a lesser extent, Fe, Na, K, and P. (figure 2.3) This enrichment is the result of a sorting effect favoring the relatively larger, more angular grains associated with windblown sediments and therefore aeolian elements, at this site.

The turbidites seem to occur predominantly during precession minima, when Ti/Al values are generally low. Such relations between astronomical forcing and turbiditic systems have been documented before in this basin (Postma et al., 1993; Weltje and de Boer, 1993). Often, they coincide with sapropels – though not exclusively so. On the other hand all turbiditic layers coincide with the glacial terminations (appendix IV) as documented by Lisiecki and Raymo (2005), suggesting that they were triggered by sudden changes in glacio-eustatic sea level. In particular, the onset of recurrent turbiditic layers after 950 ka (MIS 25/26) may be related to the Mid Pleistocene Transition (MPT) when global ice volume and associated sea level changes became larger. The absence of turbiditic layers after 650 ka, i.e. around the end of the MPT, is most likely related to the predominant use of data from ODP 968 in the composite after 650 ka, the depositional depth of which is ~600m shallower than that of ODP 967. As a result, ODP 968 may be situated above the typical depth where the mass movements occur on the slopes of the Eratosthenes seamount.

2.4 Evaluation of the Late Pleistocene sapropel Chronology

Our new Ti/Al tuning results in a highly detailed chronology for events, such as sapropel depositions and tephra layers that can be compared to other studies. Table 2.3 gives an overview of the new ages for the sapropel midpoints compared to those given by Emeis et al. (2000), Langereis et al. (1997) and Lourens (2004). The differences are small or negligible down to ~400 ka (see also Ziegler et al., 2010). A first major deviation occurs during the eccentricity minimum around ~400 ka, where we correlate sapropel b in ODP 967 (Emeis et al., 2000) to one insolation cycle (i-cycle) older, resulting in an age difference of ~12 kyr due to the relatively short precession period at that time. Sapropel b in ODP Site 967 has been correlated to SAP 8 in ODP Site 964 (Emeis et al., 2000) and S11 in KC01B (Lourens, 2004), and is deposited at the onset of MIS 11. The S11 was initially correlated to the insolation maximum at 407 ka (Lourens et al., 1996), since the maximum summer insolation value is much stronger than that at 419 ka. The Ti/Al record however allows little room for such an interpretation: the sharp gradient in insolation around 404 ka is reflected very clearly in the Ti/Al ratio (figure 2.4). Adhering to the proposed age of 407 ka for sapropel b would put the Ti/Al record in antiphase with insolation, for which there are no plausible arguments. Moreover, it would compress the record above this interval, and stretch it below, resulting in unlikely changes in sedimentation rate. Hence, our tuning suggests that the age of the S11, SAP 8 and Sapropel b are one i-cycle older than initially proposed or that the deposition of these sapropels was not time equivalent.

Our new sapropel chronology of ODP 967/968 is consistently older than that proposed by Emeis et al. (2000) below Sapropel b down to ~860 ka. In particular, most sapropels should be tuned one, and in a few cases two, i-cycles older than proposed by Emeis et al. (2000). Our new tuning is largely consistent however with the revised chronology used in the ATNTS2004 (Lourens et al., 2004) and that of ODP 964 (Lourens, 2004). The only exception is S13, related to i-cycle 48 according to Emeis et al. (2000). The latter interval, which appears to be a double sapropel with S12 just above it (figure 2.4), seems to correspond to an obliquity maximum rather than precession related forcing. The interference between the two orbital parameters creates a broad insolation maximum here around 530 ka. S13, correlated to Sa in KC01 or SAP10 in ODP 964 as proposed by Lourens et al. (2004), is not related to i-cycle 52 (table 2.3).

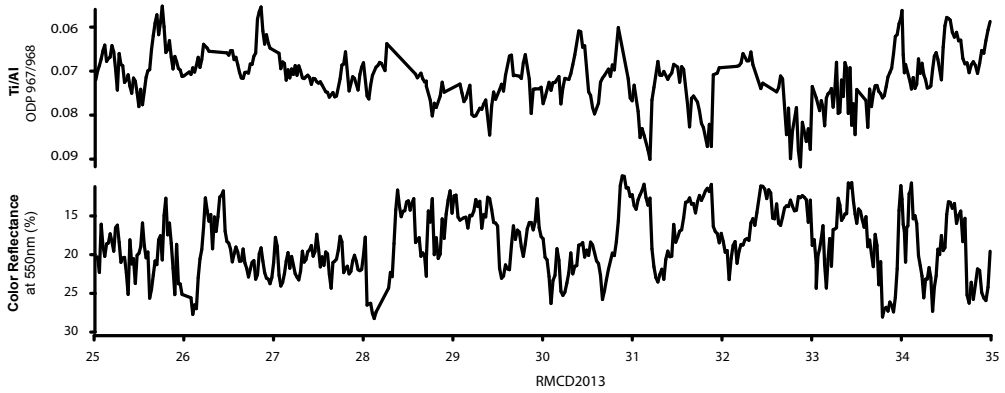

Figure 2.5: the Ti/Al and color reflectance records of ODP site 967 plotted over depth. The two proxies are especially incongruent between 29-34 RMCD.

The interval between 700-950 ka does not contain any sapropels and has proven problematic to tune. A more thorough discussion on this interval will be presented in the next section. Prior to 950 ka, the sapropel chronology of Emeis et al. (2000) is in agreement with that of Lourens et al. (2004) and compares well with the ages we obtained for S19 through S22.

2.5 Discussion

2.5.1 Incongruent behavior of the proxies

The Ti/Al proxy has enabled us to make a new tuning for the combined record of ODP cores 967 and 968. As a consequence the age model for the sapropels in these cores has shifted significantly in large parts of the record. This new tuning is robust and the age estimates are more accurate than before. However, there are some incongruencies between the different proxies in the interval between 700-950 ka, which contains very few sapropel deposits. The relatively weak insolation changes in this time interval of low eccentricity creates difficulties with tuning because proxies lack a characteristic pattern to tie to insolation. Emeis et al. (2000) use so-called 'red intervals' as indicator for missing or so-called ghost sapropels for tuning to insolation. However, the color reflectance proxy in this interval behaves capriciously and contradictory to the Ti/Al record (figure 2.5). Of these proxies, Ti/Al has the simplest operational mechanics, and generally seems to be much more linearly related to insolation (figure 2.4). Therefore we argue that the Ti/Al tuning renders the most reliable age model.

Our Ti/Al based ages for sapropels or red intervals in this period, as identified by Emeis et al. (2000), often diverge significantly from their estimates (table 2.3). For example, one of the red intervals tuned by Emeis et al. (2000) to i-cycle 74 appears much more related to a maximum in obliquity than to a minimum in precession. A similar situation seems to hold for the red interval S*5, tuned to i-cycle 82 by Emeis et al., that occurs during an insolation minimum but coincides with an interval of high obliquity. Many other red intervals defined by Emeis et al. in the period 700-850 ka appear, according to our age model, unrelated to insolation and have as such not been dated.

2.5.2 Obliquity influence in the Ti/Al proxy record

Another intriguing fact is the relatively large influence of obliquity found in the Ti/Al record (figure 2.6). Its influence has been recognized before in the sapropel record, e.g. by Lourens et al. (1996). They constructed a curve by generating a normalized precession curve and detracting a normalized obliquity signal divided by two (P-½T curve). This is very similar to the 65°N June 21 insolation curve in terms of relative power and has a power spectrum that is nearly identical. The added benefit of the P-½T curve is that the phasing of obliquity power and precession power can be controlled separately in the target curve. A different phase for these factors creates a different interference pattern in the target curve. Lourens et al. (1996) used this feature to test which phasing for obliquity best matches the thick/thin alternations of the sapropel record. They found that a phase lag of 3 kyr for tilt has the closest match. That is close to the ~4 ± 0.7 kyr lag between the Ti/Al record and obliquity found in this study by cross spectral analysis. Although some influence of global climate cannot be excluded, this relatively short lag indicates that the 41 kyr signal in the record is not due to a teleconnection with high boreal latitudes. The time lag of ice volume response to insolation is ~7 kyr (Lisiecki and Raymo, 2005). Instead, it implies that the obliquity power with its associated time lag found in these monsoon proxies is an intrinsic part of this low latitude climate system.

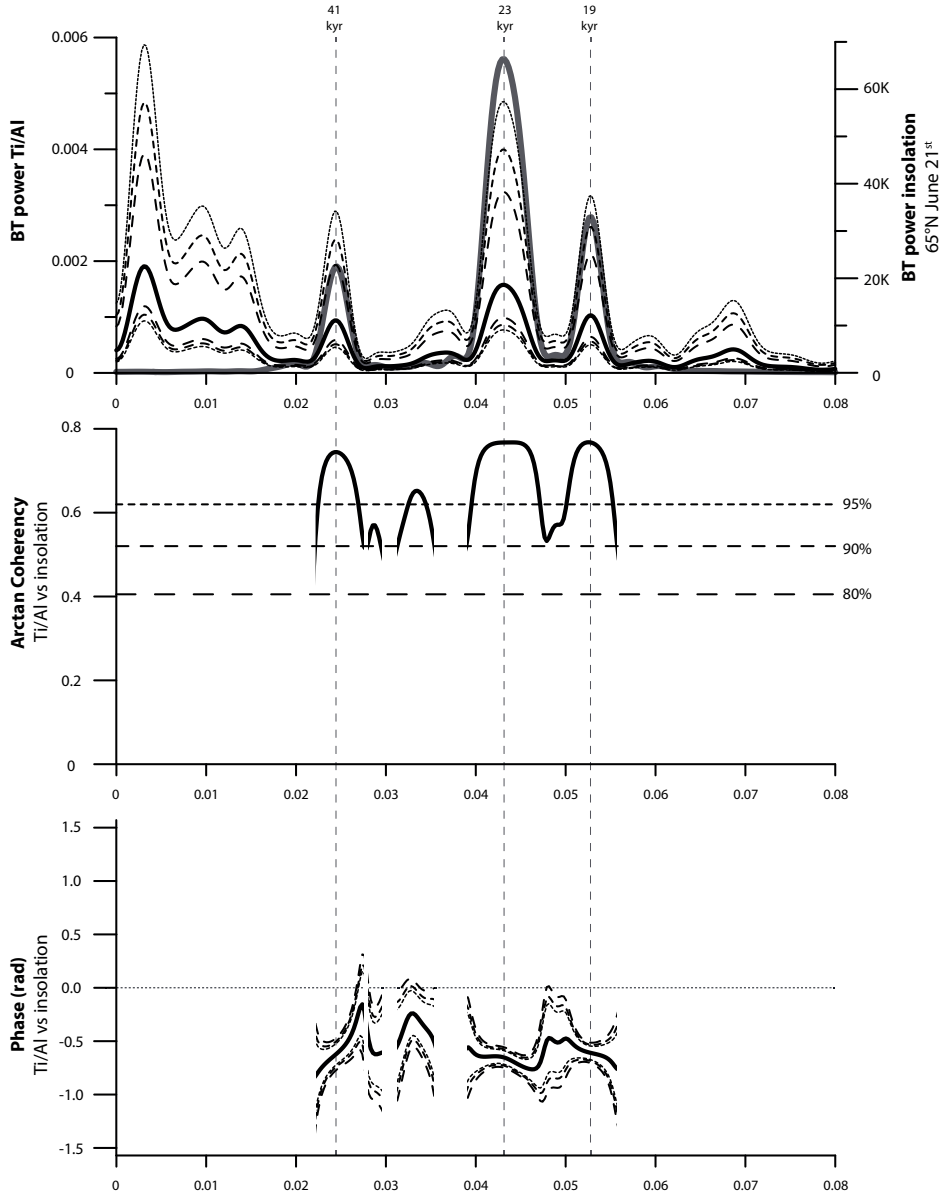

Figure 2.6: Top panel: power spectrum of the tuned Ti/A record, enveloped by the confidence limits at 80, 90, an 95%, and the power spectrum of the target insolation curve in red. The distribution of power is similar, with a dominant spectral peak at 23 kyr and smaller ones at 41 and 19 kyr – reflecting the linear behavior of Ti/Al in response to insolation. middle panel: coherency between the Ti/Al record and insolation. Only at the dominant frequencies does the coherency reach the 95% confidence boundary. Bottom panel: Phase difference between the Ti/Al record and insolation, in radials. The high coherency translates into a narrow uncertainty envelope at the dominant spectral frequencies. The phase difference corresponds to a time lag of 3.9 kyr, 2.5 kyr, and 1.7 kyr for the orbital periods of 41 kyr, 23 kyr, and 19 kyr, respectively.

The intriguing possibility of low latitude climate control by obliquity has been discussed before. In an earlier study into the dust content of ODP 967 (Larrasoaña et al., 2003) magnetic measurements are used to find the hematite content of the sediment. Arguably this proxy works much in the same fashion as our Ti/Al record. The 3 Myr record of Larrasoaña et al. (2003) extends well into the 41 kyr world of before the Mid Pleistocene Transition (0.6-0.9 Ma). Spectral analysis reveals a strong, even dominant influence of obliquity in their record (Larrasoaña et al., 2003), where low dust input is also linked to high obliquity. They argue that high obliquity might enhance the dust flux through an increased meridional temperature gradient in the Southern Hemisphere during austral winter. Additionally, they pose that a critical watershed is activated during periods of higher obliquity, making the North African monsoon susceptible to a threshold-type response to what would otherwise seem a minor latitudinal change in the African summer monsoon penetration (Larrasoaña et al., 2003). This seems possible, although the highly linear relationship between our Ti/Al record and insolation speaks against the involvement of a threshold.

Another possible low latitude mechanism explaining a direct influence of obliquity on this low latitude setting is proposed by Lourens and Reichart (1996). They reasoned that the northward shift of the ITCZ during monsoon season expands the Hadley circulation in summer, which would reach from the tropic of Capricorn at 23°S and the ITCZ, perhaps as far as 23°N during strong monsoons. The strength of this monsoon is regulated by the contrast between the insolation at 23°S and 23°N. Lourens and Reichart argue that a target curve of the insolation differences between 23°N and 23°S introduces a significant amount of power in the obliquity range and matches the thick/thin pattern of sapropels much better than the monsoon index of Rossignol-Strick (1983). This idea, based on the functioning of the present day monsoon system, has recently gained support from modeling results exploring the effect of obliquity on low latitude climate (Bosmans, 2014).

2.6 Conclusions

We constructed a high-resolution composite record by combining data from ODP 967 with the adjacent site 968. Using X-Ray Fluorescence we produced a high resolution geochemical dataset. The high level of agreement between the Ti/Al ratio (proxy for monsoon activity) and the Sanbao/Hulu caves (Cheng et al., 2009) allows us to establish the relation between North African Monsoon activity and insolation. Using this relation we create a new and highly accurate age model for the composite record and the sapropels therein through orbital tuning of the Ti/Al record.

Our age model for the sapropels in ODP 967/968 is different from the previously published chronology of Emeis et al. (2000). In most cases our chronology agrees with the ATNTS2004 (Lourens et al., 2004) and the chronological framework of Lourens (2004) for ODP 964. In the interval between 700-950 ka – where changes in insolation forcing are generally small and sediments are devoid of true sapropel formation – the Ti/Al proxy behaves very differently from the color reflectance values, or 'red intervals, that are otherwise used to mark missing sapropels. In these cases of conflicting proxy data the Ti/Al proxy is given preference because it has the simplest operational mechanics and linearly resembles the insolation curve. The different behavior of this proxy leads to major revisions of the existing age model of Emeis et al. (2000).

Throughout our record we find significant influence of obliquity. Cross spectral analysis shows a lag of ~4 ± 0.7 kyr to obliquity maxima, pointing at a direct response to insolation rather than a teleconnection to the high latitudes, with a time lag that is intrinsic to the climate system and only minor influences from other sources (i.e. ice volume). A possible mechanism introducing obliquity

power in these low latitudes is using the gradient between 23°N and 23°S June 21 insolation, as opposed to just low latitude northern hemisphere insolation as the driver for monsoon strength.

Supplementary data are available in the Pangaea database under doi 10.1594/PANGAEA.831712

Acknowledgements: This project was financially supported by NWO-ALW (project number 865.10.001). We kindly acknowledge the Ocean Drilling Program in general, and Walter Hale and the Bremen Core Repository specifically for the samples used in this study. Thanks to two anonymous reviewers for valuable comments.

This work was initiated by L.J. Lourens. Lab work and analyses were performed by M. Ziegler and T.Y.M. Konijnendijk. T.Y.M. Konijnendijk wrote the manuscript, with contributions of the other authors.

Table 2.3: comparison of sapropel chronologies. The columns on the left present the chronology of Emeis et al. (2000) for ODP 967 sapropel midpoints and those of red intervals identified by Emeis et al. (2000). The middle columns present the chronology of Lourens (2004) for Eastern Mediterranean sapropels. The presented data represent sapropels from ODP 964 as defined by Emeis et al. (2000), KC01, and KC01B, and are correlated to the ODP 967 sapropels in the columns to the left. The columns on the right present the data of this study. This is an extension of the data of Ziegler et al. (2010), which consists of all data up to 967-968-s10. The lithological boundaries and midpoints of sapropels are as defined by Emeis et al. (2000). The nomenclature follows Emeis et al. (2000), with a prefixed '967-968' to avoid confusion with the classification in KC01 and KC01B. An exception is s' (~288 ka), which is renamed to match its KC01 counterpart. Several of the red intervals identified by Emeis et al. (2000) are renamed as an s* followed by a number, though not all are recognized as a response to insolation (n.i.). Note that an extended table like this one is added as an appendix to this thesis, based on the extended age model in chapter 5.

Emeis et al. (2000)				Lourens (2004)														
Sapropel[1] no. in 967	Type	i-cycle[1]	Age[1] (ka)	ODP 964[1,2] code	KC01(B)[2] code	i-cycle[2]	Age[2] (ka)	Composite 967-968[3] code.	Site	Hole	Core	sect.	top	bot	midpoint mbsf	midpoint[a] rmcd	midpoint[3,a] age	i-cycle[3]
1	SAP	2	8	SAP 1	S1	2	8.5	s1	968	A	1	1	64	84	0.74	1.18	8.3	2
*	red INTERVALS	4	35	-	-	-	-	n.i.	968	-	-	-	-	-	-	-	-	-
a	GHOST?	6	55	-	-	-	-	n.i.	968	-	-	-	-	-	-	-	-	-
2	SAP	8	81	X	S3	8	81	s3	968	A	1	4	92	109	5.50	4.30	80.6	8
3	SAP	10	102	SAP 2	S4	10	101	s4	968	A	1	5	52	58	6.55	5.22	101.8	10
4	SAP	10	102	-	-	-	-	s4 precursor	968	A	1	5	76	84	6.80	5.39	107.8	10
5	SAP	12	124	SAP 3	S5	12	124	s5	968	B	2	2	4	44	7.14	7.54	125.5	12
*	red INTERVALS	14	148	-	-	-	-	n.i.	968	-	-	-	-	-	-	-	-	-
6	SAP	16	172	SAP4	S6	16	172	s6	968	B	2	4	32	104	10.74	9.72	172.0	16
7	SAP	18	195	SAP5	S7	18	195	s7	968	B	2	5	52	102	12.16	10.88	195.2	18
8	SAP	20	217	SAP6	S8	20	216	s8	968	B	2	6	10	76	13.33	11.68	216.8	20
9	SAP	22	240	SAP7	S9	22	239	s9	968	A	2	4	40	51	13.96	12.41	239.7	22
*	red INTERVALS	24	262	-	-	-	-	n.i.	968	-	-	-	-	-	-	-	-	-
*	red INTERVALS	26	288	Y	S'	26	288	s'	968	A	2	5	108	132	16.20	13.77	287.5	26
*	red INTERVALS	28	310	-	-	-	-	n.i.	968	-	-	-	-	-	-	-	-	-
10	SAP	30	331	Z	S10	30	331	s10	968	A	2	6	108	113	17.61	15.38	332.3	30
*	red INTERVALS	34	369	-	-	-	-	s*[1]	967	C	2	4	102	-	15.03	16.90	375.8	34
b	SAP	38	407	SAP8	S11	38	407	s[b]	968	A	3	1	136	149	19.94	18.32	418.9	40
11	SAP	44	461	SAP9	S12	48	502	s11	968	A	3	4	32	52	23.42	20.47	504.5	48
12	SAP	46	483	-	-	-	-	s12	968	A	3	4	130	10	24.40	21.31	527.9	50
13	SAP	48	503	SAP10	Sa	52	553	s13	968	A	3	5	30	46	24.88	21.72	538	*
*	red INTERVALS	50	529	-	-	-	-	s*[2]	968	A	3	5	100	-	25.50	22.26	556.9	52
*	red INTERVALS	52	553	-	-	-	-	s*[3]	968	A	3	6	4	-	26.04	22.73	577.3	54

Emeis et al. (2000)				Lourens (2004)															
Sapropel[1] no. in 967	Type	i-cycle[1]	Age[1] (ka)	ODP 964[1,2] code	KC01(B)[2] code	i-cycle[2]	Age[2] (ka)	Composite 967-968[3] code.	Site	Hole	Core	sect.	top	bot	midpoint mbsf	midpoint[a] rmcd	midpoint[3,a] age	i-cycle[3]
14	SAP	54	575	SAP11	S*	56	596	s14	968	A	3	6	72	83	26.76	23.36	596.8	56
15	SAP	56	597	SAP12	Sb	58	618	s15	968	A	3	6	126	148	27.37	23.96	617.3	58
c	GHOST?	58	618	-	*	-	-	s[c]	967	A	3	4	4	7	23.36	24.61	650.2	60
*	red INTERVALS	60	647	-	-	-	-	n.i.	967	-	-	-	-	-	-	-	-	-
16	SAP	62	668	-	-	-	-	s16	967	A	3	4	121	124	24.53	25.78	692.3	64
17	SAP	64	690	-	-	-	-	s17	967	A	3	5	18	40	25.09	26.34	714.0	66
*	red INTERVALS	74	785	*	*	74	784	n.i.	967	-	-	-	-	-	-	-	-	*
*	red INTERVALS	76	804	-	-	-	-	n.i.	967	-	-	-	-	-	-	-	-	-
*	red INTERVALS	78	822	-	-	-	-	n.i.	967	-	-	-	-	-	-	-	-	-
*	red INTERVALS	80	841	-	-	-	-	n.i.	967	-	-	-	-	-	-	-	-	-
*	red INTERVALS	82	862	*	*	82	861	s*[4]	967	B	4	3	22	-	27.53	31.07	870.6	82*
*	red INTERVALS	84	882	-	-	-	-	s*[5]	967	B	4	3	90	-	28.21	31.76	892.8	*
*	red INTERVALS	86	908	-	-	-	-	s*[6]	967	B	4	4	28	-	29.09	32.73	921.1	86
18	SAP	88	934	-	-	-	-	s18	967	C	4	1	142	150	29.92	33.41	937.7	*
19	SAP	90	955	SAP13	S″	90	955	s19	967	C	4	2	50	72	30.50	33.98	957.5	*
20	SAP	92	977	SAP14	Sc	92	977	s20	967	C	4	2	110	113	31.10	34.53	377.2	92
21	SAP	94	997	SAP15	*	94	997	s21	967	C	4	3	6	9	31.50	35.04	996.4	94
22	SAP	96	1027	SAP16	*	96	1027	s22	967	C	4	3	67	74	32.17	35.71	1026.0	96
23	GHOST?	98	1048	-	*	-	-	s23	967	C	4	3	121	123	32.71	36.26	1050.3	98

[a]Sapropel midpoints as defined by Emeis et al. (2000), their age estimate according to the Ti/Al age model
[1]Emeis et al. (2000)
[2]Lourens, 2004; retuning of KC01B, ODP 964, KC01
[3]Ziegler et al. (2010); this study
n.i.: not identified

If you start with your own desires for what Nature should do, consider Nature's own observed reasons for doing things, and then rationalize an extremely persuasive argument for why Nature should produce your preferred outcome for Nature's own reasons, then Nature, alas, still won't listen.

Eliezer Yudkowsky

Chapter 3

On the timing and forcing mechanisms of late Pleistocene glacial terminations: Insights from a new high-resolution benthic stable oxygen isotope record of the eastern Mediterranean.

Benthic oxygen isotope records of deep marine sedimentary archives have yielded a wealth of information regarding ice sheet dynamics and climate change during the Pleistocene. Since they often lack independent age control, these records are generally bound, however, by a fixed phase relationship between orbital forcing and the climate, e.g. ice volume, response, since they often lack independent age control. Here we present the first long (~1.2 Ma) benthic oxygen isotope record from the Eastern Mediterranean, based on ODP Sites 967 and 968, which clearly reflects the behavior of global climate on a glacial-interglacial scale throughout this time period. The age model for our record is based on tuning the elemental ratio of titanium versus aluminum (Ti/Al) against insolation. The Ti/Al record is dominated by the precession-related changes in northern African climate, i.e. monsoonal forcing, and hence largely independent of glacial-interglacial variability. We found the largest offset between our chronology and that of the widely applied, open ocean stacked record LR04 (Lisiecki and Raymo, 2005) for T_{VII} (~624 ka), which occurred ~9 kyr earlier according to our estimates, though in agreement with the AICC2012 δD_{ice} chronology of EPICA Dome C (Bazin et al., 2013). Spectral cross-correlation analysis between our benthic $\delta^{18}O$ record and 65°N summer insolation reveals significant amounts of power in the obliquity and precession range, with an average lag of 5.5±0.8 kyr for obliquity, and 6.0±1.0 kyr for precession. In addition, our results show that the obliquity-related time lag was smaller (3.0±3.3 kyr) prior to ~900 ka than after (5.7±1.1 kyr), suggesting that on average the glacial response time to obliquity forcing increased during the mid-Pleistocene transition, much later than assumed by Lisiecki and Raymo (2005). Finally, we found that almost all glacial terminations have a consistent phase relationship of ~45±45 degrees with respect to the precession and obliquity-driven increases in 65°N summer insolation, consistent with the general consensus that both obliquity and precession are important for deglaciation during the Late Pleistocene. Exceptions are glacial terminations T_{IIIb}, T_{36} and potentially T_{32} (and T_{VII} T_{24} and T_{34}), which show this consistent phase relationship only with precession (only with obliquity).

This manuscript is under review at Quaternary Science Reviews DD 9 April, 2015

3.1 Introduction

The global climate state shifted through the past 1 million years (Ma) of Earth's history from a predominantly obliquity driven glacial-interglacial mode towards a pronounced 100-kyr glacial-

interglacial rhythm (Imbrie et al., 1993; Tiedemann et al., 1994; Lisiecki and Raymo, 2005). This transition is known as the Mid Pleistocene Transition (MPT) and its origin is still under debate (e.g Clark et al., 2006; Maslin and Ridgwell, 2005). Part of the discussion relates to the fact that the benthic foraminiferal $\delta^{18}O$ isotope record – reflecting both changes deep sea water temperatures and the isotopic composition of sea water through the uptake of isotopically light water in ice sheets – behaves erratically with respect to the astronomical cycles of precession and obliquity, which are considered as the major forcing mechanisms of the glacial-interglacial variability during this time period (Hays et al., 1976; Imbrie et al., 1993; Tiedemann et al., 1994; Lisiecki and Raymo, 2005). The available knowledge of how climate and ice sheets respond to the precession and obliquity-driven insolation usually stems from the last and penultimate glacial-interglacial transitions, which are well constrained by highly detailed records that are readily datable using radiocarbon or other absolute methods (e.g. Lourens, 1996; Martrat, 2004; Lemieux-Dudon et al., 2010). This inferred knowledge about climate response to insolation forcing has generally been extrapolated into the past. In other words, a predefined relationship is used to tune the benthic foraminiferal $\delta^{18}O$ isotope record to insolation forcing using a fixed phase lag between the data and the target curve, generally represented by a simple ice-sheet model (e.g. Shackleton et al., 1990; Lisiecki and Raymo 2005).

With the availability of long and high quality records, Lisiecki and Raymo (2005) established a state of the art marine isotope chronology based on 57 benthic isotope records, spanning the last 5.3 Ma: the LR04 benthic oxygen isotope stack. This high-resolution reconstruction of global climate is the current global standard for correlating marine oxygen isotopic records as well as many other climate reconstructions (e.g. Wolff et al., 2006; Parrenin et al., 2007; Tzedakis 2007), as well as inversion modeling studies to disentangle the ice volume and deep-sea temperature signal (e.g. Bintanja et al., 2005). The age model for the LR04 benthic stack was established by tuning the stacked record to a simple ice sheet model (Imbrie and Imbrie 1980). In this model it is assumed that the phase lags in ice sheet response at the frequencies of obliquity and precession are those of a single exponential system (Imbrie and Imbrie, 1980; Imbrie et al., 1984; Lisiecki and Raymo, 2005). The ice-sheet model (equation 1) is forced by the normalized 21 June 65°N insolation curve (Laskar et al., 1993; 'x' in equation 1), taking into account an ice sheet response time (Tm) of 15 kyr and a non-linearity coefficient b of 0.6, based on radiometric dating of the penultimate glacial cycle (Imbrie and Imbrie 1980).

$$dy/dt = (1 \pm b) / Tm(x-y) \quad (1)$$

The change in ice volume over time (dy/dt) therefore depends on the insolation forcing x versus present ice volume y, with nonlinearity b switching signs: it is negative while ice is growing and positive when the ice sheets decay (i.e. when dy/dt is negative). Together this describes the slow buildup and fast ablation of the Late Pleistocene ice sheets with a delay in ice sheet response of 4.2, 5.0 and 7.9 kyr in the 19 and 23 kyr components of precession and the 41 kyr component of obliquity, respectively. The constants Tm and b are generally assumed to be invariant with time even though the accumulation rate and size of the ice sheet varied continuously (Shackleton et al., 1990). One objection to the above methods is that we have insufficient possibilities to verify the outcome of such tuned age models. In a limited number of cases a reversal of the earth's magnetic field or radiometrically datable tephra layers generates some control on the tuning, but in most situations the astronomical age model is more precise and deviations fall within error margins of possible secondary age control (Shackleton et al., 1990). Lisiecki and Raymo (2005) used sedimentation rate as a control on their age model. They labored under the reasonable assumption that their stack cannot exhibit overly large variations in sedimentation rate. Therefore, they restricted the

algorithm's freedom to compress or stretch their record in tuning it to insolation. This conservative approach however still overrides any natural variability in the Earth's response to insolation forcing by aligning the record to a model with predefined response times.

The broadly accepted astronomically-based tuning approach was tested by Huybers and Wunsch (2004), who made a reconstruction of Pleistocene climate change from a stack of 21 marine sediment cores, using only a generalized sedimentation rate as an estimate for the age/depth relation in his record, with radiometrically dated geomagnetic boundaries as age markers. With this approach they produced independent age constraints for isotopic shifts, and argued that tuning to insolation suppresses weak non-linear interactions, i.e. climate variability with a periodicity of 70 and 29 kyr. Also, the role of eccentricity-modulated precession is often criticized and obliquity suggested as the dominant late Pleistocene climate forcing (Huybers and Wunsch, 2004; Huybers, 2007; 2011). Unfortunately, letting sedimentation rates dictate the age model entirely introduces large uncertainties in the estimates. Adding a different form of age control is the best way to improve this valuable approach.

Better estimates of the phase relation between insolation forcing and the benthic $\delta^{18}O$ response are necessary to improve our understanding of the timing and nature of climatic shifts, such as the MPT and glacial terminations. Outside the realm of deep sea coring there is a variety of settings offering the possibility of climate reconstruction, sometimes with the advantage of additional age control, like radiometric dating. Reconstructions of sea level in relation to ice volume changes have been based on the coral reef growth of Barbados (Harmon et al., 1978, 1983; Bard et al., 1990) using ^{14}C dating and U/Th dating for the last 250 kyr. Dutton et al. (2009) used a set of U/Th-dated speleothems from Italy to reconstruct the sea level of MIS 7 in detail. Also of very high resolution is the speleothem-derived monsoon activity reconstruction of Sanbao-Hulu (Wang et al., 2008; Cheng et al., 2009). The speleothem $\delta^{18}O$ record reflects changes in the strength of the East Asian summer monsoon. The record is dated by U/Th dates back to ~390 ka with average dating errors within ~0.5kyr (Cheng et al., 2009). It is a highly precise, highly accurate paleoclimate record displaying fast climate shifts such as the Dansgaard-Oeschger millennial scale variability, with rapid transitions between stadial and interstadial periods (Wang et al., 2008, Cheng et al., 2009).

While all of these reconstructions provide valuable insights in paleoclimate behavior over the Pleistocene, they lack some of the benefits typical for deep sea coring. The sea level reconstructions based on corals and speleothems depend on specific locations. Such climate archives often only cover a limited time period, which gives these reconstructions a patchy character. The ice core records, while providing detailed and long sequences of paleoclimate, mostly reflect local circumstances like temperature (Jouzel et al., 2007). The Sanbao-Hulu speleothem record reflects the East Asian Monsoon. Neither of these provides an integrated signal of global climate, as it is provided by benthic $\delta^{18}O$ (Hays et al., 1976; Imbrie et al., 1984). In this study we present the first high resolution, long-term (1.2 Ma) benthic oxygen isotope record from the Eastern Mediterranean. Our record is uniquely located in a setting that allows us to date the record without tuning the isotopes to insolation or a reference curve. We arrive at our chronology by dating a geochemical signature of the sediment (§3.2.4). Therefore, no assumptions for the response time of ice volume to insolation are required. This approach builds upon earlier work by Ziegler et al. (2010), who reconstructed the last 350 kyr using sediments from ODP Site 968. With this non-standard age model we test the age and duration of all the major isotopic stages and transitions of the last ~1.2 Ma.

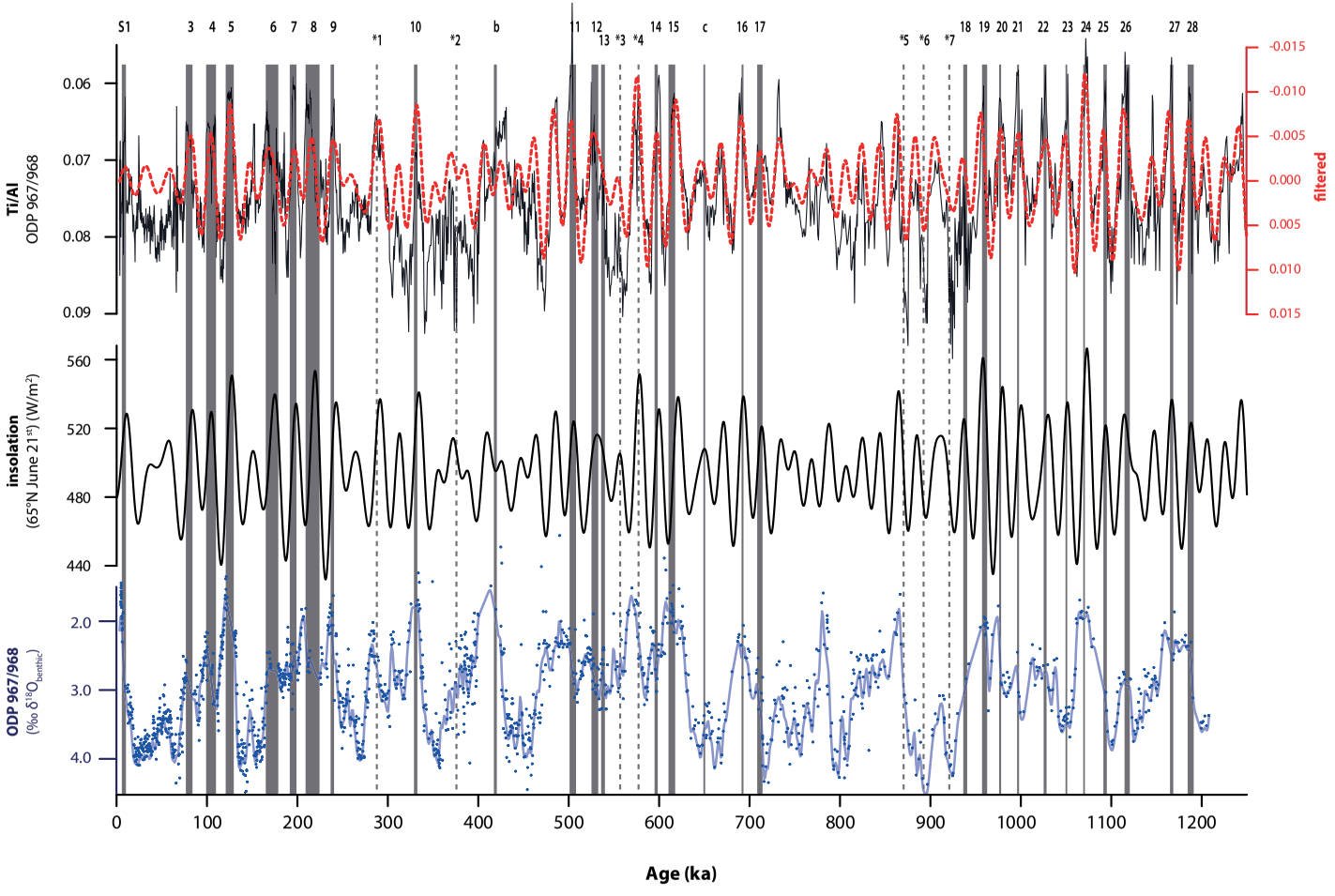

Figure 3.1: overview of the Ti/Al and benthic isotope data derived from the Eastern Mediterranean splice in relation to insolation (Laskar et al., 1993). The top graph in black is the Ti/Al proxy used for establishing the age model. The red overlay is a combination of the 23 kyr and 41 kyr signal recognized by a spectral filter (Paillard et al., 1996) after tuning, closely resembling the 65°N June 21st insolation curve (middle plot). The bottom graph is the benthic $\delta^{18}O$ record established from the Mediterranean splice. Individual measurements are indicated with blue dots. The grey line is a Gaussian low-pass (>5 kyr) filter to reduce noise. The vertical grey bars indicate sapropels as present in the Mediterranean splice (chapter 2).

3.2 Materials and Methods

3.2.1 ODP Sites 967 and 968

Our study uses data from the adjacent ODP Sites 967 and 968 in the Eastern Mediterranean (figure 1.6). ODP Site 967 (34°04'N, 32°43'E) was drilled south of Cyprus, near the Eratosthenes seamount at a water depth of 2,554 m. ODP Site 968 (34°20'N, 32°45'E) was drilled on the Eratosthenes seamount at a water depth of 1,961 m (Emeis et al., 1996). The data of the two sites are combined into a single splice using color reflectance data (chapter 2). This enabled us to extend the paleoclimatic record of Ziegler et al. (2010) of ODP Site 968, the stratigraphic recovery of which is incomplete further back in time. . The combined splice of ODP 967 and 968 was sampled at 2 cm intervals. Samples were split into a 3-5 g part that was used for X-Ray Fluorescence (XRF) analysis and the remaining 12-20 g which was washed and sieved for the extraction of foraminifers.

3.2.2 Stable isotopes

In order to generate a benthic foraminiferal oxygen isotope record for the top 350 kyr, Ziegler et al. (2010) used different species, as no single species was present throughout the whole record. The species that were analyzed are *Gyroidina altiformis*, *Gyroidina neosoldanii*, *Cibicides kullenbergi*, *Hoeglundina elegans*, *Cibicides ungerianus*, and *Melonis pompilianus*. The oxygen isotope data of *H. elegans* were corrected for its enrichment (0.78‰) relative to equilibrium calcite (Grossman, 1984). For the record below 350 ka, i.e. the new data presented here, only the species *Gyriodina neosoldanii* and *Gyroidina altiformis* were used. Between 2 to 4 specimens were hand-picked from the fraction >212 mm and used integrally for Isotope Ratio Mass Spectrometry (IRMS).

The stable isotope data of the entire record were measured on a Thermo-Finnigan MAT253 mass spectrometer, coupled with a Kiel III automated carbonate reaction device. A standard run consisted of 35 samples interspersed with 3 in-house standards (NAXOS) as well as 8 international carbonate standards (NBS-19). Calibration revealed an analytical precision better than 0.1‰ and 0.03‰ for $\delta^{18}O$ and $\delta^{13}C$, respectively.

3.2.3 Spectral analysis

All the time series analyses discussed in this paper were performed using Analyseries (Paillard et al., 1996). Blackman-Tukey spectral analyses were performed using 3 different levels of confidence: 80%, 90% and 95%. Spectral peaks were filtered from the record using a wide range (frequency ± 20%) spectral band-pass filter, unless otherwise specified. Cross-spectral analyses to reveal spectral correlation and phase between the records were also performed using Analyseries, at the same 3 levels of confidence. A cross-correlation value over 90% is considered significant, a value over 95% is considered highly significant. Wavelet analysis was performed using the standard script of Torrence and Compo (1998), with a Morlet wave transform.

3.2.4 Age model

ODP Site 967 is regarded as one of the most important reference sections for establishing the standard Pleistocene sapropel chronology of the Mediterranean (Emeis et al., 1996, 2000; Sakamoto et al., 1998; Kroon et al., 1998; Lourens et al., 1998; 2004). The chronologies of the aforementioned authors are all based on the correlation of sapropel midpoints to their correlative 65°N summer insolation maxima, including a fixed 3-kyr time lag, following Lourens et al. (1996). Differences between them have occurred because of minor adaptations within the spliced record of ODP Site 967 and different correlation schemes. Here we follow the newest (refined) chronology

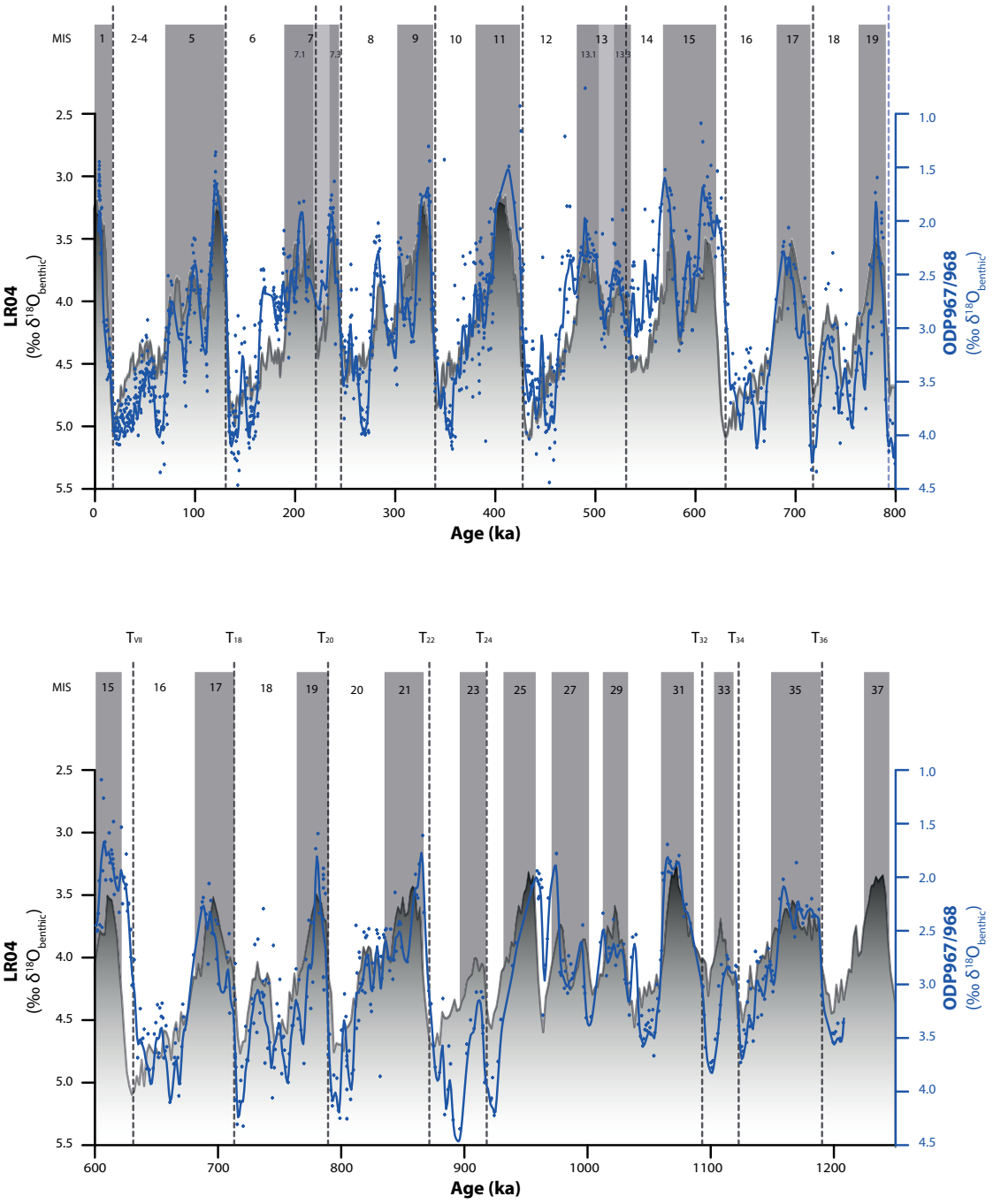

Figure 3.2: direct comparison of the Mediterranean benthic isotope record (blue dots and line) to the LR04 benthic stack (grey) (Lisiecki and Raymo, 2005). Marine isotope stages as published by Lisiecki and Raymo (2005) are indicated with grey (warm stages) and white (cold stages) background. Terminations as found in our study are indicated with vertical dashed lines.

of the combined ODP Site 967 and 968 record developed in chapter 2 for the past 1.05 Ma and extended the approach till 1.2 Ma.

For the upper 225 kyr of the record, we follow Ziegler et al. (2010), who dated this part in more detail than the initial standard sapropel chronology (e.g. Lourens et al., 1996; 2004) by correlating the color reflectance (CR) at 550 nm, Ba/Al and Ti/Al records of ODP Site 968 to the speleothem oxygen isotope ($\delta^{18}O_{speleothem}$) records of the Sanbao/Hulu caves (Wang et al., 2008). This correlation was based on the fact that the proxy records of both sites clearly reflect millennial-scale climate variability, which occurred superimposed on the dominant precession-controlled cyclicity associated with changes in the intensity of the monsoon system (Ziegler et al., 2010). In chapter 2, we followed this approach down to 340 ka, using the extended Chinese $\delta^{18}O_{speleothem}$ record of Wang et al. (2008). Accordingly, the high precision U/Th dating of the Sanbao/Hulu caves (average dating error <1%; Cheng et al., 2009) could be transferred to ODP Sites 968 and 967, assuming an in-phase relationship between the millennial-scale variability observed in both records. Ziegler et al. (2010) relied primarily on correlating the CR record of ODP Site 968 to the Chinese $\delta^{18}O_{speleothem}$ record because the repeated depositions of at least 6 tephra layers and a thin turbidite slightly affected the Ti/Al signature over the past 225 ka. In the older deposits below this point, the Ti/Al record no longer suffers from the occurrence of prominent tephra layers, and hence was used in chapter 2 and this study as primary tool for constructing the age model (figure 3.1). Note that we have removed 13 thin turbidites between 650 and 1200 ka from our spliced record (chapters 2, 5), based on their strong signature in the XRF record.

The ratio of titanium to aluminum that we measured from the bulk sediment of ODP Sites 967 and 968 (Ziegler et al., 2010; this thesis) is used as a proxy for aeolian versus riverine-derived terrestrial materials transported to the studied sites. As such it is inversely proportional to activity of the North African monsoon (Lourens et al., 2001). Windblown dust is estimated to be the source of 65% to 95% of the titanium in ODP Site 967 sediment (Wehausen and Brumsack, 2000; Lourens et al., 2001). The presence in the sediment of aluminum originates from clay minerals in the Nile outflow: a measure of runoff from the North African continent. Changes in Ti/Al mirror monsoonal-induced humidity changes in central to north Africa (Lourens et al., 2001), which is driven by changes in the earth's orbit, mainly precession (Rossignol-Strick, 1985). The most important reason to apply the Mediterranean Ti/Al record for tuning, instead of the CR or Ba/Al, is that it shows an almost linear response to insolation forcing also within 405-kyr eccentricity nodes when insolation changes are minor and sapropel depositions are lacking (Lourens et al., 2001; chapter 2).

To establish the age model for the deeper part of our record we tuned our Ti/Al record directly to the June 21st 65°N insolation target curve (chapter 2). For this purpose, we first determined the phase relationship between insolation and the precession component of the $\delta^{18}O_{speleothem}$ record through spectral cross-correlation analysis over the past 340 ka. This yielded an average lag of ~2.7 kyr between the precession component of the $\delta^{18}O_{speleothem}$ record and astronomical precession, including an uncertainty (2σ) of ±1.1 kyr. The dating uncertainty in the speleothem record averages ~1.14 kyr, which gives us a total uncertainty of ±1.6 kyr in a root mean square calculation. This is the estimated uncertainty for all age estimates beyond ~340 ka, the last tie point between our record and the Chinese $\delta^{18}O_{speleothem}$ record. We extrapolate the above relation for the rest of our record. The Ti/Al record, which is dominated by the precession component, is tuned to 65°N June 21st insolation (Laskar et al., 1993) with a lag of 2.7 kyr. The tuning process is generally straightforward, with the Ti/Al signal closely resembling insolation forcing (figure 3.1). Intervals with less pronounced eccentricity, in particular the 400 kyr minima at 400 ka (Marine Isotope Stage, or MIS,

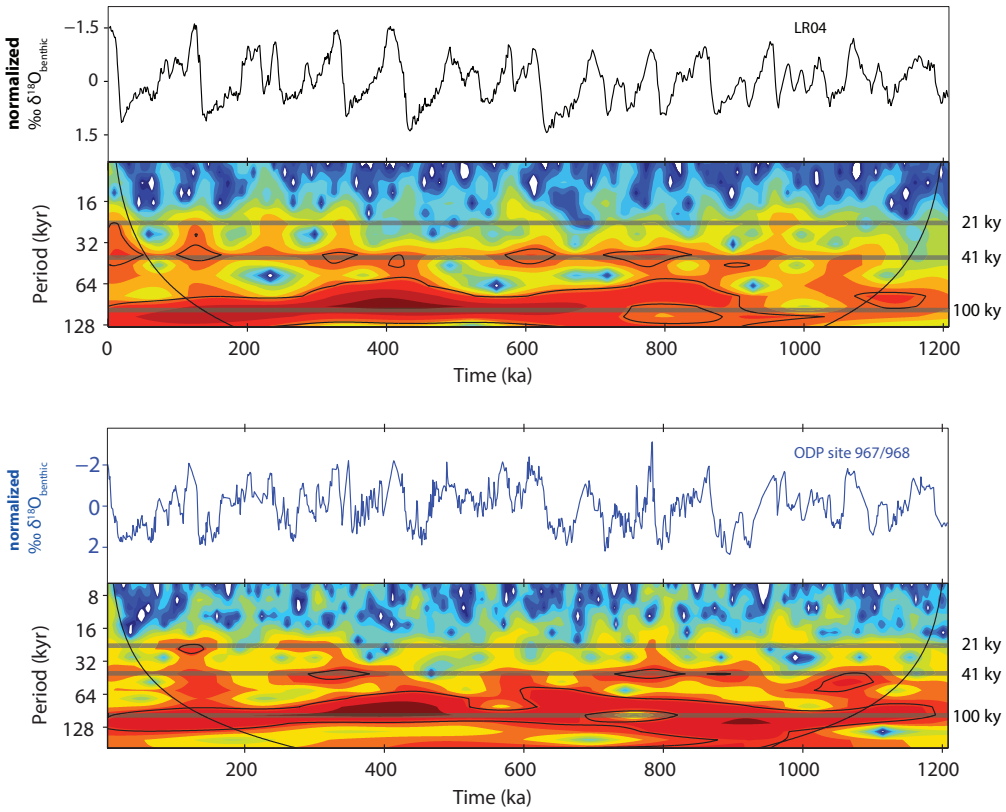

Figure 3.3: (top) the normalized LR04 record, with a wavelet transform below. Horizontal bars indicate the standard Milankovic periodicities 100, 41, and 21 kyr. Compare the normalized Mediterranean benthic isotope record and its wavelet transform (bot).

11) and 800 ka (MIS 19) raise some additional uncertainty due to the weakly expressed cyclicity in the Ti/Al record. This will be discussed in §3.4.

With the Ti/Al age model underlying our benthic isotope record, we compare the length and phase of the isotopic stages in the Pleistocene. We investigate the response of global climate and ice volume to insolation changes in view of the assumptions made by Imbrie and Imbrie (1980). We comment on the accuracy of existing chronologies like the LR04 benthic stack.

3.3 Results

3.3.1 Oxygen isotope record

All major glacial and interglacial stages (MIS1-35) of the past 1.2 Myr can be identified in the eastern Mediterranean benthic $\delta^{18}O$ record (Fig. 3.2). The transitions between stages are present without exception, making detailed estimation of the age and duration of all stages possible. The record shows some small gaps however, due to the occurrence of several episodes in which a number of successive samples are devoid of benthic foraminifers. In the youngest 250 kyr of the

record, these gaps occur exclusively within the sapropel layers (figure 3.1), hinting at hydrographical changes, i.e. low-oxygen conditions as a consequence of water column stratification, as the cause for their disappearance (Rossignol-Strick, 1985). Gaps in the record also occur below 250 ka, during MIS 9, 11, 17, 21, 25 and 27 (figure 3.1). Though often not accompanied by a fully developed sapropel, the interglacial setting may have triggered similar conditions too unfavorable for *Gyriodina neosoldanii* and *Gyroidina altiformis* to have lived at this site.

Isotopic values in the top ~0.9 Ma range from ~1.5‰ during interglacials to ~4‰ during full glacial conditions. Between 0.9 and 1.2 Ma the values range between 1.7 and 3.5‰. Late Pliocene values (MIS 96-100) reported for this core (Lourens et al., 2010) ranged from ~2‰ to ~3.1‰, meaning that the amplitude has increased during the Pleistocene, with a slight tendency toward heavier values. An increase in glacial/interglacial variability occurs around MIS 22 (900 ka), which has the heaviest isotope values measured in this record. It is a clear stepwise change towards full glacial values as found in the Late Pleistocene.

In comparison to the LR04 benthic stack, the Eastern Mediterranean record generally has much lighter isotopic values (figure 3.2) due to temperature differences (Ziegler et al., 2010). The difference ranges between 0.5-1.0‰ during glacial maxima and 1.0-1.5‰ during interglacial periods. The amplitude of glacial/interglacial variability is somewhat higher than the open ocean LR04 benthic stack due to the 'basin effect' (Rohling, 1999). This effect is a result of the fact that the Mediterranean is a net evaporative basin with limited exchange to the open ocean. The restriction of water exchange with the open ocean through the Strait of Gibraltar causes significant salinity effects as sea level changes over glacial/interglacial time scales (Rohling et al., 2014). Average benthic $\delta^{18}O$ values are slightly lighter than those in the open ocean due to generally higher deep water temperatures. Finally, the open ocean stack shows a more gradual increase in both the full glacial and mean glacial values over the course of the Pleistocene than the stepwise transition around MIS 22 in our record. Despite these differences, the two records exhibit a roughly identical signature on a glacial-interglacial scale.

3.3.2 Time Series Analysis

A wavelet conversion of the Mediterranean isotopes as well as the LR04 benthic stack indicates that the power distribution of the obliquity-related 41 kyr component and the well-known ~100-kyr glacial rhythm are the most persistent cycles in both records throughout the Pleistocene (figure 3.3). There are no indications for a distinct decrease in 41 kyr power from the early to the late Pleistocene, in association with the MPT. However, there are a couple of brief intervals, i.e. during MIS 13, 27, and 35, where the record does not show a clear 41 kyr signal (figure 3.3). Its absence during MIS 35 could be due to the fact that it occurs close to the edge of our record. MIS 13 and 27 are two intervals of low variability and with a higher frequency, ~29 kyr and 19 kyr respectively. A persistent influence of precession becomes visible in both records after ~400 ka and is clearly modulated by the 100-kyr cycle of eccentricity (figure 3.3).

Cross-spectral analysis between our record and the LR04 stack over the past 1.2 Ma reveals very similar power spectra (figure 3.4a). Both records contain strong power around the 100 kyr period, secondary power in the 41 kyr obliquity-related frequency band, and to a lesser amount in the 23 kyr precession-related frequency band. A modest concentration of power is also found around 26.5 kyr in our Mediterranean record and around 29 kyr in LR04. Both records clearly lack power in the 19 kyr precession-related frequency band. Overall coherency is high, with values above the 95% significance level at 100 kyr, 41 kyr, 29 kyr and 23 kyr periodicities (figure 3.4b). There is a lesser but significant coherency peak at 19 kyr. The phase spectrum shows that our record

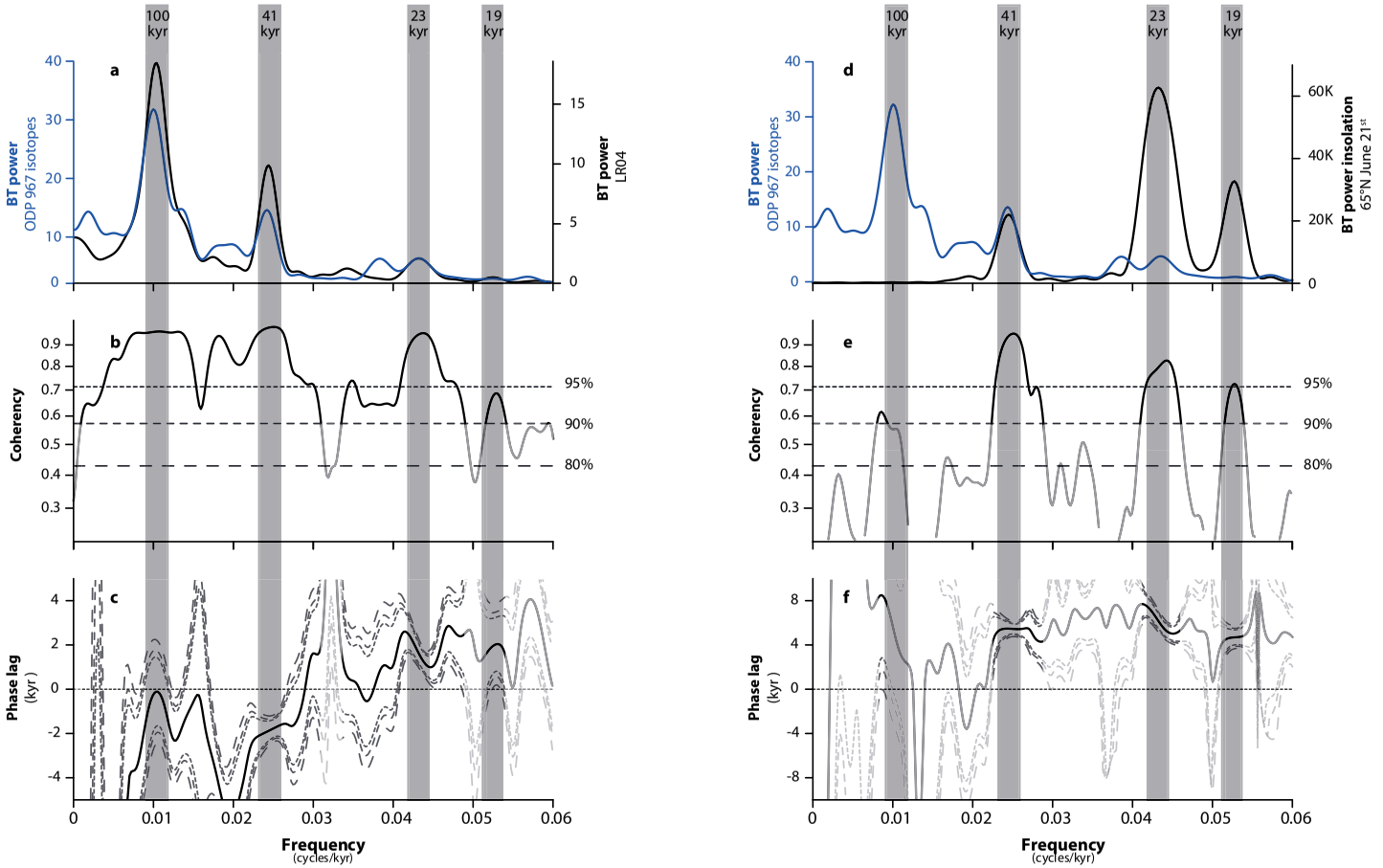

Figure 3.4: a) in blue the Blackman-Tukey power spectrum of the Mediterranean benthic oxygen isotope record, and in black that of the LR04 benthic stack (Lisiecki and Raymo, 2005). The spectra look very similar with a dominant spectral peak at 100 kyr, secondary power at 41 kyr and a smaller peak at 23 kyr.
b) coherency between the Mediterranean isotope record and LR04. Horizontal dashed lines indicate confidence levels. Coherency is consistently high (>95%) in all periods higher than 33 kyr as well as around 23 kyr. Significant (>90%) coherence also occurs at 29 kyr (0.034 cycles/kyr).
c) Phase difference between the Mediterranean isotope record and insolation, in kyr. The high coherency translates into a narrow uncertainty envelope (dashed lines) at the dominant spectral frequencies.
d-f) the same for the cross correlation between the Mediterranean benthic isotope record and June 21st insolation at 65°N.
For all frequencies where coherency is below the 90% significance level, coherency and phase values are plotted semi-transparent

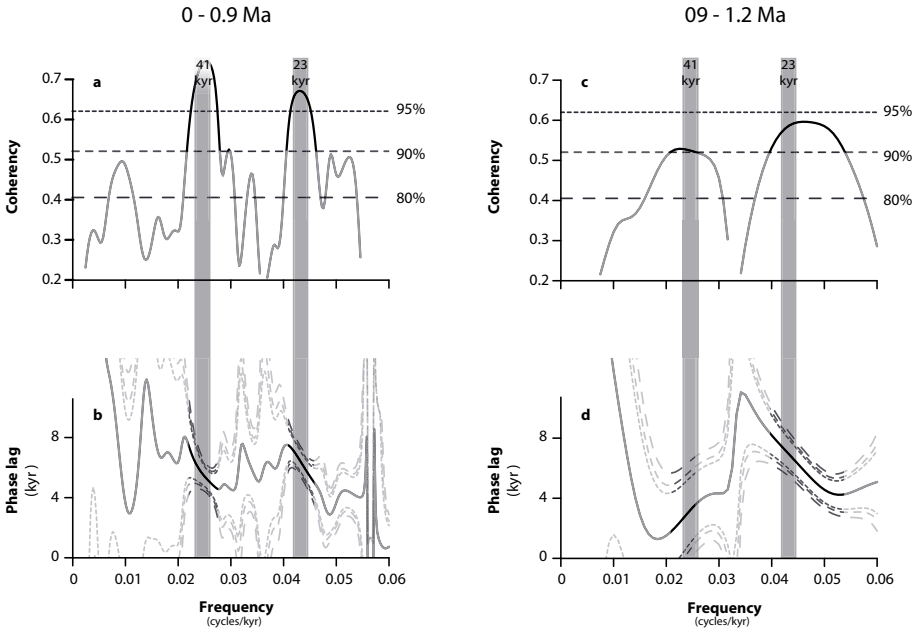

Figure 3.5: a-b) coherency and phase between the isotope record and insolation over the last 900 ka (as in figure 3.4). c-d) the same for the interval 900-1200 ka. The shorter interval and low resolution translate to higher uncertainties, though they remain significant. The lag to obliquity is considerably shorter in the Early Pleistocene, but for precession there is little change.

has a shorter lag for obliquity and a longer lag for precession than the LR04 stack.(figure 3.4c) The difference amounts to -1.5±0.4 kyr for obliquity and +1.3±0.3 kyr for precession.

Subsequently, we applied cross-spectral analysis between our isotope record and the 65°N June 21st insolation (figure 3.4d-f). Coherency is high between both records in the precession and obliquity frequency bands with values exceeding the 95% significance level (figure 3.4e). The analyzed phase relations over the past 1.2 Ma are estimated to be 5.5±0.8 kyr for obliquity and 6.0±1.0 kyr for precession.

The change in character of the $\delta^{18}O$ variability prior to MIS 22 suggests a change in relation to insolation. We performed a separate spectral analysis on our isotope record in the intervals 0-0.9 Ma and 0.9-1.2 Ma. Note that the 0.9-1.2 Ma is shorter and of lower resolution than the 0-0.9 Ma interval, which affects the reliability of the analysis. Results indicate a faster response to obliquity forcing in the Early Pleistocene than in the Late Pleistocene (figure 3.5). The phase lags are estimated 3.0±3.3 kyr for obliquity in the Early Pleistocene, versus 5.7±1.1 in the last 0.9 Ma. The results for precession are much closer together and fall well within the error margin, indicating little significant change.

3.3.3 Timing of glacial terminations

To identify the possible (orbital) forcing mechanism behind deglaciations in the Pleistocene, we followed Huybers and Wunsch (2004) and Huybers (2007; 2011), who analyzed the phase between the major glacial terminations and the main insolation variables obliquity and climatic precession (figure 3.6). First we determined the age of the terminations in our record, using an

approach adapted from Huybers (2007) and Grant et al. (2014). For this purpose we took the derivative of the benthic isotope record, which was first smoothed with a Gaussian filter, and identified the terminations as the interval where the sum of $\delta^{18}O$ change in a moving window of 4 kyr exceeds 0.8‰. This threshold is set to avoid smaller excursions and identify only the largest of deglaciation events. We average the onset and end of the termination interval to pinpoint an age (figure 3.6). The exact timing depends on the threshold used and the amount of smoothing but is not very sensitive: the estimates stay within our ±1.6 kyr uncertainty margin for a large range in threshold values. Local influences of salinity and temperature on our record will arguably have a larger influence on this measure. Nevertheless it provides us with a first order approach of the timing of glacial terminations as estimated using our Ti/Al age model (table 3.1).

Table 3.1: the timing of terminations, in kyr. Terminations T_I-T_{VII} are identified as defined by Raymo (1997), T_{18}-T_{36} follow the unofficial protocol of Lourens et al. (2010) and are named after the glacial MIS that they end. The timing is determined as explained in §3.3.2, for both the Mediterranean isotope record (second column) and LR04 (third column). The ages of T_I-T_{VII} as listed in Lisiecki and Raymo (2005) are added (fourth column) for reference.

Deglaciation	This study	LR04 *(this study)*	LR04 *(listed)*
T_I	17.3	16	14
T_{II}	134.4	134	130
T_{III}	244.4	244	243
T_{IV}	338.4	336	337
T_V	427.1	429	424
T_{VI}		534	533
T_{VII}	629.1	624	621
T_{18}	715.6	715	
T_{20}	791.3	793	
T_{22}	870	867	
T_{24}	916.4	917	
T_{26}		961	
T_{28}		1001	
T_{30}		1032	
T_{32}	1095.8	1096	
T_{34}	1123.7	1121	
T_{36}	1190.7	1189	

The age model for our record results in more or less identical estimates for the duration and timing of the boundaries for most of the marine isotope stages as described in LR04 (table 3.1). There are, however, some mismatches beyond ~400 ka (figure 3.2). In first instance, the age for the onset of MIS 13.1 is estimated at 504.5±1.6 ka in our record, which is ~3 kyr younger than the ~508 ka estimate in LR04. The age of the basis of MIS 13.3 (i.e. T_{VI}) is ~6 kyr younger in our record (at ~526.5±1.6 ka) than in LR04 (at ~533 ka). The age estimates of both records for the youngest interstadial in MIS 15 are in generally good agreement, though we estimate the onset of MIS 15 (T_{VII}) to be much older than in LR04: 630±1.6 ka instead of 621 ka. Note that the latter is the age listed in Lisiecki and Raymo (2005), whereas our analysis of the LR04 stack indicates an age of ~624 ka. We found no large disagreements in the timing of MIS 17-23 (~650-900 ka) that transcend the uncertainty of our record. However, the onset of MIS 25 (T_{26}) is estimated ~3 kyr older, and MIS 27 ~6 kyr younger than in LR04 (figure 3.2). This gives our record a very different character in relation to insolation during this interval, even though the variability is similar to that in the open ocean stack. Our estimate for stages 28-32 agrees well with the LR04 stack again, although we note a short-lived excursion in MIS 30 that is not reflected in LR04. The age of the base of MIS 35 (T_{36}) is again in very good agreement with LR04, while the onset of MIS 33 (T_{34}), having a slightly different shape, is ~3 kyr older.

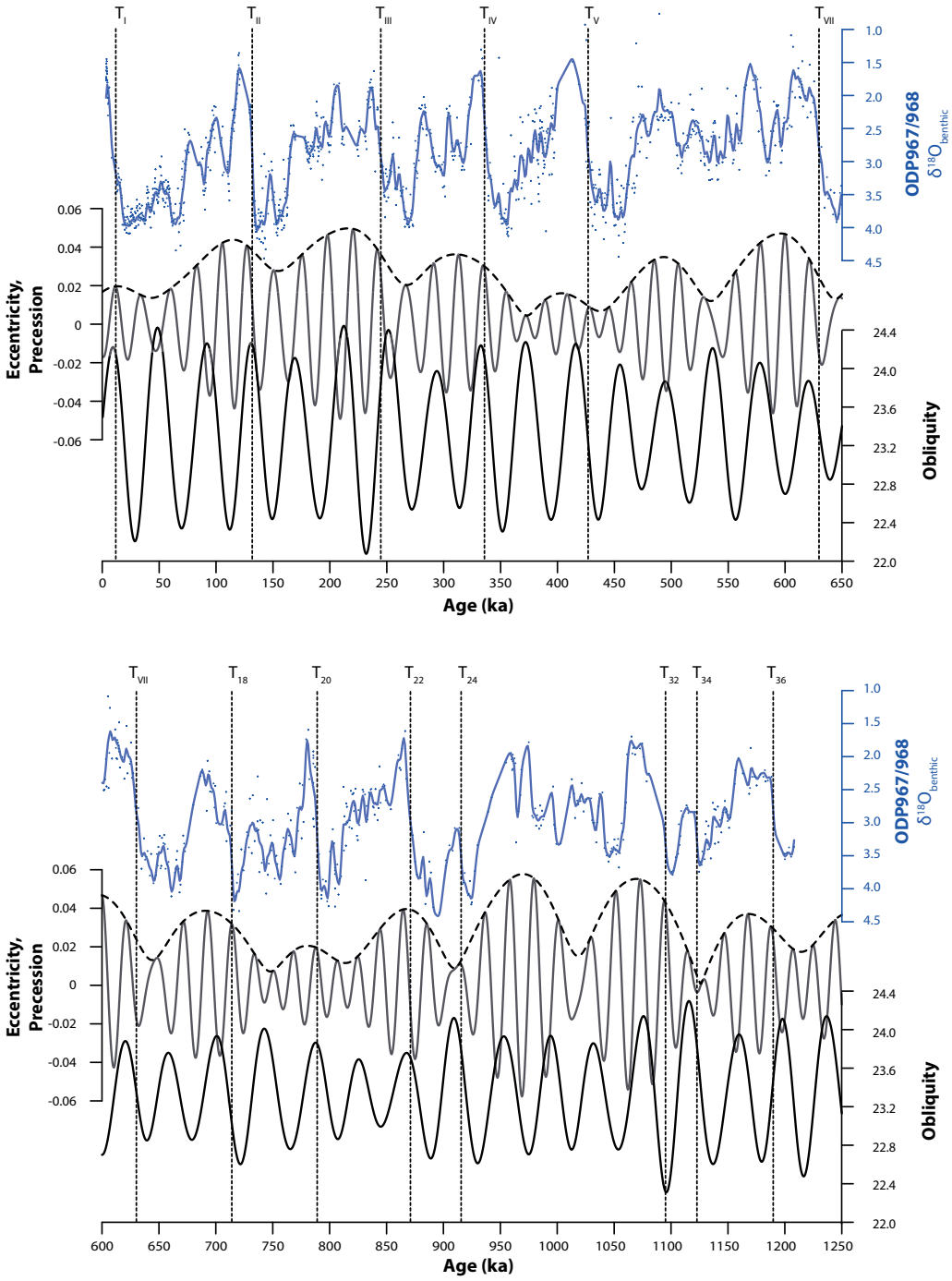

Figure 3.6: direct comparison of the Mediterranean benthic isotope record (blue dots and line, as in figure 3.1) to the orbital parameters obliquity (bottom graph in both plots), eccentricity, and climatic precession (middle graphs). Terminations are indicated by vertical dashed lines

In a next step, we compared the timing of the terminations with the astronomical parameters of precession and obliquity by estimating the phase lag between each termination and the closest onset of a precession or obliquity cycle (defined as the maximum rate of change). The results are portrayed in a phase wheel (figure 3.7), where the angle indicates the phase lag relative to each variable. Because of the considerable uncertainty involved with estimating the timing, we refrain from making statements on details. We only consider the cases where the deglaciation events cannot be related to either variable, because the timing deviates more than 1σ of the average of the terminations. This comes down to a lag of more than 12.5 kyr (5.7 kyr) to obliquity (precession), or a lead of 1.9 kyr (1.1 kyr) to obliquity (precession). Terminations T_{IIIa} (missing) and T_{VI} (unreliable) are omitted, because the nature of these deglaciations makes them unsuitable for our analysis. In addition, the isotope shift at the onset of MIS 13.3 is too small and too slow to pass the threshold in our approach.

The timing of T_{IIIb} and of T_{36} lag obliquity by more than 140° or 16 kyr. Termination T_{32} on the other hand leads obliquity by >70° or 8 kyr. However, an exact determination of the timing of T_{32} is problematic in the Mediterranean record, due to a gap in the isotope record in the later part of the termination. This might influence our analysis. T_{18} leads obliquity by 18° or 2.1 kyr. Each of these terminations have a quite realistic lag – between 30° and 70°, or ~2-4 kyr – to precession. We consider these terminations as the result of precession forcing only, and reject the possibility of obliquity as a driver. The attribution of terminations T_{36} (and potentially T_{32}) to precession supports an early onset of the MPT. On the other hand, T_{VII} and T_{34} lead precession (>60°, more than ~4 kyr), while they all have a normal (if small) lag to obliquity (between 0° and 30°, or ~0-3 kyr). We must reject precession as a driver of T_{VII}, which is remarkable because it is considered to mark the beginning of the 'full 100 kyr world' at the end of the MPT (Clark et al., 2006)

3.4 Discussion

Considering the overall high level of agreement between the ODP Sites 967/968 $\delta^{18}O$ record and the LR04 benthic stack, it is evident that our record reflects primarily changes in global ice volume and deep sea temperature. For most of the transitions and stages, our record has comparable ages to those of LR04 (table 3.1). The exceptions to this rule are (the interstadials of) MIS 13, 15, 25, 27, and 33, which deviate considerably – far more than the 1.6 kyr uncertainty estimate. In addition, we found several characteristic isotopic features in our Mediterranean benthic $\delta^{18}O$ record which were not reflected in/identical to the open ocean benthic stack LR04 (figure 3.2), namely: (1) The larger amplitude of our record with respect to the open ocean (2) Our record exhibits short-lived negative excursions immediately preceding glacial terminations. (3) some glacial inceptions appear to have a different structure, e.g. MIS 6 and 12. (4) The isotope values in our record curve more smoothly into glacial terminations, in contrast to the jagged sawtooth shapes of the LR04 stack. We can largely exclude inter-laboratory discrepancies as possible explanation for these differences, because the accuracy and analytical precision of the oxygen isotope measurements are in general high. The few gaps in our isotope record of the interval encompassing MIS 25-27 and several sapropel layers were excluded from our discussion and hence cannot explain the observed differences either. On the contrary, the largest differences we recognized occurred in the intervals which have good data coverage (figure 3.2). This implies that the aberrant features reflected in the Mediterranean benthic $\delta^{18}O$ record are most likely due to uncertainties between the two chronological approaches and the possible imprint of regional and/or local temperature and/or salinity effects.

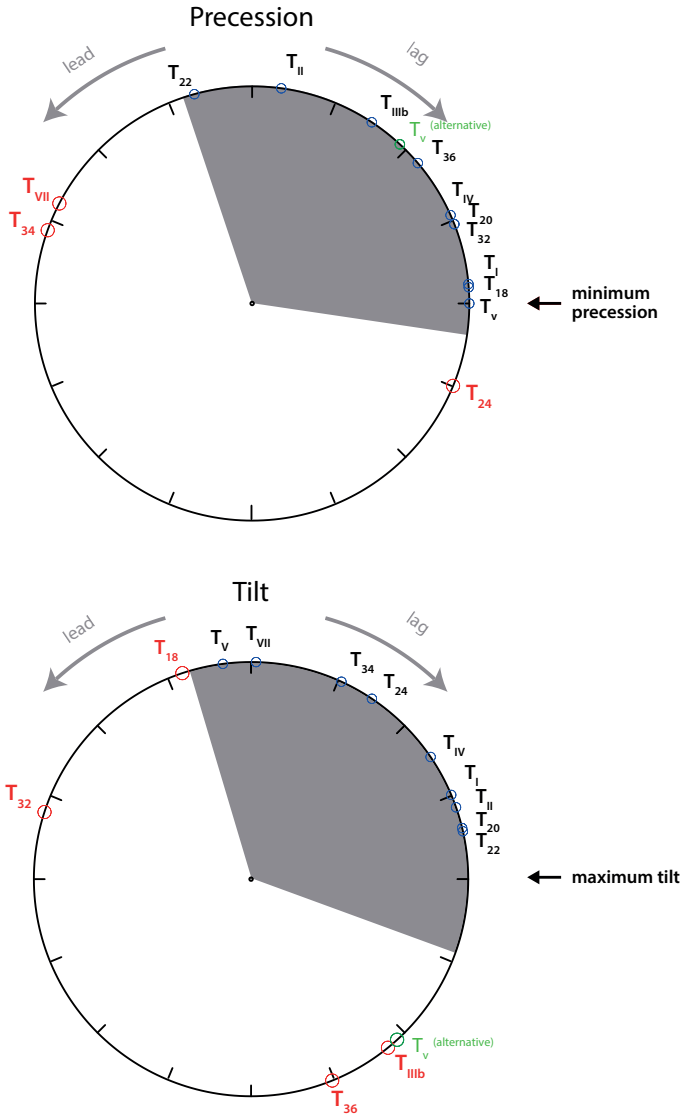

Table 3.2: the phase estimates of the terminations listed in degrees, as portrayed in figure 3.6.

Deglaciation	phase difference (in deg)	
	Precession	Tilt
T_I	85	67
T_{II}	8	71
T_{III}	33	141
T_{IV}	66	56
T_V	90	-7
T_{VII}	-63	1
T_{18}	86	-18
T_{20}	69	76
T_{22}	-15	77
T_{24}	112	34
T_{32}	69	-72
T_{34}	-70	24
T_{36}	50	158

Figure 3.7: phase wheel showing the phase estimate of the terminations as indicated in figure 3.5 with respect to the nearest onset in the cycles of obliquity (left) and precession (right). Zero degrees means no lag, 90° corresponds to a ¼λ, or ~10 kyr (obliquity), ~5 kyr (precession). Termination T_{III} (~245 ka) means $T_{III\text{-}b}$: Termination $T_{III\text{-}a}$ is not indicated because it is missing from our record. The shaded area in the graphs is the 1σ range of terminations. Terminations that fall outside this range are marked in red to indicate that they are unlikely to be triggered by this insolation variable.

3.4.1 Accuracy of the Ti/Al time scale

Our confidence in the Ti/Al-based age model is high, since the dominant precession cyclicity is readily apparent from spectral analysis of the untreated record in the depth domain (chapter 2). After tuning (to precession only), the spectral power carries great resemblance to overall insolation (figure 3.1), confirming the highly linear response of Ti/Al to the forcing. A possible source of uncertainty may however come from the constant time lag of 2.7 kyr we applied between the Ti/Al record and insolation. In comparison, the Chinese $\delta^{18}O_{speleothem}$ response to insolation has a lag varying between 0.8±0.4 kyr and 3.6±1.6 kyr. The largest deviations from the mean lag occur during the eccentricity minima, when the precession-bound signals are weak. The deviations are not systematic, i.e. no recurring faster or slower response during forcing minima, as far as our analysis can find. Therefore we have kept our tuning lag constant.

A second uncertainty may come from the tuning of sapropel S_b (figure 3.1). In chapter 2 we have tuned this sapropel to one i-cycle older than previous studies (Emeis et al., 2000; Lourens, 2004). Accordingly, the 41 kyr band pass filter we applied to our benthic oxygen isotope record follows the obliquity component of insolation well, though there are some inconsistencies during MIS 12 and 13. Here the amplitude of the filter is much smaller than in the adjacent cycles, whereas this change is not reflected in the obliquity forcing (figure 3.8). Also, the lag of the 41 kyr component to insolation is decreased in MIS 9 and 10, to an almost in-phase state. After MIS 9 the 41 kyr component continuously lags insolation again.

As an alternative, we retuned the Ti/Al record to insolation in the interval ~350-560 ka, adjusting tie points so that sapropel S_b has an age of ~407 ka, in accord with the adopted age of Lourens (2004). The corresponding ages for the isotopic record also shifted (supplementary figure 1), which mended the problems with the 41 kyr spectral band filter (supplementary figure 2): a more consistent phase behavior and no more amplitudinal irregularities. The resulting phase lag estimates for the isotopic record are ~6.8 kyr for obliquity and ~6.7 kyr for precession. More importantly, attributing S_b to a later i-cycle also shifts T_v, which occurs at about the same depth, to 411.3 ka. This contradicts both the LR04 and EDC chronologies for this termination, but agrees with Shackleton (1995), who also placed T_v at ~410 ka.

A major consequence of this alternative tuning is the radical change in sedimentation rate at the MIS12-MIS11 transition (supplementary figure 3). Also, a ~15 kyr mismatch in the LR04 benthic stack would have a pronounced influence on the global mean sedimentation rate estimates, which is a powerful argument against such a revision in this well resolved interval of the stack (Lisiecki and Raymo, 2005). Finally, while the spectral filter for the isotopic record was improved, the spectral filters for the Ti/Al record were negatively affected by the change in tuning (supplementary figure 3a, b), illustrating that the alternative tuning does not match insolation forcing as well as in the original tuning (chapter 2).

3.4.2 Regional temperature and salinity effects

The larger glacial-interglacial amplitude of the Mediterranean benthic $\delta^{18}O$ record most likely implies a direct influence of regional temperature and salinity changes in the semi-enclosed Mediterranean basin over glacial-interglacial time scales (Rohling, 1999; Rohling et al., 2014). Also, sapropels – the well-known precession-controlled perturbations in the regional temperature and salinity conditions of the Mediterranean basin – seem to have shaped the benthic $\delta^{18}O$ record. Most clearly are the precession-related short-lived excursions depicted in the record during MIS 6, 8, 12, and 14, that are not reflected in the open ocean benthic stack LR04 (figure 3.2). These small excursions just prior to deglaciations are also found in the sea level reconstructions of the Red Sea

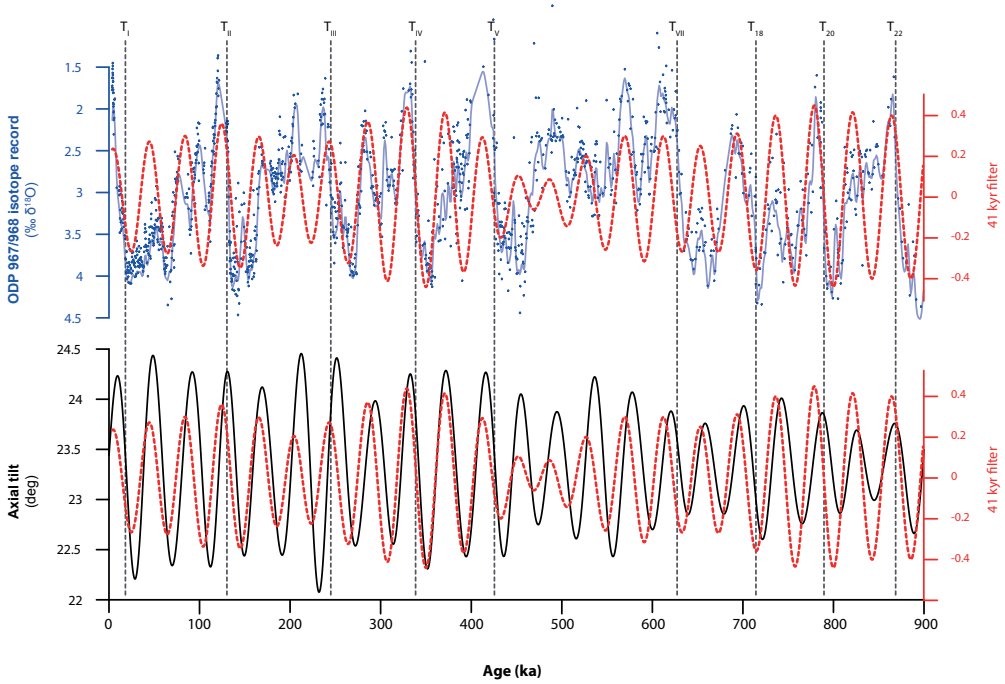

Figure 3.8: a spectral bandpass filter centered on 41 kyr (frequency 0.0241±0.005; dashed red line) versus the Mediterranean isotope record (blue dots and line) and versus obliquity (black line).

over the past 500 ka (Siddall et al., 2003; Rohling et al., 2009; Grant et al., 2012), suggesting that a regional hydrological effect is in play in both basins, thus possibly connected to changes in the low-latitude climates such as the monsoon. However, because similar features were also found in the Antarctic Epica Dome C (EDC) ice core δDeuterium (δD_{ice}) record (Rohling et al., 2009), it seems more likely that these excursions are linked to and hence reflect global sea level changes (Rohling et al., 2014), which are evidently not resolved by the LR04 record.

Another marked difference is the shouldered slopes (i.e. early return to interglacial values) found at the onset of the deglaciations of MIS 10, 12, 16, and 22 in our record that seem to coincide with the most severe glacial values in LR04 (figure 3.2). These features generally occur in phase with or just before an increase in Northern Hemisphere summer insolation. We hypothesize that during these periods of relatively low insolation and extreme cold conditions in the North Atlantic region, the overall evaporation in the Mediterranean basin is low, thereby reducing the overall salinity values and hence concomitant $\delta^{18}O$ values of the eastern Mediterranean deep water that flows along these drill sites (Robinson et al., 1992).

To summarize, regional and/or local temperature or salinity changes in the Mediterranean can explain the observed differences in shape and expression of the short-lived isotopic features between our record and LR04, noting that in particular the precession-related excursions were also found in records outside the Mediterranean realm. As a result, the Mediterranean $\delta^{18}O$ record has gained a less asymmetric saw tooth appearance through the late Pleistocene glacial cycles than LR04. This increased (pseudo) symmetry may have affected the average phasing of the orbital band pass filters and hence could explain the observed smaller time lag than assumed by LR04. Most of the glacial-

interglacial transitions however are, due to the magnitude of the isotope shift, so distinct that the offset due to regional and local effects ought to be negligible compared to the total discrepancies found between the records. Another source of uncertainty may stem from the LR04 chronology.

3.4.3 Chronological uncertainties in LR04

Incongruencies in age between the EDC δD_{ice} record and the LR04 benthic isotope stack were discussed by Parrenin et al. (2007) for their EDC3 time scale. In particular, the clear offset of +6 kyr they found between both chronologies for MIS 13. The EDC3 time scale is based on a detailed ice accumulation and flow model in combination with tuning of $\delta^{18}O$ from atmospheric O_2 in ice bubbles to insolation. The recently published Antarctic Ice Core Chronology 2012 (AICC2012) however changes the onset of MIS 13 considerably (Bazin et al., 2013). Bazin et al. (2013) omitted a tuning marker at ~532 ka, arguing it caused fluctuations in their ice accumulation model. This results in the deuterium record lining up with LR04 to an age estimate of 533 ka for the onset of MIS 13. Even with the large uncertainty range involved with the estimates (±6 kyr for EDC – Dreyfus et al., 2007; Bazin et al., 2013), the synchronicity between the AICC2012 chronology and the LR04 suggests our estimate to be incorrect. It could be that the Ti/Al age model is less accurate because of a lack of tie points due to the broad insolation maximum around 530 ka. Considering the double sapropels in this same interval (figure 3.1), it is also likely that local influences on our benthic isotope record disturb the estimate.

Apart from MIS 13, Parrenin et al. (2007) discussed the timing of termination T_{VII}, which leads LR04 by ~3kyr. There is little change in the timing of this deglaciation in the AICC2012 chronology, at ~629 ka (Bazin et al., 2013). This estimate agrees with our age estimate of termination T_{VII} at 630±1.6 ka (figure 3.9). The listed LR04 estimate (621 ka) is well outside our age uncertainty.

Beyond T_{VII}, the lowest part of the EPICA Dome C record, there are more discrepancies between LR04 and the deuterium data, ranging from -2 kyr to +8 kyr. In this interval, our record is more closely aligned with LR04, disagreeing with the AICC2012 chronology (figure 3.9). This suggests that, whatever caused the later exceptions, for the period of ~650-900 ka the LR04 tuning is consistent with our Ti/Al based age model. Following this argument to its logical conclusion, this in turn would suggest that the AICC2012 chronology is marginally flawed in the lowermost part of the record, or that there are processes in play that affect each proxy differently.

Until now we have tacitly assumed that changes in benthic $\delta^{18}O$ occur more or less simultaneously in different basins throughout the Pleistocene. Recent work (Skinner and Shackleton, 2005; Lisiecki and Raymo, 2009) has shown, however, that there is a significant mismatch between the Pacific and the Atlantic basin, with T_I-T_V in the Pacific lagging the Atlantic by an average of ~1600 yrs (Lisiecki and Raymo, 2009). Unfortunately, there is no measure for any possible lag between the Mediterranean and the Atlantic because no benthic oxygen isotope record of sufficient length and resolution was available. This problem is discussed in greater detail in chapter 4. We note here that, for T_I-T_V, we found no significant mismatch between our benthic record and the average (Atlantic and Pacific) ages published for the LR04 benthic stack. In addition, our record leads LR04 in some stages, but significantly lags the benthic stack at other intervals. There does not seem to be a systematic deviation of Mediterranean benthic isotopes with regard to the average of the LR04 benthic stack. Our age model therefore provides an alternative to the one published by Lisiecki and Raymo (2005). We have retuned the LR04 stack accordingly and have made it available online.

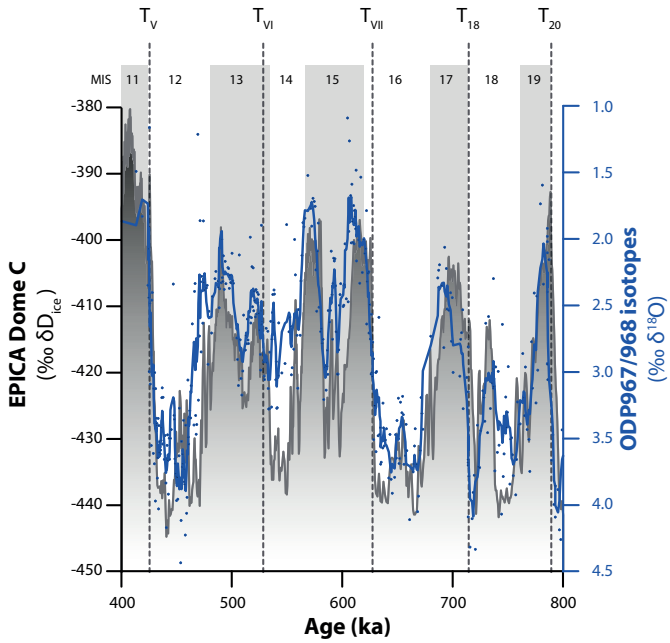

Figure 3.9: direct comparison of the Mediterranean benthic isotope record (blue dots and line) to the EDC δD_{ice} (Jouzel et al., 2007; Bazin et al., 2013), for MIS 11-19. As in figure 3.2.

3.4.4 Phase of ice volume changes and glacial terminations

The disagreements between our record and the LR04 age model imply that the response of global ice volume and climate to insolation forcing is not as systematic as assumed by the Imbrie and Imbrie (1980) model. This may in part be due to the changes in the climate system responsible for the MPT. The shifting response of ice sheets, and with them global climate, from the obliquity to the precession parameter is difficult to capture in one tuning model.

Using phase estimates (figure 3.7) we have tried to identify which orbital parameter is likely to have caused each glacial-interglacial transition in the past ~1.2 Ma. Based on this analysis we exclude obliquity as a possible forcing for the onset of MIS 7, 17, 31, and 35. The exclusive role of precession forcing inferred for MIS 35 puts the onset of the MPT not later than ~1.2 Ma, consistent with the findings of Clark et al. (2006) and Dupont et al. (2001). The obliquity parameter remains important throughout the Pleistocene, as is clear by the timing of T_{VII}, and T_{34}. For T_{VII}, which is at the end of the MPT where the 100 kyr cycle is commonly regarded to be well established (e.g. Mudelsee and Stattegger, 1997; Clark et al., 2006), precession is unlikely to have influenced the timing of the deglaciation. The isotope shift occurs ~9 kyr earlier than estimated by LR04 and other authors (e.g. Shackleton et al., 1995; Huybers and Wunsch, 2004) but not the AICC2012 (Bazin et al., 2013), which times the transition at ~628 ka. That is within our uncertainty estimate. Such an early transition cannot be the result of precession forcing because it leads the nearest precession cycle by 62°, or ~3.6 kyr (figure 3.7). A combination of the parameters (Huybers, 2011) is also not likely, because the maximum rate of change in 65°N June 21st insolation – combining both precession and obliquity – occurs at or around the same time as the shift in precession, which would result in a similar phase relation. Our findings therefore suggest that this transition is forced solely by obliquity.

The phase wheel in figure 3.7 does not unambiguously show a difference in response time of global climate to insolation between the middle and the late Pleistocene. We therefore look to the cross-spectral analyses performed on the intervals in the record before and after ~0.9 Ma. These provide a more general estimate for the interval, instead of snapshots of individual transitions. We place the boundary here because it is the clearest single long term shift in climatic behavior (Mudelsee and Schulz, 1997; Elderfield et al., 2012; this study). The cross-spectral analyses over the intervals before and after 0.9 Ma show the phase lag of the isotope response to obliquity was likely to be considerably (~2.7 kyr) shorter in the Early Pleistocene than in the last 900 ka (figure 3.5). These estimates stray significantly from those inferred (by e.g. Lisiecki and Raymo, 2005) from the model of Imbrie and Imbrie (1980), suggesting a much less systematic response than assumed in literature. Also, we have assumed that the lag in Ti/Al remains constant at 2.7 kyr throughout the record. It is likely that this lag would have been smaller in the Early Pleistocene (Ziegler et al., 2010), causing an even larger difference in the inferred MIS ages.

3.5 Conclusions

We present the first long, high-resolution benthic isotope record from the Eastern Mediterranean Sea. It reflects all the glacial and interglacial stages and interactions of the last ~1200 kyr present in the LR04 benthic stack. Using sediment geochemistry to create our age model we establish independent age estimates for the timing and duration of the Marine Isotopic Stages of the Pleistocene. We arrive at different ages for some isotopic stages compared to the LR04 benthic stack before MIS 11. (An updated age model for the LR04 benthic stack is provided in the supplementary material.) We attempt to use our additional age control to pinpoint the influence of the orbital parameters obliquity and precession in triggering deglaciations. Though large uncertainties are involved, evidence indicates that terminations T_{32} and T_{36} might be attributable to precession. This is a argues for an early (>1200 ka) onset of the MPT. Vice versa, the ~9 kyr earlier onset of T_{VII} compared to LR04 can only be explained as a response to obliquity forcing.

Spectral cross-correlation analysis of the record reveals significant amounts of power in the obliquity and precession range, with an average lag of 5.5±0.8 kyr for obliquity, and 6.0±1.0 kyr for precession. Separate analysis of the intervals before and after ~900 ka however reveal a lag of 3.0±3.3 kyr to obliquity in the Early Pleistocene, and a lag of 5.7±1.1 kyr in the Late Pleistocene. Our findings suggest that earth climate behaves less systematic with regard to insolation forcing than predicted by the deterministic approaches of Imbrie et al. (1984), Shackleton (1995), and Lisiecki and Raymo (2005).

Acknowledgements: This project was financially supported by NWO-ALW (project number 865.10.001). We kindly acknowledge the Ocean Drilling Program in general, and Walter Hale and the Bremen Core Repository specifically for the samples used in this study. Special thanks go to Astrid Vrijhoef for her assistance in lab work. Two anonymous reviewers provided extensive feedback, helping to improve the manuscript considerably.

This work was initiated by L.J. Lourens. Lab work and analyses were performed by M. Ziegler and T.Y.M. Konijnendijk. T.Y.M. Konijnendijk wrote the manuscript, with contributions of the other authors.

It is the peculiar quality of a fool to perceive the faults of others and to forget his own.

Marcus Tullius Cicero

Chapter 4

On the timing of late Pleistocene terminations: Inferences from benthic $\delta^{18}O$ records of the Atlantic, Pacific, and Mediterranean basins

T.Y.M. Konijnendijk[1,], M. Mojtahid[2], R. Hennekam[3], G.J. de Lange[1], M. Ziegler[1], L.J. Lourens[1]*
[1]: Utrecht University, Faculty of Geosciences, Institute for Earth Sciences
2: université d'Angers, France
3: NIOZ, Texel

4.1 Introduction

Glacial terminations are regarded as effectively globally synchronous events, and have as such been used by Lisiecki and Raymo (2005), amongst other features, in aligning the benthic $\delta^{18}O$ records of 57 cores in their widely accepted global benthic stack (LR04). Skinner and Shackleton (2005) showed, however, that this assumption of global synchronicity does not hold. More specifically, from their highly detailed, ^{14}C constrained study of the last glacial termination, they concluded that the increase in benthic $\delta^{18}O$ values of one sediment core from the Iberian Margin (MD99-2334K) in the North Atlantic is ~3900 years off from that found in the deep eastern equatorial Pacific (TR-163). Following this approach, Lisiecki and Raymo (2009) subsequently separated the Atlantic and Pacific records in their renewed stack of the past 800 ka, and found indications for diachronous termination signals for the last five terminations. They estimated the Pacific to lag the Atlantic basin by 1.6 kyr on average, with lags up to 4 kyr at termination T_{II} (~128 ka) and T_{IV} (~330 ka).

The findings of Skinner and Shackleton (2005) were further confirmed by Waelbroeck et al. (2011), who studied nine ^{14}C-dated cores along a north-south transect in the Atlantic to investigate the behavior of the different water masses in the basin over the course of the last deglaciation. They found large differences in pattern and timing of between the cores, which they considered as proof that there is no global synchronicity in deglaciation. According to Waelbroeck et al. (2011), evidence of deglaciation first occurred in the intermediate North Atlantic triggered by brine waters transporting ^{16}O-rich water downwards during Heinrich stadial 1 (HS1). The deep North Atlantic sites responded later, and the South Atlantic waters were only ventilated after HS1 with the resumption of North Atlantic Deep Water formation. Note that Skinner and Shackleton (2005) explained the time discrepancy between the Pacific and North Atlantic in terms of a delayed deep water temperature response in the former, based on Mg/Ca measurements. These indeed indicate a delayed warming, but the magnitude of the temperature response (~1˚C) is far too small to explain the $\delta^{18}O$-discrepancy (~1‰). They do not consider localized $\delta^{18}O$ effects because, they argue, the deep Pacific is too large a reservoir to be influenced by them.

More recently, Stern and Lisiecki (2014) made a targeted attempt to disentangle the age of termination T_I in the different ocean basins. They tried to test when light $\delta^{18}O$ water reaches the separate basins by compiling seven regional stacks reflecting the intermediate and deep North and South Atlantic, the intermediate and deep Pacific, and the intermediate Indian oceans. Each of these stacks was carefully aligned using the Match protocol (Lisiecki and Lisiecki, 2002), and with strong age control in the form of independent ^{14}C age models based on planktonic foraminiferal carbonate. They find the earliest onset of deglaciation at ~18.5 ka in the intermediate waters masses of the South Atlantic, followed by slightly delayed onset in the other Atlantic stacks and the deep Pacific at ~17.5 ka, the intermediate water masses in the Pacific at 16.5 ka and finally the intermediate water masses in the Indian Ocean at 14.5 ka.

The approximately 4000 yr difference between different ocean basins reported by Stern and Lisiecki (2014) seems at first glance consistent with the estimate of Skinner and Shackleton (2005). However, Skinner and Shackleton (2005) compared the timing of the final isotopic shift into full interglacial values, while Stern and Lisiecki (2014) compared the onset of deglaciation, and found a much smaller difference (~2kyr) between the basins in the finishing stages of the deglaciation. Another discrepancy is that the ~4 kyr difference found by Skinner and Shackleton (2005) relates to the difference between the deep North Atlantic and deep Pacific basins, while that of Stern and Lisiecki (2014) concerns the difference between the intermediate water masses of the South Atlantic and Indian Ocean basins. Stern and Lisiecki (2014) found a much smaller difference in timing (~1 kyr on average) of the deglaciation between the deep Atlantic and Pacific basins, and argued that the large lag found by Skinner and Shackleton (2005) is due to local effects.

In 2010, Ziegler et al. presented the first high-resolution benthic $\delta^{18}O$ record of the Eastern Mediterranean basin over the past 375 ka, which was recently extended down to 1.2 Ma (chapter 3). A major advantage of this eastern Mediterranean $\delta^{18}O$ record of ODP Sites 967/968 is its independent age control. While the open ocean records are based on ^{14}C-dating and orbital tuning of the glacial-interglacial $\delta^{18}O$ variability, the age control our studied materials comes from tuning the dominantly precession-controlled geochemical signature of the sediments to the insolation times series (Lourens et al., 1996; 2001; Ziegler et al., 2010; chapter 2).

In light of the diachronicity in timing of the glacial terminations as discussed above, it is vital to review the behavior of isotopes in the Eastern Mediterranean compared to other locations. Especially considering that this semi-enclosed basin has many hydrographic features quite distinct from global ocean circulation. We compare T_I in the benthic isotope record of ODP Site 968 in the eastern Mediterranean (Ziegler et al., 2010) to the available, absolutely dated open ocean records, to see how the Mediterranean record feeds into this discussion. In addition we use shallow benthic data from site PS009PC, also in the eastern Mediterranean, which has been ^{14}C dated (Hennekam et al., 2014; this study). We use the results of this comparison to assess which basin the Mediterranean response resembles the most, and to gauge the limits within which we can comment on global stratigraphy. Finally, we compare the ODP Site 967/968 isotope data to the separate Atlantic and Pacific stacks of Lisiecki and Raymo (2009) to explore if there are structural differences between the records over the previous four terminations.

4.2 Materials and Methods

ODP Site 968 (34°20'N, 32°45'E) was drilled south of Cyprus (figure 4.1) on the slope of Eratosthenes seamount at a water depth of 1,961 m (Emeis et al., 1996). The age model (Ziegler et al., 2010) consists of tuning the color reflectance of the sediment at 550 nm (a proxy for

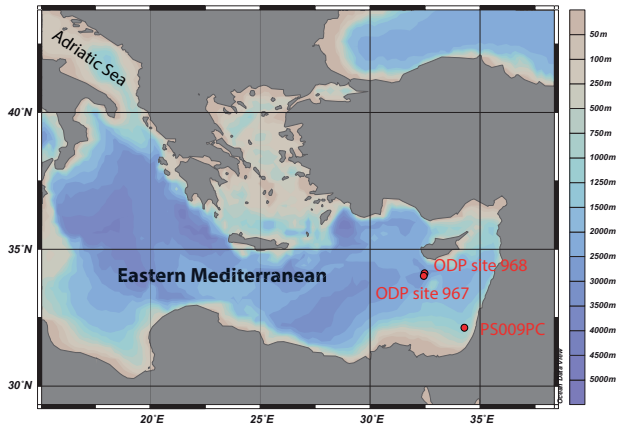

Figure 4.1: overview of the eastern Mediterranean basin. The locations of the Mediterranean cores used in this study are indicated with red dots.

monsoon activity on the North African continent) to the Chinese Sanbao-Hulu speleothem record of Wang et al. (2008), and the geographically closer Soreq speleothem record of Bar-Matthews et al (2003). Highly detailed correlations of millennial scale features allow for fine tuning of this age model. Additional age control in the interval under discussion is provided by the upper and lower boundaries of sapropel S1, which have been extensively carbon-dated and are assumed to be synchronous basin-wide (de Lange, 2008). The terminations beyond ~300 ka (T_{IV} and T_V) are based on the tuning of the elemental ratio of titanium to aluminum to precession, with an uncertainty of ~1.6 kyr (Lourens et al., 2001; chapter 3). This part of the record also uses data derived from adjacent ODP Site 967 (34°04'N, 32°43'E, 2554m depth), which is combined into one splice (chapter 2).

Piston core PS009PC (32°07.7'N, 34°24.4'E, 552m water depth; Hennekam and de Lange, 2012) was taken during the PASSAP cruise with the R/V Pelagia in May 2000. This coring site is located in the southeast margin of the eastern Mediterranean (figure 4.1). The age model for PS009PC (Hennekam et al., 2014) was constructed based on seven ^{14}C AMS measurements on planktonic foraminiferal samples of PS009PC. The ^{14}C analyses were performed at the Poznań Radiocarbon Laboratory in Poland. For conversion to calendar ages the OxCal 4.1.7 program was used (Ramsey, 2009), and the Marine'09 data set was used for calibration (Reimer et al., 2009) with a local reservoir correction (ΔR) of 21± 63 year based on ^{14}C analyses of recent shell material near the core locality [Reimer and McCormac, 2002; Boaretto et al., 2010]

The location of piston core PS009PC is fed by Levantine Intermediate Water (LIW), which flows between 200 and 600 m in the eastern Mediterranean (Wüst, 1961). This water is formed after the Atlantic surface water flowing in at the Strait of Gibraltar has increased in salinity through continuous net evaporation on its way to the east. In winter, the surface water in the northeast seas of the eastern Mediterranean cools down and sinks to intermediate depth (Wüst et al., 1961; Nittis and Lasceratos, 1998; Lasceratos et al., 1999). In the Adriatic Sea, LIW is mixed with surface waters during cold winters to form dense Eastern Mediterranean Deep Water (EMDW). This relatively homogeneous deep water mass (Lasceratos et al., 1999) fills the eastern Mediterranean between 1500 and 3000 m depth (Wüst, 1961), and bathes ODP Sites 967 and 968. PS009PC and ODP Site 967/968 therefore represent both the intermediate (LIW) and deep (EMDW) eastern Mediterranean.

4.3 Results

4.3.1 Eastern Mediterranean benthic $\delta^{18}O$ records

The PS009PC record has a slightly higher range in $\delta^{18}O$ values than ODP Site 968 (figure 4.2), starting at ~4.5‰ during the Last Glacial Maximum (LGM) and ending stably at ~2.0‰ in the Holocene. ODP Site 968 $\delta^{18}O$ values are constant at ~4.0‰ in the LGM and range around 2.0‰ in the Holocene. The PS009PC values are thus 0.5‰ heavier than ODP Site 968 in the earliest part of the record. We attribute the difference to ontogenetic effects between the different species measured. The PS009PC $\delta^{18}O$ record was based on the species *U. peregrina* and *U. mediterranea*, while this part of the EMDW record was based on *C. kullenbergi*. The discrepancy is close to the 0.6‰ difference reported for these species in literature (Mix et al., 1995). Note that the upper part of the ODP Site 968 $\delta^{18}O$ record is based on *G. neosoldanii* and *G. altiformis*. We could not find a detailed comparison of these species in literature. Analysis of paired measurements of *C. kullenbergi* and *G. neosoldanii* (37 pairs) and of *C. kullenbergi* and *G. altiformis* (22 pairs) reveals little differences: 0.28‰ and 0.04‰ respectively. Both estimates fall within one standard deviation of 0‰ and are statistically indistinguishable.

We subsequently compared the (combined) temperature and salinity effects on both records (figure 4.2) by removing the (global) glacioeustatic $\delta^{18}O$ component, which we derive from the relative sea level data of Lambeck and Chappell (2001) and a glacial-interglacial deep water change in $\delta^{18}O$ of ~1.0‰, following Skinner and Shackleton (2005). Note that we did not remove the ontogenetic effect of *U. peregrina* and *U. mediterranea*, because of the uncertainty involved in the magnitude of the offset and the limited added value for our analysis. Both $\delta^{18}O$ records declined significantly at the onset of HS1, ~17.5 ka. During most of HS1 until the beginning of the Younger Dryas (YD), the values of both records level off and are tied close together around 3.4‰. This indicates that the LIW warmed significantly more than EMDW during this interval. In the YD there is increased hysteresis when the PS009PC $\delta^{18}O$ values turn heavier, implying a cooling at intermediate water depths. This is consistent with the findings of Bard et al. (2000) and Cacho et al. (1999), who found strong cooling of the surface waters in the Iberian Margin and Alboran Sea, respectively, during the YD. The ODP Site 968 $\delta^{18}O$ record shows lighter values in this interval. A change to warmer or less saline waters seems unlikely during the YD, indicating that a shift in $\delta^{18}O$ of the source water for LIW is the most likely cause, e.g. more ^{18}O-depleted water feeding into the Adriatic where the LIW is formed, such as Alpine meltwater.

After the YD, isotope values in both eastern Mediterranean cores rapidly shift towards the light Holocene values. The ODP Site 968 $\delta^{18}O$ record is interrupted within the sapropel, S1 (figure 4.2). Only one data point is present in this core at ~8.2 ka, possibly indicative of a brief oxygenation of the deeper waters (Rohling et al., 1997; Rossignol-Strick 1999). At the end of S1, the ODP Site 968 $\delta^{18}O$ record resumes and joins the Holocene values of PS009PC.

Assuming a comparable interspecies' difference between *Uvigerina* and *Gyroidina* as with *Cibicides* in the lower interval, this indicates that the LIW warmed considerably more during deglaciation than the EMDW, of which most warming occurred during the initial stages of HS1.

4.3.2 Termination I in the Mediterranean and the open ocean

We start by comparing our eastern Mediterranean $\delta^{18}O$ records to the nearest basins discussed by Stern and Lisiecki (2014), the intermediate and deep North Atlantic (figure 4.3). These are adjacent to and connected with the Mediterranean basin, although the source of deep water formation is different for the basins and they should have limited direct influence on each other. As has been discussed in chapter 3, the $\delta^{18}O$ values of the open ocean on average are different from the

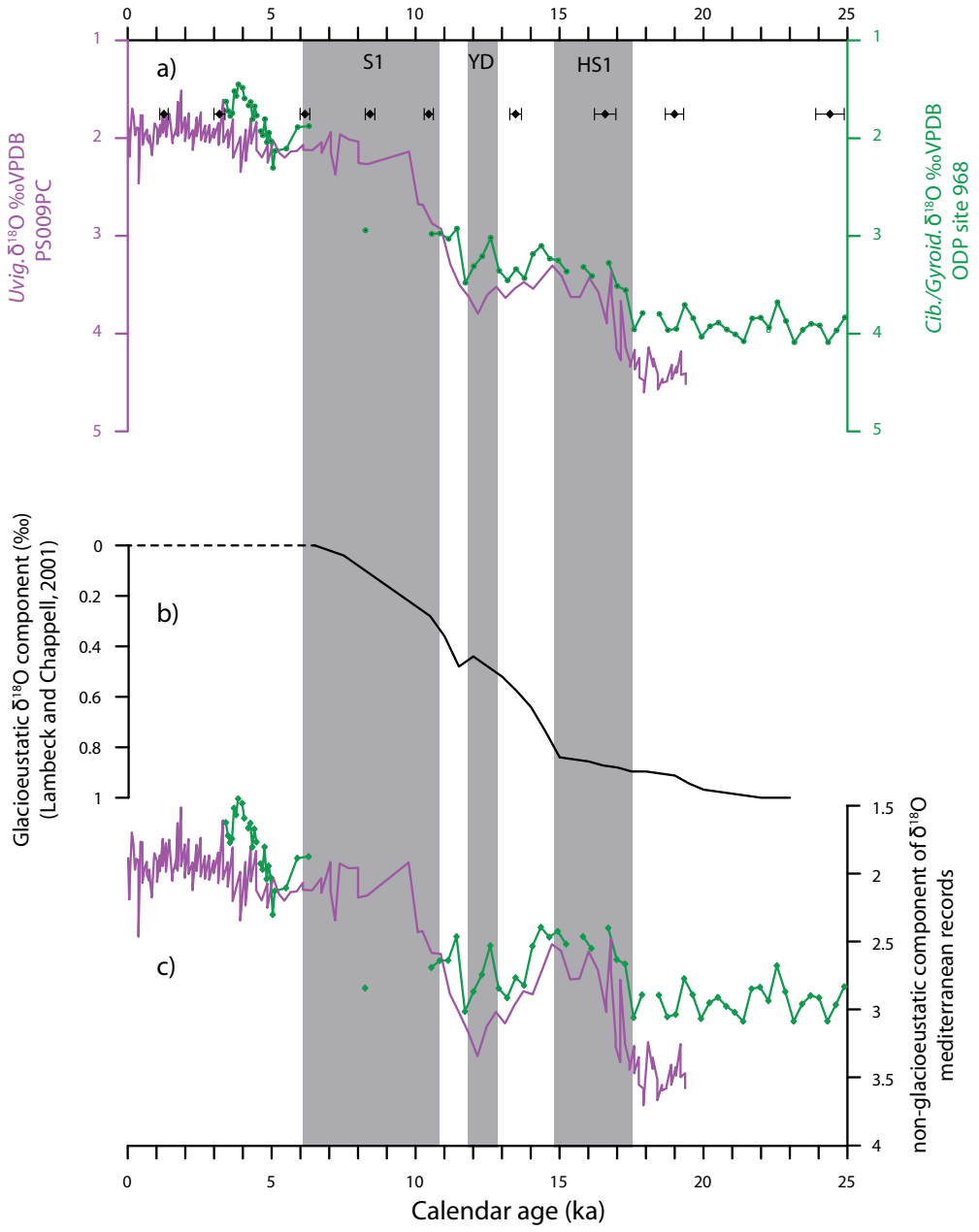

Figure 4.2: a) Intermediate Mediterranean $\delta^{18}O$ record (pink) and the Deep Mediterranean $\delta^{18}O$ record (green) over the last 25 ka. Radiocarbon dates of the intermediate record are indicated with black dots (including 2σ error bars) b) the glacioeustatic $\delta^{18}O$ component of seawater, based on the sea level estimates of Lambeck and Chappell (2001) and a 1.0% glacial – interglacial change in deep water $\delta^{18}O$, as estimated by pore-water analyses (Schrag and DePaolo, 2002), and c) the non-glacioeustatic $\delta^{18}O$ of the intermediate and deep Mediterranean. Pervasive global/regional events such as the last Heinrich stadials (HS1), the Younger Dryas (YD), and sapropel S1 are indicated with grey bars.

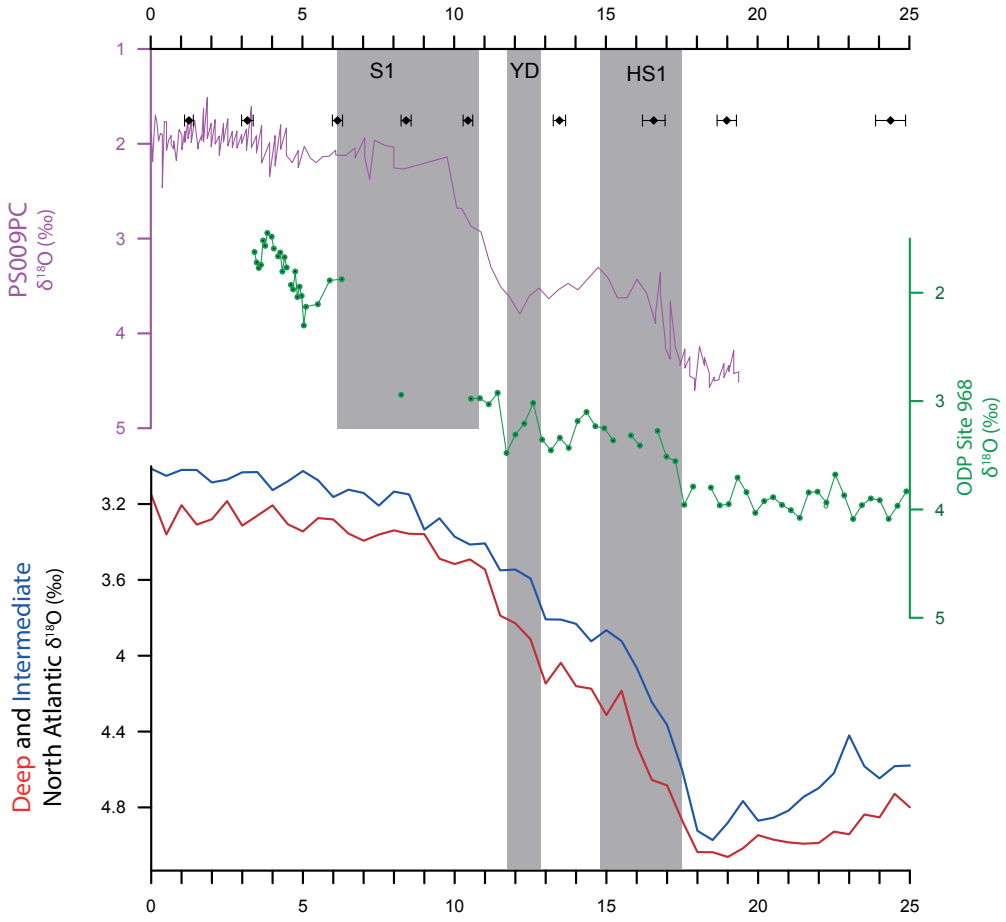

Figure 4.3: The Mediterranean records compared to the Intermediate North Atlantic (blue) and Deep North Atlantic (red) stack of Stern and Lisiecki (2014). Shaded bars indicate known pervasive climate events as in figure 4.2.

Mediterranean and have smaller amplitudes. The $\delta^{18}O$ values range between ~5.0‰ during the LGM to ~3.1‰ during the Holocene (for the Intermediate North Atlantic; for the Deep North Atlantic, Holocene values are ~3.3‰).

The onset of deglaciation in both the Deep and Intermediate North Atlantic is estimated to be at 17.5 ka (Stern and Lisiecki, 2014), exactly the same time as the LIW estimate (figure 4.3). The ODP Site 968 $\delta^{18}O$ record – which has slightly lower resolution – places the onset of deglaciation between 17.3 and 17.6 ka. There is therefore no discernible difference in timing of the onset of T_I between the eastern Mediterranean intermediate and deep waters, and the Intermediate and Deep North Atlantic. The latter records both show a temporary drop in the rate of $\delta^{18}O$ change at the end of HS1, which increased again at the onset of the YD. Both records gradually reached Holocene values.

While the deglaciation in the Intermediate and Deep North Atlantic records slows down at the end of HS1, it doesn't quite level off as it does in the eastern Mediterranean. Also, the slowdown of $\delta^{18}O$ change occurs earlier in the Mediterranean than in the open ocean stacks. We attribute part of

these differences to the internal variation of records included in the Intermediate and Deep North Atlantic stacks. Some of these records exhibit considerable slowdown in the $\delta^{18}O$ rate of change, while others show continuous increase; to illustrate the variability within the North Atlantic basins, we compare the records presented by Waelbroeck et al. (2011) to our own (figure 4.4). The benthic record of MD95-2037 (Labeyrie et al., 2005; Gherardi et al., 2009), located on the mid-Atlantic ridge at about the same latitude as the Mediterranean, shows a very similar stepwise pattern in deglaciation. On the other hand MD99-2334K (Skinner et al., 2003), located on the Iberian Margin, shows an uninterrupted deglaciation pattern. These pronounced differences are averaged out in the Deep North Atlantic stack of Stern and Lisiecki (2014). Considering the large internal variation in these records (figure 4.4), both in pattern and in timing of the features, we regard the similarity between the Mediterranean records and the open ocean stacks as good.

The Intermediate and Deep North Atlantic records indicate accelerated deglaciation rates at the onset of the YD, while both Mediterranean records show a resumed deglaciation at the end of the YD. The rates of change in the eastern Mediterranean are higher so that Holocene values are reached by 10 ka. This is sooner than in the open ocean stacks of Stern and Lisiecki (2014), which slow down into a Holocene plateau more gradually, and only attain it at ~9 ka (figure 4.3). Overall the total deglaciation happens in much the same time frame, between ~17.5 ka and 9-10 ka.

4.3.3 Terminations T_{II}-T_V

We compare the merged ODP Site 967/968 $\delta^{18}O$ record (Ziegler et al., 2010; chapter 3) to the separate stacks for the Atlantic and Pacific basins ($LR09_{Atl}$ and $LR09_{Pac}$) constructed by Lisiecki and Raymo (2009). These stacks exhibit distinctive behavior, with the onset of deglaciation beginning earlier in $LR09_{Pac}$ (T_{II}, T_{IV}) or both stacks simultaneously (figure 4.5). Deglaciations proceed quicker in $LR09_{Atl}$ than in $LR09_{Pac}$, resulting in the average lag between the Atlantic and Pacific basins of ~1.6 kyr reported by Lisiecki and Raymo (2009). Our ODP Site 967/968 benthic $\delta^{18}O$ record compares quite well for T_{II} and T_{III}, with the onset, slope and end of deglaciation closely resembling those of the LR09 stacks (figures 4.5a, b). The final stages of T_{II} and T_{III} are obscured in our record by the lack of data within sapropel S5 and S9, respectively. However, the overall picture is that there are negligible differences in timing between the Mediterranean $\delta^{18}O$ signal and the open ocean stacks for T_{II} and T_{III}.

The ODP Site 967/968 benthic $\delta^{18}O$ record shows a small (~1kyr) lead for T_{IV} for the steepest part of the slope with respect to the open ocean, though this falls well within the 1.6 kyr uncertainty estimate of our age model (chapter 3). Deglaciation seems to be completed simultaneous to $LR09_{Atl}$, with $LR09_{Pac}$ deglaciation slowing down at the same point (figure 4.5c).

The largest difference in timing between the benthic $\delta^{18}O$ record of ODP Site 967/968 and the open ocean stacks is found for T_V (figure 4.5d). During this termination, our eastern Mediterranean record seems to lead those from the open ocean. Part of this apparent lead can be explained by the fact that in general maximum glacial values and the onset of deglaciation are found significantly earlier in the eastern Mediterranean record than in both open ocean stacks (figure 4.5e). In particular, where the benthic $\delta^{18}O$ record of ODP Site 967/968 curves smoothly into deglaciation, the open ocean records show a jagged saw tooth pattern (chapter 3). This difference is most pronounced for T_V, where maximum glacial values are reached at ~452 ka, approximately 20 kyr before those recorded in the open ocean stacks (figure 4.5e). However, the benthic $\delta^{18}O$ values in ODP Site 967/968 fluctuate for some time, and the actual inflexion to deglaciation occurs later, at ~433 ka (figure 4.5d,e), which is much closer to the open ocean estimate. The result is that T_V seems to lead the open ocean stacks a great deal, but the lead is estimated to be only ~1.9 kyr

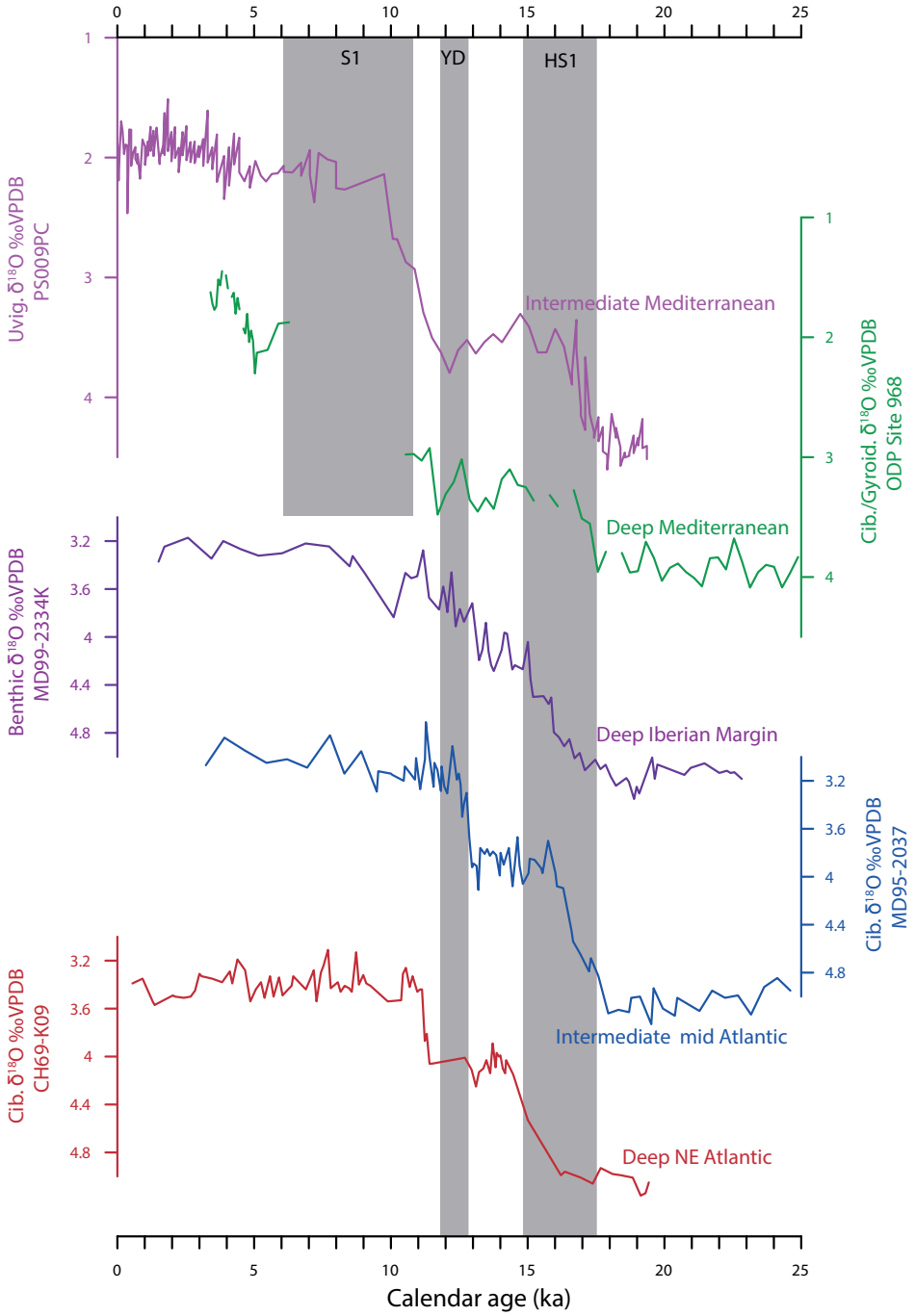

Figure 4.4: Comparison of several North Atlantic records presented in Waelbroeck et al. (2011) to the Mediterranean records. MD99-2334K (Deep Iberian Margin), MD95-2037 (intermediate mid-Atlantic), and CH69-K09 (Deep North Atlantic) are plotted on their respective 14C based age models (Waelbroeck et al., 2011). Shaded bars indicate known pervasive climate events as in figure 4.2.

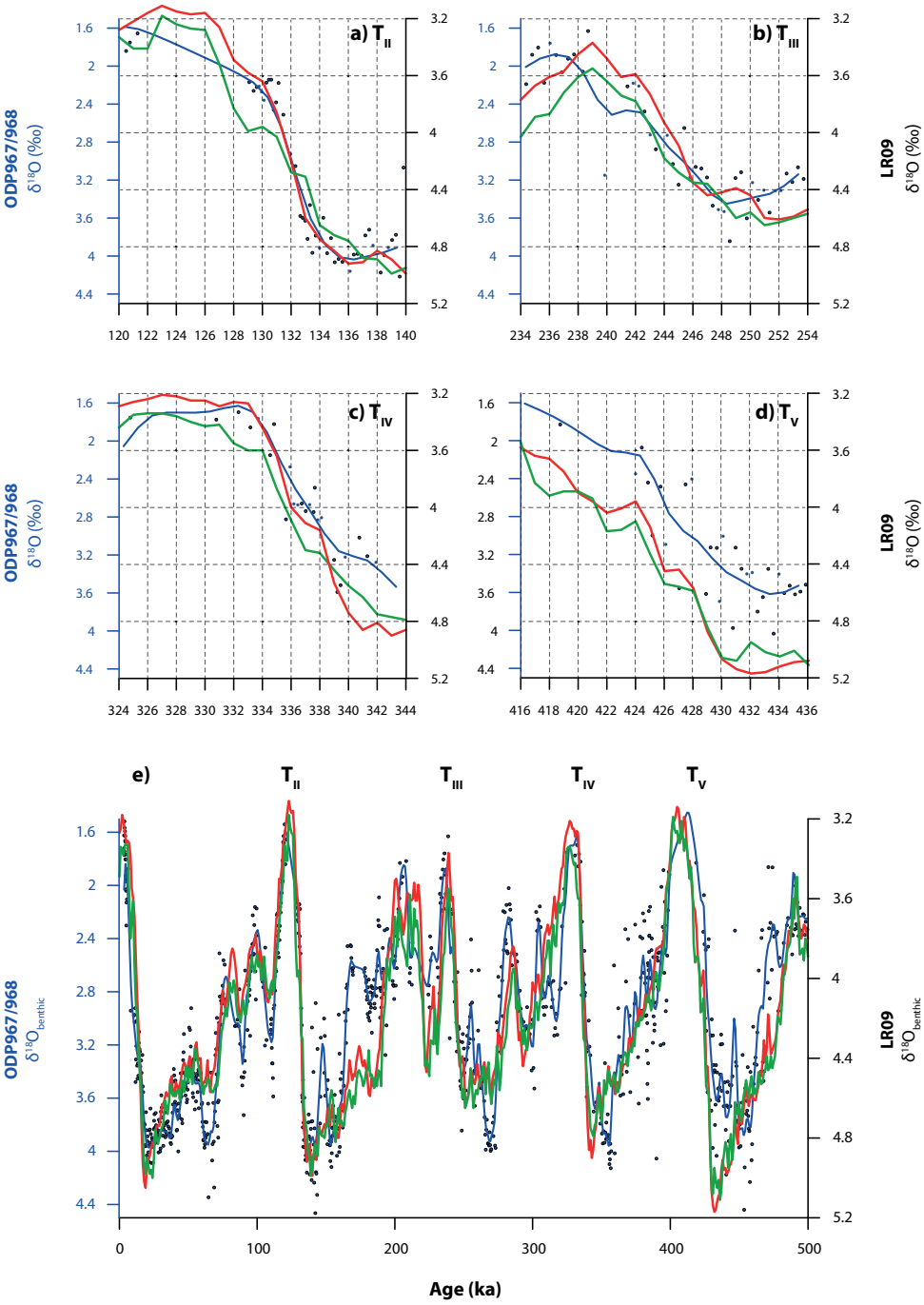

Figure 4.5: a)-d) Terminations T_{II} to T_V in the deep Mediterranean (blue) compared to the $LR09_{Atl}$ (red) and $LR09_{Pac}$ (green) stacks (Lisiecki and Raymo, 2009). Blue dots indicate individual $\delta^{18}O$ measurements in the Mediterranean record. Hiatuses occur in some intervals, especially interglacials, due to sapropels (not indicated). e) overview of the last 500 ka

(chapter 3). This is still more than the uncertainty interval of our chronology – though not outside the uncertainty estimate of Lisiecki and Raymo (2009).

4.4 Discussion

Overall, the Mediterranean benthic $\delta^{18}O$ records and those of the open ocean are very similar in behavior and timing. In particular, the timing of T_I, T_{II} and T_{III} with the Atlantic and Pacific stacks of Lisiecki and Raymo (2009) and the Mediterranean results are closely intertwined. The first time there is any discrepancy between the records is in T_{IV}, and more so during T_V. This may have to do with the fact that the shape of the Mediterranean isotope record is different from the open oceans during MIS 8, 10 and 12, which points to a slightly different response of the eastern Mediterranean to full glacial conditions. The estimated timing of the major terminations is nevertheless not far off: T_{IV} still agrees well within the 2σ error margin of 1.6 kyr (chapter 3), and the discrepancy of T_V is modest: 1.9 kyr.

The difference for these later terminations could be due to flaws in either record. For the Mediterranean record, the age estimates for T_{IV} and T_V are based on tuning of the elemental Ti/Al ratio to insolation, rather than correlation of the color reflectance record to the Sanbao-Hulu $\delta^{18}O_{speleothem}$ as was applied for the upper 300 ka of the record (Ziegler et al., 2010; chapters 2 and 3). The fixed 2.7 kyr lag used in our tuning for the older (>340 ka) record introduces some uncertainty in the age model (chapter 3). On the other hand, there is also a minimal 3-kyr uncertainty involved in the age estimates of Lisiecki and Raymo (2004, 2009).

The structure of T_I in the Mediterranean is divided in three phases. The onset of a deglaciation signal in the $\delta^{18}O$ occurs at ~17.5 ka in both the deep and intermediate Mediterranean simultaneously. This onset, at the start of HS1, is synchronous with the findings of Stern and Lisiecki (2014) for the deep and intermediate North Atlantic. The shift to lighter $\delta^{18}O$ values in the Mediterranean cannot be caused by brine as suggested by Waelbroeck et al. (2011) for the North Atlantic. It could be that the Atlantic surface waters flowing into the Mediterranean were highly depleted in $\delta^{18}O$. Evidence suggests that icebergs reached the Iberian Margin during HS1 (Bard et al., 2000), which would provide fresh, light $\delta^{18}O$ water to the Mediterranean surface waters. Alternatively, the shift in $\delta^{18}O$ could be the result of simultaneous warming of the LIW and EMDW reservoirs. Near the end of HS1 the Mediterranean $\delta^{18}O$ records level off, and remain constant until the start of the YD despite continuous glacial melt and associated sea level rise (Lambeck and Chappell, 2001; Carlson and Clark, 2012). Such plateauing is also seen in several open ocean cores (figure 4.4), but is not found in the Intermediate and Deep North Atlantic stacks of Stern and Lisiecki (2014), likely because it is averaged out. The deglaciation trend in $\delta^{18}O$ resumes at the end of the YD, which is later than in the open ocean where it resumes at the start of the YD instead (figure 4.3). During the YD there is hysteresis between the LIW and the EMDW. The LIW record indicates a cooling of LIW, consistent with findings of Bard et al. (2000) and Cacho et al. (1999) that Mediterranean surface waters cooled significantly during the YD. The EMDW record however shifts to lighter $\delta^{18}O$ values. This could be the result of low $\delta^{18}O$ water input in the surface of the Adriatic Sea that is mixed in with the LIW to form EMDW. The LIW record attains full Holocene values at ~10 kyr, which agrees with the Intermediate and Deep North Atlantic stacks to within 1 kyr.

4.5 Conclusions

We describe the development of the intermediate and deep eastern Mediterranean over the course of the last glacial termination, and compare them to open ocean studies. Both records show a strong initial warming at the onset of HS 1, with the intermediate Mediterranean warming relatively more than the deep water. This timing, at ~17.5 ka, is identical to open ocean estimates. There is a stop and even slight reversing trend in the Mediterranean $\delta^{18}O$ records from ~17.0 ka until the end of the Younger Dryas, despite ongoing glacial melt. During the Younger Dryas, there is a hysteresis between the intermediate and deep records, possibly partly due to low $\delta^{18}O$ water input from the Alps into the Adriatic basin where EMDW is formed. At the end of the Younger Dryas, the warming trend is resumed and Holocene values are reached at ~10 ka. Overall, the pattern of a three-phase deglaciation is seen in many open ocean records as well, although it less evident when multiple records are stacked.

Based on the evidence of especially T_I we conclude that there is no structural difference between the Mediterranean $\delta^{18}O$ response during deglaciation and the open ocean. This allows for a meaningful stratigraphic correlation between Mediterranean records and the open ocean, within uncertainty. With the addition of more and better dated records, the exact nature of deglaciation in the different ocean basins will be resolved in the future.

How inappropriate to call this planet Earth when it is quite clearly Ocean.

Arthur C. Clarke

Chapter 5

A new MedStack – 1.2 million year history of Eastern Mediterranean Hydroclimate

T.Y.M. Konijnendijk[1,], M. Ziegler[1], R. de Bruijn, S. Veldhuijzen, C. Schrader, M. ten Have, J. van Dijk, S.P. Akse, R. van der Ploeg, L. Roskes, A. Vrijhoef, F. van Dorp, M. van der Schee, P. Mesman, A. Dols, L.J. Lourens[1]*

[1]: Utrecht University, Faculty of Geosciences, Institute for Earth Sciences

The Mediterranean is a semi-enclosed basin, almost entirely separated from the open ocean and only connected by the Strait of Gibraltar. Extreme shifts in Mediterranean circulation occur regularly as a result of environmental changes. A well-known example at multi-millennia timescales is the episodic stratification of the eastern Mediterranean resulting in sapropel formation.

Here we present new data from eastern Mediterranean ODP Site 967 and 968. These 1200 kyr long high resolution records of bulk sediment geochemistry and planktic foraminiferal oxygen isotopes document changes in the past Mediterranean hydroclimate. The benthic foraminiferal records from the same sites register the eastern Mediterranean deep water signal, which resembles the open ocean isotope variability. The planktic foraminiferal record in turn exhibits strong regional influences of temperature and salinity. The planktic record is included in a new MedStack, which we present here with an improved age model and higher resolution, thus better representing Mediterranean planktic isotope stratigraphy.

Using astronomical tuning of the geochemical signature in our eastern Mediterranean sites, we constructed a detailed chronology for all the events in our various records. We find that the lag between sapropel formation and insolation forcing varies, and is generally shorter in the Middle Pleistocene than it is in the Late Pleistocene.

5.1 Introduction

5.1.1 Eastern Mediterranean circulation changes on orbital time scales

The Mediterranean Sea is a semi-enclosed basin that interacts with global ocean dynamics (i.e. the Atlantic) through the Strait of Gibraltar. It is divided in an eastern and western basin (figure 1.3), which are separated by the Strait of Sicily (Robinson et al., 1992). At orbital time scales, variations in sea level have the potential to influence the exchange rates of water between the Atlantic and Mediterranean by restricting the Gibraltar Strait exchange flow between the Atlantic and Mediterranean basins (Rohling et al., 2014). Nonetheless, benthic oxygen isotope data over the Pleistocene (chapter 3) suggest that the deep Mediterranean isotopic signature reflects the global benthic signal (Lisiecki and Raymo, 2005), with the understanding that the Mediterranean record exhibits on average heavier values and a slightly higher amplitude variability (Ziegler et al., 2010).

On the other hand, the Mediterranean has numerous regional circulation processes and intense dynamic variability. A well-known example is the formation of sapropels in the eastern Mediterranean in response to orbital insolation changes (Rossignol-Strick, 1985; Rohling et al., 1994, 2015). According to theory, at peak summer insolation the monsoon over the North African continent is enhanced. The resulting increased North African river runoff creates a low salinity lid over the eastern Mediterranean, stopping the salinity driven formation of Levantine Intermediate Water (LIW), and stratifying the water column (Rossignol-Strick, 1985). This results in the deposition of dark, organic-rich layers throughout the basin (de Lange et al., 2008).

5.1.2 Present-day Mediterranean circulation

Both sub-basins (figure 1.3) have a variety of regional processes occurring within their respective boundaries, such as deep water formation. Relatively less-saline water from the Atlantic flows eastwards from Gibraltar, being partially diverted into western Mediterranean circulation, and enters the eastern Mediterranean through the Sicilian Strait (Wüst 1961; Emeis et al., 1996; figure 1.3) the only seaway connecting the eastern and western basins. Evaporation over the length of this course causes the water to become more saline and therefore denser (Robinson et al., 1992). In the easternmost part of the Mediterranean, LIW is formed when this dense water sinks during winter, forming a water mass between 200 to 600 m depth (Wüst, 1961). Eastern Mediterranean Deep Water (EMDW) is mainly formed in the Adriatic Sea and partially in the Aegean Sea, where the saline water cools substantially in cold winters. It mixes in with the LIW in the deep Tyrrhenian Sea (Astraldi et al., 2002), which is exported to the Sicilian Strait into the Western Mediterranean basin and out the Gibraltar Strait into the Atlantic, partially recirculating in both Mediterranean sub-basins. The export of nutrient rich deep waters makes the Mediterranean, and the eastern basin especially, a nutrient desert (Emeis et al, 1996).

5.1.3 Sapropel chronology

Episodically deposited sapropel layers have been used for stratigraphic correlation and age model construction (e.g. Lourens et al., 1996; Hilgen, 1991; Emeis et al., 2000; Lourens, 2004). Typically, sapropel midpoints are tuned to June 21st 65°N insolation maxima with a lag of 3000 years (3 kyr). The 3 kyr time lag is based on sapropel S1 in the Holocene, which was dated by ^{14}C AMS dating (Mercone et al., 2000). The midpoint of S1 falls at 8.5 ka – 3 kyr behind the corresponding insolation maximum at 11.5 ka. This lag is assumed to be inherent to the processes behind sapropel formation (Lourens et al., 1996). Using a constant lag of 3 kyr to the target curve of June 21st 65°N insolation, sapropel tuning has formed the basis of the astronomically tuned Neogene time scale (Gradstein et al., 2004).

While the tuning of sapropels is considered to be fairly reliable, the assumption of a constant 3 kyr lag is not beyond questioning, especially since model studies suggest there ought not be a lag in the response of North African climate to insolation (Tuenter et al., 2005). Apart from the evident lag in S1, Lourens et al. (1996) found that the alternating thick-thin patterns in Plio-/Pleistocene sapropel groups of the Singa/Vrica sections match the interference between obliquity and precession in the insolation forcing when a 3 kyr lag was incorporated. Ziegler et al. (2010) suggested that an average lag of sapropel midpoints of around 3 kyrs during the Late Pleistocene results from the influence of North Atlantic cold events that delay the onset of strong monsoon intensity during precession minima. They predicted that the lag is most likely smaller during the Early Pleistocene and Pliocene, due to the absence of large North Atlantic cold events during these time periods.

A variable time lag of sapropel midpoints over the past 1 million years was established in chapter 2. There we used the ratio of titanium to aluminum in the sediment of ODP sites 967 and 968 in the eastern Mediterranean, a proxy for North African aridity, and based our age model on tuning this proxy to June 21st 65°N insolation (Laskar et al., 1990), arrived at new age estimates for a number of sapropels over the last 1 Myr.

5.1.4 Multiproxy reconstruction of Pleistocene Mediterranean circulation changes

A better understanding of the oceanic processes during sapropel formation requires a multi-proxy approach. In this study we extend the Ti/Al based astronomical age model of chapter 2 to 1.4 Ma, covering the period of the Mid-Pleistocene Transition (Clark et al., 2006). We provide renewed age estimates for the sapropels found in ODP site 967 in the extended part of the record. In addition, we add geochemical data – i.e. the Barium-Aluminum ratio as a proxy for deposition of (oxidized) organic matter – and a full, high-resolution planktic foraminiferal oxygen isotope record from the same sites.

We have integrated the new planktic data with the previously published MedStack (Lourens, 2004; Wang et al., 2010), a compilation of eastern Mediterranean planktic isotope records. This incorporates data from cores KC01b (Rossignol-Strick et al., 1998), and MD84641 (Fontugne and Calvert, 1992), while the older part (>1.2 Ma) is covered by the Singa/Vrica sections (Lourens et al., 1996). The new MedStack has much higher resolution and a revised structure with weighted contributions from the individual sites based on sampling resolution. The age model for the last 1200 kyr is also updated, based on the Ti/Al proxy evidence.

Using the combination of available proxies we tentatively disentangle the different processes at work in the eastern Mediterranean, the contrast between deep water and surface ocean conditions, and hydrological conditions of the region.

5.2 Materials and Methods

5.2.1 ODP Sites 967 and 968

Our study uses data from the adjacent ODP Sites 967 and 968 in the eastern Mediterranean (figure 1.6). ODP Site 967 (34°04'N, 32°43'E) was drilled south of Cyprus, near the Eratosthenes seamount at a water depth of 2,554 m. ODP Site 968 (34°20'N, 32°45'E) was drilled on the Eratosthenes seamount at a water depth of 1,961 m (Emeis et al., 1996). The data of the two adjacent sites are combined into a single splice using color reflectance data. The recovery at Site 968 is incomplete, compelling us to use ODP Site 967 in order to create a continuous record. The construction of the combined splice is described in detail in chapter 2. The combined splice of ODP 967 and 968 was sampled at 2cm intervals. Samples were split into a 3-5 g part that was used for XRF analysis and the remaining12-20 g which was washed and sieved for the extraction of foraminifers.

5.2.2 Stable isotopes

For the planktic oxygen isotope record 30 specimens of the surface-dwelling species *G. ruber* were handpicked from the size fraction>212μm. Specimens were placed in ethanol and subjected to several seconds in an ultrasonic bath to clean the samples. The ethanol was extracted, after which samples were crushed, homogenized, and dried. 20-50 μg of the samples was used for mass spectrometry.

The stable isotope data were produced on a Thermo-Fisher MAT253 mass spectrometer, coupled with a Kiel III automated carbonate reaction device. A standard run consisted of 35 samples interspersed with three aliquots of an in-house standard (NAXOS) as well as eight aliquots of an international carbonate standard (NBS-19). Long-term analytical precision is better than 0.1‰ and 0.03‰ for $\delta^{13}C$ and $\delta^{18}O$, respectively.

5.2.3 XRF measurements

For the XRF-procedure, 3-5 gram of the samples was freeze-dried, then ground and homogenized. The samples were placed in a furnace and heated stepwise to 100°C, 450°C, 550°C, 800°C and 1000°C. At each interval the relative weight loss was measured to obtain residual water content, organic matter content and carbonate minerals, respectively. The residue of this treatment was then molten into glass beads for XRF scanning. 600 mg of the sample powder was mixed with 6000 mg lithium tetraborate (Li2B4O7, Spektromelt), and fused to glass beads. The elemental composition of the beads was measured using a Philips PW 2400 X-ray spectrometer. Analytical precision was determined by parallel analysis of one international standard (ISE 921) and one in-house standard, and found to be within 2% for Al and Ti.

5.2.4 Age model

The ratio of titanium to aluminum (Ti/Al) in the sediment is a proxy for aridity in the Sahara, and as such inversely proportional to activity of the North African monsoon (Lourens et al., 2001). Between 65 % and 95% of the titanium in the sediment comes from windblown dust (Wehausen and Brumsack, 2000), whereas aluminum originates from clay minerals in the Nile outflow. The discharge of this river and associated sediment load reflects precipitation rates on the North African continent. Changes in Ti/Al therefore mirror humidity changes in Central to North Africa (Lourens et al., 2001). The North African monsoon is known to be driven by changes in the earth's orbit, mainly precession (Rossignol-Strick, 1985). Thus, the Ti/Al ratio in the sediments at ODP sites 967 and 968 exhibits a strong signal that quite linearly reflects insolation forcing chapter 2.

In line with chapter 2 we constructed our age model by tuning the Ti/Al ratio to June 21st 65°N insolation. The phase lag of the Ti/Al proxy with regard to insolation was established in chapter 2 to be 2.7 kyr. This is the average lag of the speleothem oxygen isotope ($\delta^{18}O_{speleothem}$) records of the Sanbao/Hulu caves (Wang et al., 2008; Cheng et al., 2009), which are highly correlated to ODP site 967 and 968 color reflectance as well as Ti/Al ratio (Ziegler et al., 2010). The radiometric (U/Th) dating of the Chinese monsoon record therefore provides a robust estimate of the leads and lags in the climate system to astronomical forcing. The uncertainty involved with the tuning process was estimated to be ±1.6 kyr (2σ interval) in chapter 3.

We extrapolated the 2.7 kyr lag for the rest of our record, up to 1.4 Ma. The tuning process was straightforward, with the pronounced precession signal and interference patterns in the forcing clearly reflected in the Ti/Al record (figure 5.1). We identified and removed three turbidites from the record around 1.2 Ma based on the distinctive geochemical signature of the deposits (chapter 2). The resulting age estimates for sapropel deposition at ODP site 967 can be found in the §5.3.1.

5.2.5 Construction of the new MedStack

To compile the available planktic isotope records into one we made use of the stratigraphic alignment performed previously by Lourens (2004). As a starting point for a new age model for the individual contributing records we used the updated age estimates of sapropels as initial tie points. These had been correlated and been assigned a new age estimate based on the Ti/Al

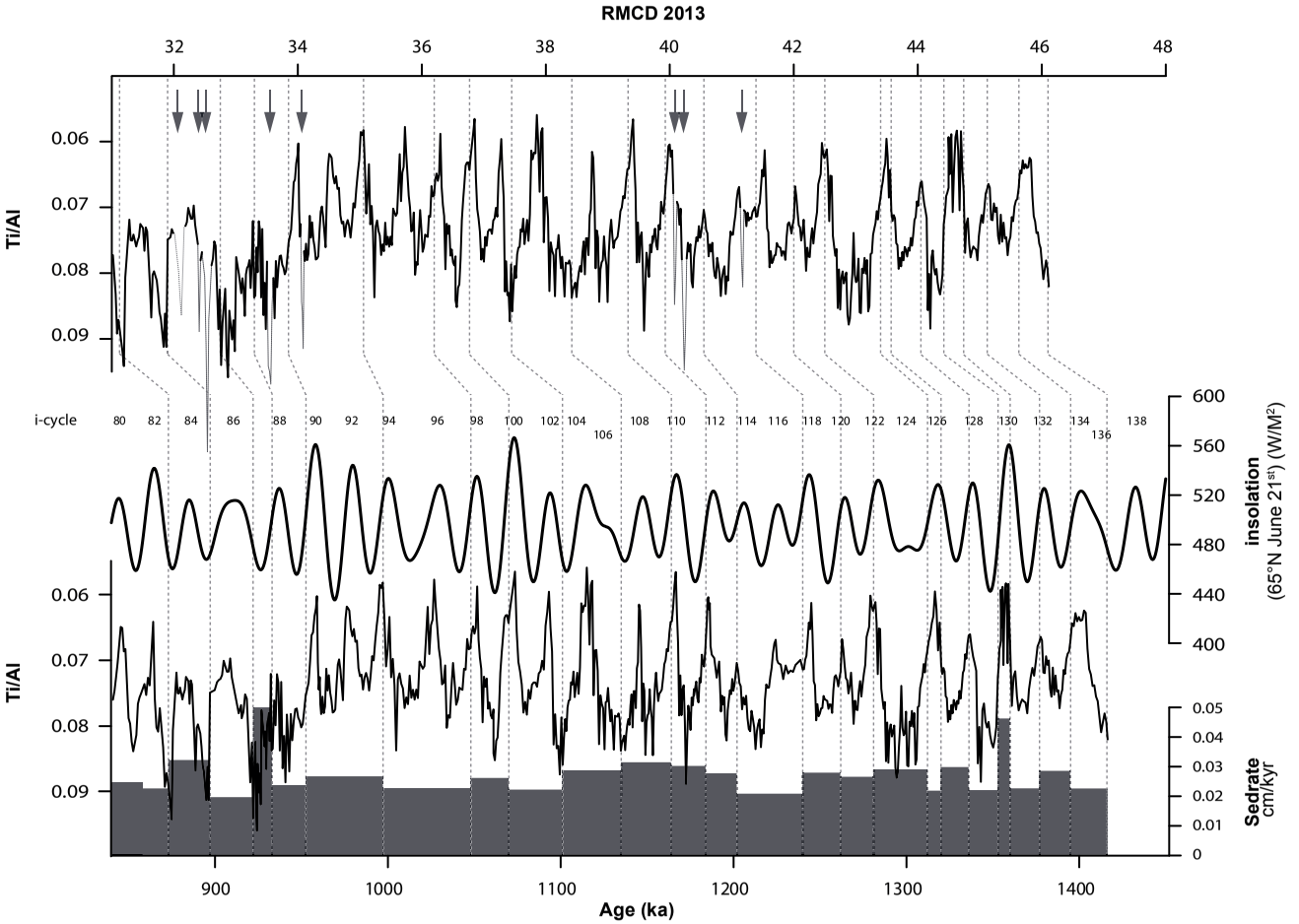

Figure 5.1: the Ti/Al record matched to 65°N June 21st insolation. Dashed lines connect the tie points in the records from depth to time domain. In the top graph, grey arrows indicate the position of turbidites; turbiditic intervals are represented by a grey arrow. Note that in the bottom record, these turbidites are filtered out of the data completely. The vertical grey bars indicate sedimentation rates as determined by the tuning.

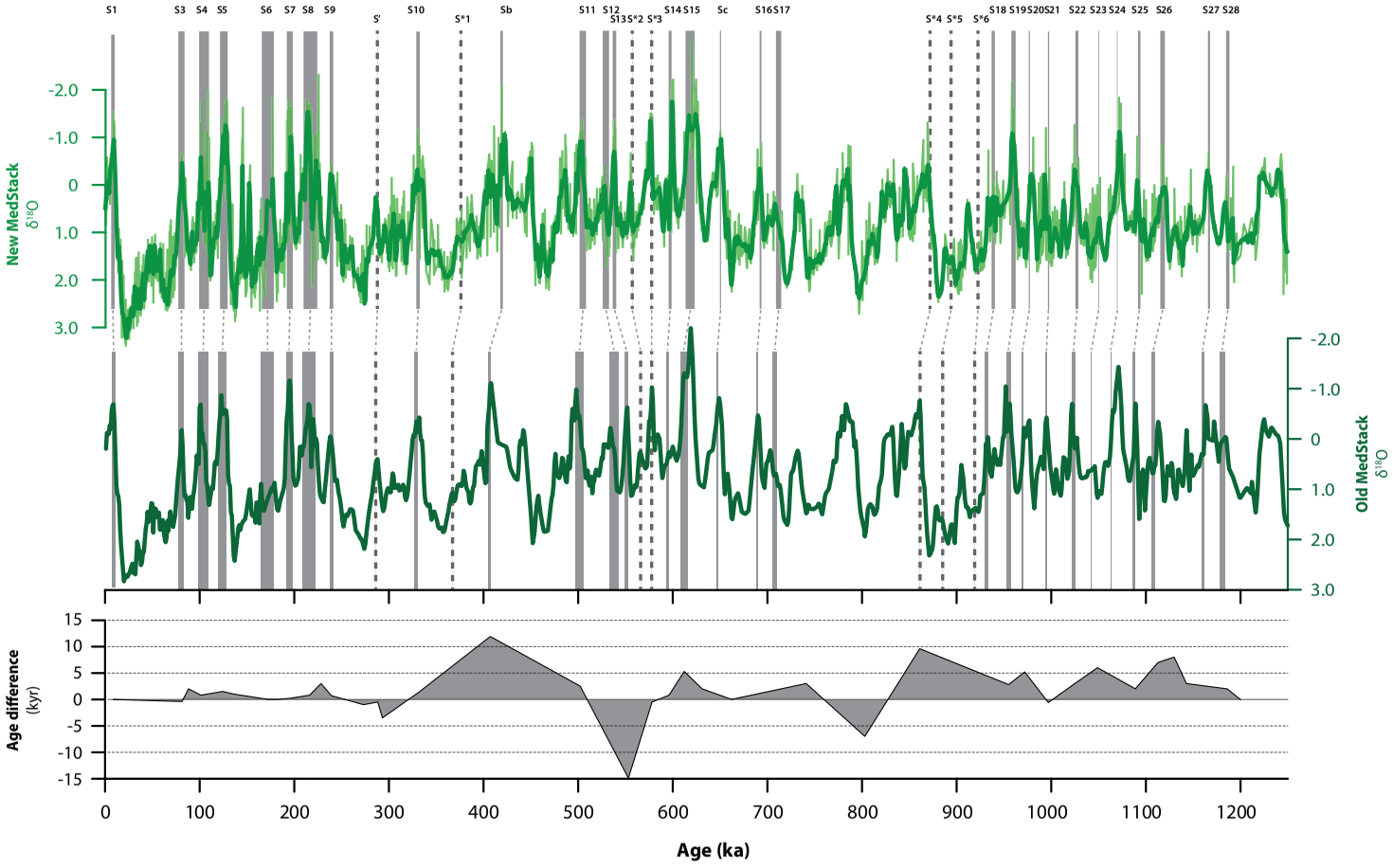

Figure 5.1: the new and old MedStack records. In light green (top) is the total data variability of the records used in the creation of the new MedStack. The thick line is the 1-kyr interpolated value. Grey vertical bars represent intervals of sapropel deposition, with dashed lines connecting them to the estimated ages of Lourens (2004) in the middle graph (dark green). The differences between the two records' age estimates are displayed at the bottom.

chronology (chapter 2). This approach resulted in a mostly satisfying fit between the ODP Site 968/967 planktic record and the existing MedStack, with the exception of sapropel s15 (~617 ka), s20 (~977 ka) and, s22 (~1026 ka). These sapropels seem to be incompletely preserved in the KC01b record, causing a discrepancy in the midpoint position. These intervals were adjusted, after which the old MedStack record was fine-tuned manually to the ODP Site 968/967 record, resulting in a successful reconfiguration of each planktic isotope record onto the Ti/Al based chronology.

The freshly aligned records were stacked, and smoothed by applying a moving 5-pt. average window. Then, the record was resampled at 1 kyr resolution (figure 5.2). This is a different procedure from the previously published MedStack (Lourens, 2004), where the individual records were first resampled to 1 kyr resolution before adding them to the stack. The new approach results in a weighted contribution of each record based on sampling resolution. The new MedStack shows more variability than the old curve (figure 5.2), and with higher confidence through its much higher resolution. Also, some intervals with missing data have been filled with data of ODP sites 967 and 968.

The MedStack chronology has undergone only minor changes due to fine tuning between 0-300 ka. However, around 400 ka there is a major discrepancy (figure 5.2). This is due to the misattribution of sapropel S11 in KC01B to the insolation maximum at 407 ka, instead of the one at 419 ka (Lourens, 2004; chapter 2). The Ti/Al record leaves no room for such an interpretation (chapter 2) which would also offset termination V at the onset of MIS 11 in the benthic record considerably with regard to the LR04 benthic stack (chapter 3.; this study). On the other hand, Sa in KC01B – which is correlated to S13 in ODP 968 – is considerably younger, not being related to i-cycle 52 (as proposed by Lourens, 2004) but to a rather broad insolation maximum around 530 ka (chapter 2). In the interval 700-900 ka, insolation forcing is particularly weak due to a node in the 405-kyr eccentricity cycle. The problematic tuning in this section has led to the rather large adjustments in chronology here (figure 5.2). The remaining adjustments in the Middle Pleistocene age model of MedStack are modest, though isotopic features are consistently attributed older ages.

5.2.6 Spectral analysis protocol

All the records discussed in this paper were analyzed using Analyseries (Paillard et al., 1996). Blackman-Tukey spectral analyses were performed using 3 different levels of confidence: 80%, 90% and 95%. Spectral peaks were filtered from each record using a wide range (frequency ± 20%) spectral band-pass filter, unless otherwise specified. Cross-spectral analyses, to reveal spectral correlation and phase between the records, were also performed using Analyseries, at the same 3 levels of confidence. A cross-correlation value over 90% is considered significant, a value over 95% is considered high.

5.3 Results

5.3.1 Middle Pleistocene (1 - 1.4 Ma) sapropel deposits at ODP site 967

The Ti/Al based chronology renders detailed age estimates for the boundaries and midpoints of sapropel deposits at ODP site 967. We retain the boundaries as defined by Emeis et al. (2000), who first published a sapropel chronology for this site. The table in appendix V gives an overview of the stratigraphic position and age estimates as published by Emeis et al. (2000), as well as our own age estimates. On average, our estimates are ~2.8 kyr older than those of Emeis et al. (2000). This implies a significant reduction of the lag between sapropel formation and insolation forcing, i.e. an almost instantaneous response. The average may be influenced by the relatively large

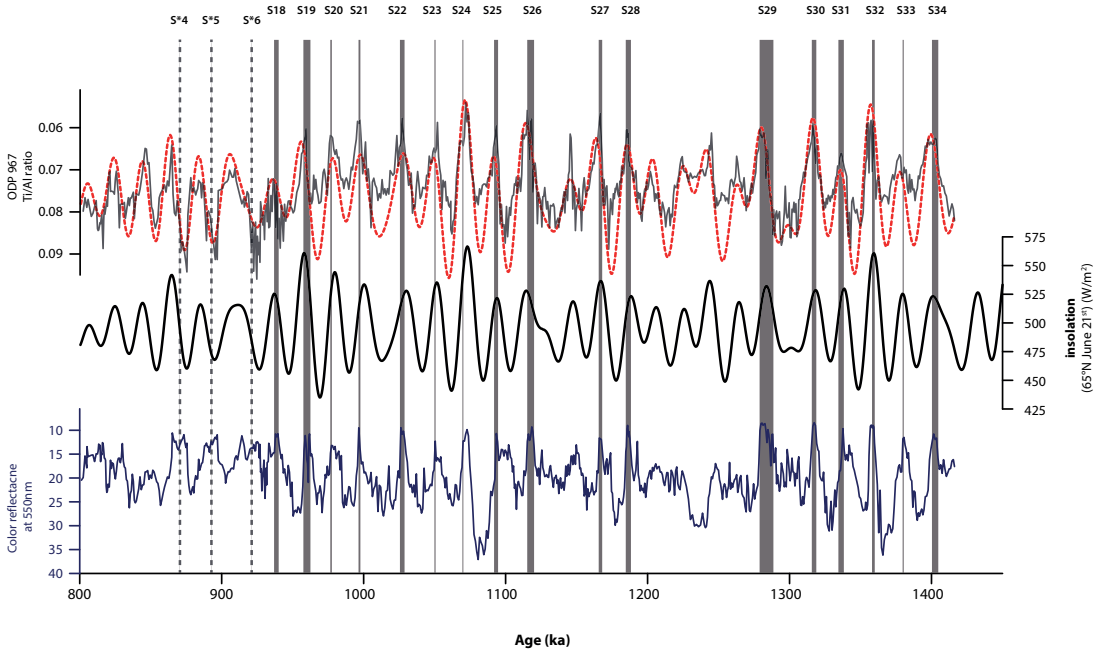

Figure 5.3: The ODP 967 Ti/Al record (top) and color reflectance record at 550 nm (bottom), in relation to 65°N June 21st insolation (middle). The dashed red line in the top graph is a combination of the filtered 41 and 23 kyr signals in the Ti/Al record after tuning, demonstrating the highly linear response of this proxy to insolation. Sapropels, indicated by vertical grey bars, coincide with excursions in color reflectance, but often occur before the monsoon maxima as indicated by the Ti/Al proxy.

difference in our estimates of S26 and S33, which were estimated to be 7.4 kyr and 4.0 kyr older, respectively. The interference pattern between two short precession cycles (i-cycles 104 and 106) and obliquity creates a broad insolation maximum around 1120 ka, and S26 seems to respond to this maximum (figure 5.3). Emeis et al. (2000), on the other hand, had related it to the younger precession cycle at 1114 ka. In the case of S33, this seems to be a rather skewed response, with the sapropel in the deeper part of the cycle (figure 5.3), while the color reflectance at 550 nm exhibits a prolonged response. This is not considered part of the sapropel however, and therefore the midpoint falls quite early. This may partially explain the rather large difference in age estimates. Overall, our results do indicate a significantly faster response of sapropel formation to insolation in the Middle Pleistocene.

5.3.2 Characteristics of the new MedStack

The combined planktic isotope data of ODP Sites 967, 968 and of KC01b and md84641 make for a very high resolution record representative of eastern Mediterranean sea surface conditions. Spectral analysis (figure 5.4) reveals strong power in the 100, 41, and 23 kyr bands, with a smaller peak around 19 kyr. The cross-correlation with June 21st 65°N insolation (Laskar et al., 1993) indicates strong coherency at obliquity and both precession frequencies. The 41 kyr signal lags obliquity forcing by ~3.5 kyr, whereas phase lags are ~2.0 and ~1.4 kyr for the 23 and 19 kyr periodicities respectively. The variability in the MedStack planktic oxygen isotope record generally resembles insolation forcing (figure 5.5) and the band pass filter is picking up the influence of precession and

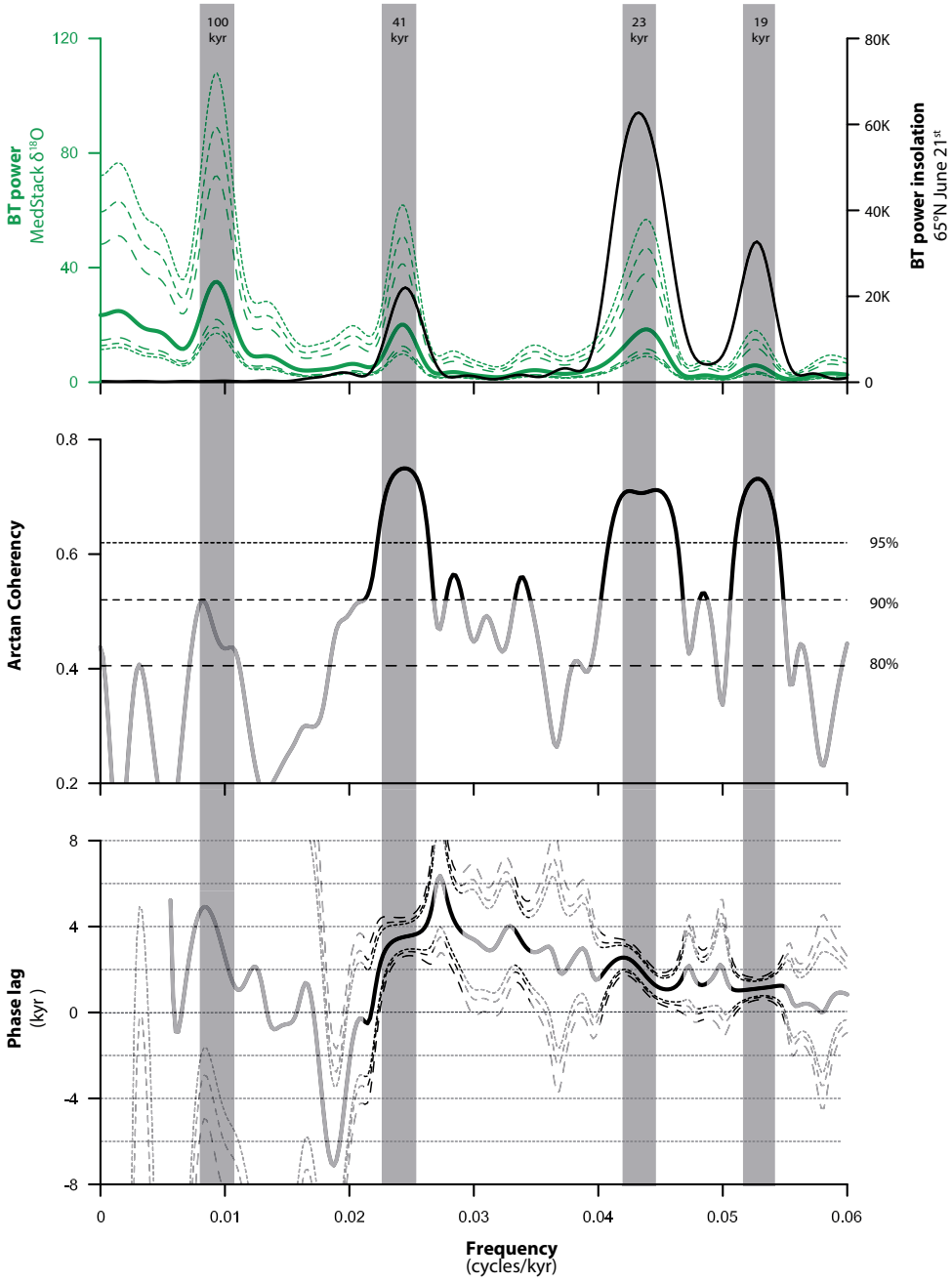

Figure 5.4: top panel: power spectrum of the new MedStack oxygen isotope record (green line), enveloped by the confidence limits at 80, 90, an 95% (dashed lines), and the power spectrum of 65°N June 21st insolation in black. Our record shows a dominant spectral peak at 100 kyr, with secondary power at 41 kyr, 23 kyr, and 19 kyr. middle panel: coherency between the isotope record and insolation. Horizontal dashed lines indicate confidence levels. Powerful (>95%) coherence in the obliquity and both precession bands. Bottom panel: Phase difference between the isotope record and insolation, in kyr. The high coherency translates into a narrow uncertainty envelope at the dominant spectral frequencies. Intervals where coherency is below 90% significance level are (partially) masked in the bottom two graphs.

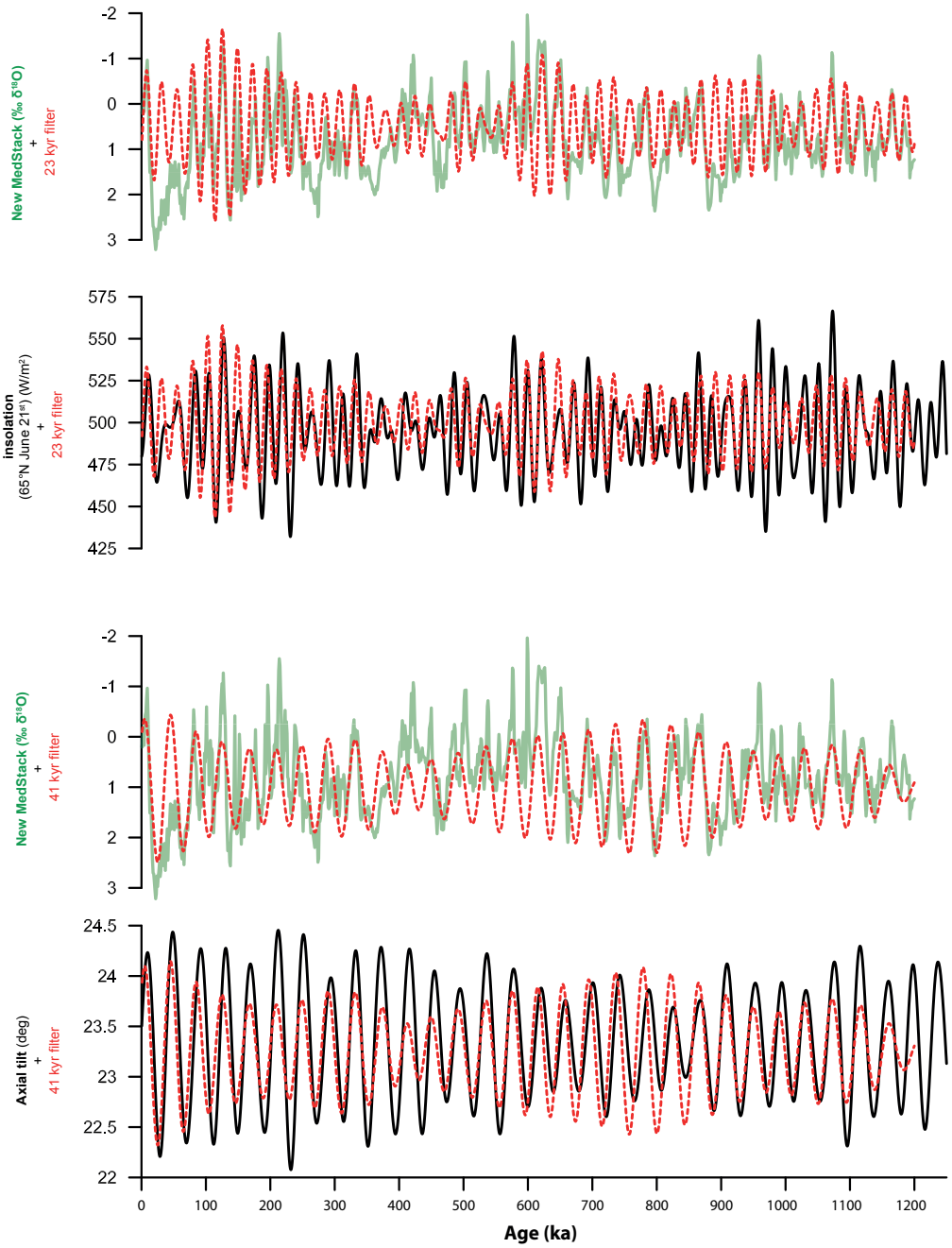

Figure 5.5: spectral fit of the dominant frequencies. Top half: a spectral filter centered on 23 kyr (frequency 0.048±0.01; dashed red line) versus the isotope record (green line), and versus insolation (black line) below. The filter picks up the precession signal perfectly everywhere but during the weakest forcing at the 400 and 800 ka eccentricity minima. Bottom half: a spectral filter centered on 41 kyr (frequency 0.0241±0.005; dashed red line) versus the isotope record (green line) and obliquity (black line).There seems to be no significant mismatch between the filter and obliquity forcing, though the phase relation is not constant.

obliquity. Even at nodes in the 405 kyr eccentricity cycle (e.g. around 400 ka and 800 ka), where the weak forcing and different frequency modulation hamper the precession filter (Huybers and Aharonson, 2011), it reflects the forcing quite well (figure 5.5).

5.3.3 Contrast of the deep/surface ocean

We are able to take a closer look at the processes specific to the Mediterranean surface waters by subtracting the benthic oxygen isotope values (chapter 3) from the MedStack record. This removes the global ice volume component and Mediterranean deep sea temperature/salinity signal (Shackleton, 1987) and isolates the surface water signal in the planktic record. First, the benthic record is low-pass filtered (>10 kyr) to remove scatter from the record. This results in a low-frequency record of benthic $\delta^{18}O$ variability with a 1 kyr resolution. The low-pas filtered record is adjusted to match the amplitude and mean of the original record (figure 5.6). We then subtract the benthic $\delta^{18}O$ value, linearly interpolated between the nearest data points, from each MedStack $\delta^{18}O$ value. The residual (figure 5.6) most likely reflects surface water temperature and/or salinity changes. The new MedStack is predominantly based on planktic $\delta^{18}O$ records from close to the Levant. This water should therefore – under normal deep water formation circumstances – have undergone little additional change in salinity before sinking to intermediate depths (Wüst et al., 1961). That means that the residual signal generally reflects a temperature contrast between surface waters (in summer, when *G. ruber* blooms) and deep sea (formed by winter cooling). Increased monsoon precipitation and north African river runoff would have a strong impact on surface salinity which would also been recorded in the surface oxygen isotope signal. The incorporation of data located further away from the Levant might add a different salinity signal to the MedStack $\delta^{18}O$. Excluding these records however was found not to significantly affect the pattern of the stack or the residual signal. Caution is required in the interpretation of the residual signal as a temperature contrast because we cannot account for e.g. the mixing of different $\delta^{18}O$ water (i.e. meltwater from Alpine glaciers) in the Adriatic during EMDW production.

Spectral analysis of the residual (planktic minus benthic) data reveals several interesting features (figure 5.7). Firstly, the dominant power controlling residual surface ocean $\delta^{18}O$ is the 23 kyr precession cycle, which was to be expected from the strong precession control on sapropels (Rohling, 1994) and hence surface water salinity influence on the MedStack $\delta^{18}O$. values With the strong 100 kyr eustatic signal removed, the remaining power in the 100 kyr band is greatly reduced. Moreover, the residual record lacks any 41 kyr signal.

Secondly, the cross spectral analysis indicates that the residual surface ocean signal has zero lag to precession in the 23 kyr band (figure 5.7). We arrive at this estimate despite the 2.7 kyr lag adopted in our tuning of the Ti/Al proxy to insolation. This suggests that, while the overall planktic signal has a ~2.0 kyr lag, the temperature/salinity component of the surface water responds almost immediately to insolation forcing.

Finally, we compared the residual record to the ratio of Barium to Aluminum in the record of ODP Sites 968/967. This is a proxy for paleoproductivity (Thomson et al., 1995) that records deposition of organic material even after it has been oxidized. Often, a Ba/Al spike is found above sapropels where the top has been oxidized (van Santvoort et al., 1996). This proxy is therefore expected to co-vary with the residual surface water signal, since sapropel deposition should coincide with strong excursions of light $\delta^{18}O$ values reflecting high temperature and/or low salinity conditions (Rossignol-Strick, 1985).

Our record exhibits sharp excursions in Ba/Al at, or just above, the stratigraphic level where sapropels are deposited (figure 5.8). The Ba/Al signal also strongly resembles the residual isotopic

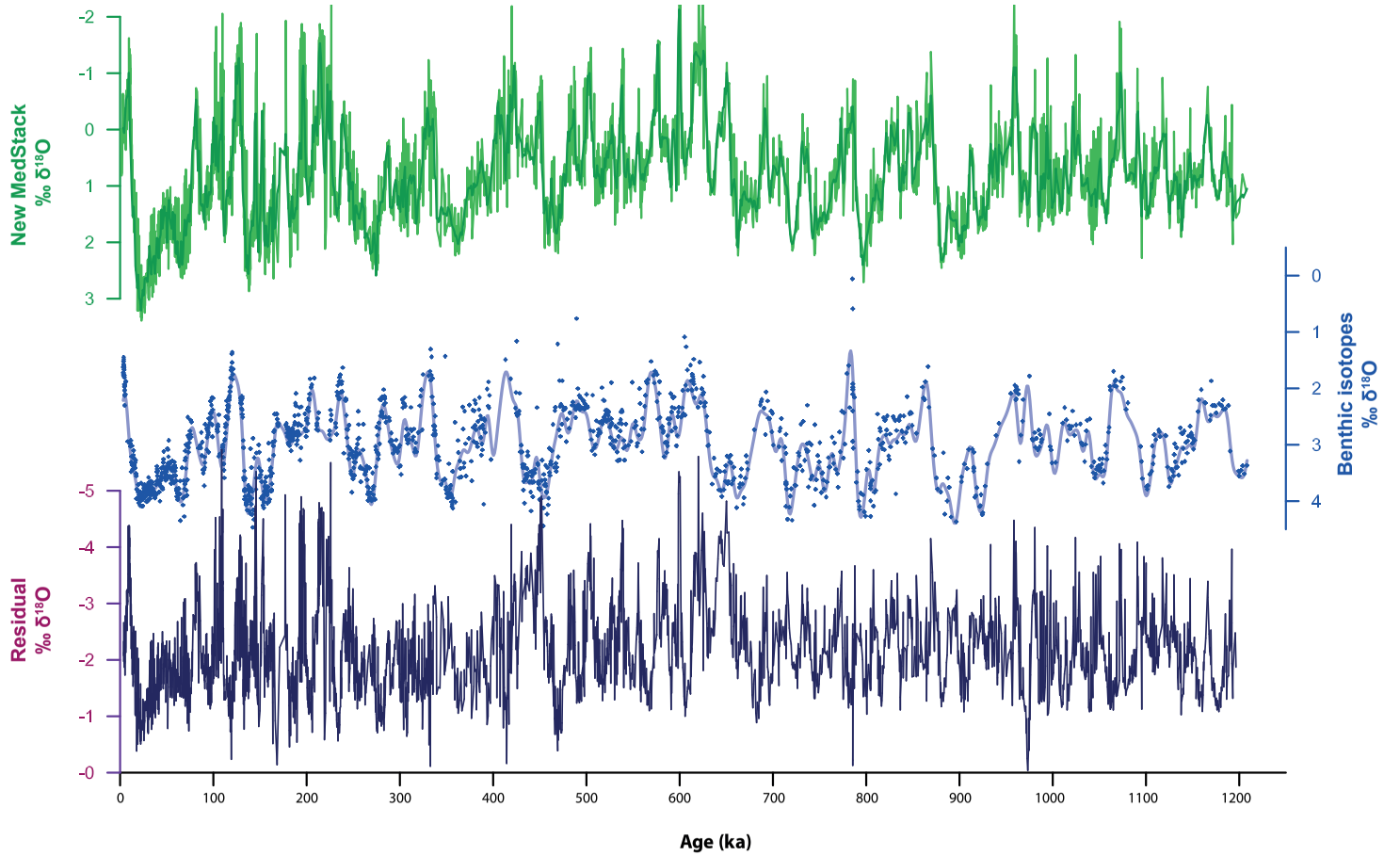

Figure 5.6: processing the residual surface ocean signal from the benthic and planktic isotope records. The top graph is the 1-kyr interpolated new MedStack record. In the middle is the ODP 967 and 968 benthic record, with a low-pass (>10 kyr) spectral filter (blue dots and line). The bottom graph shows the residual record, after deducting the benthic record from the new MedStack.

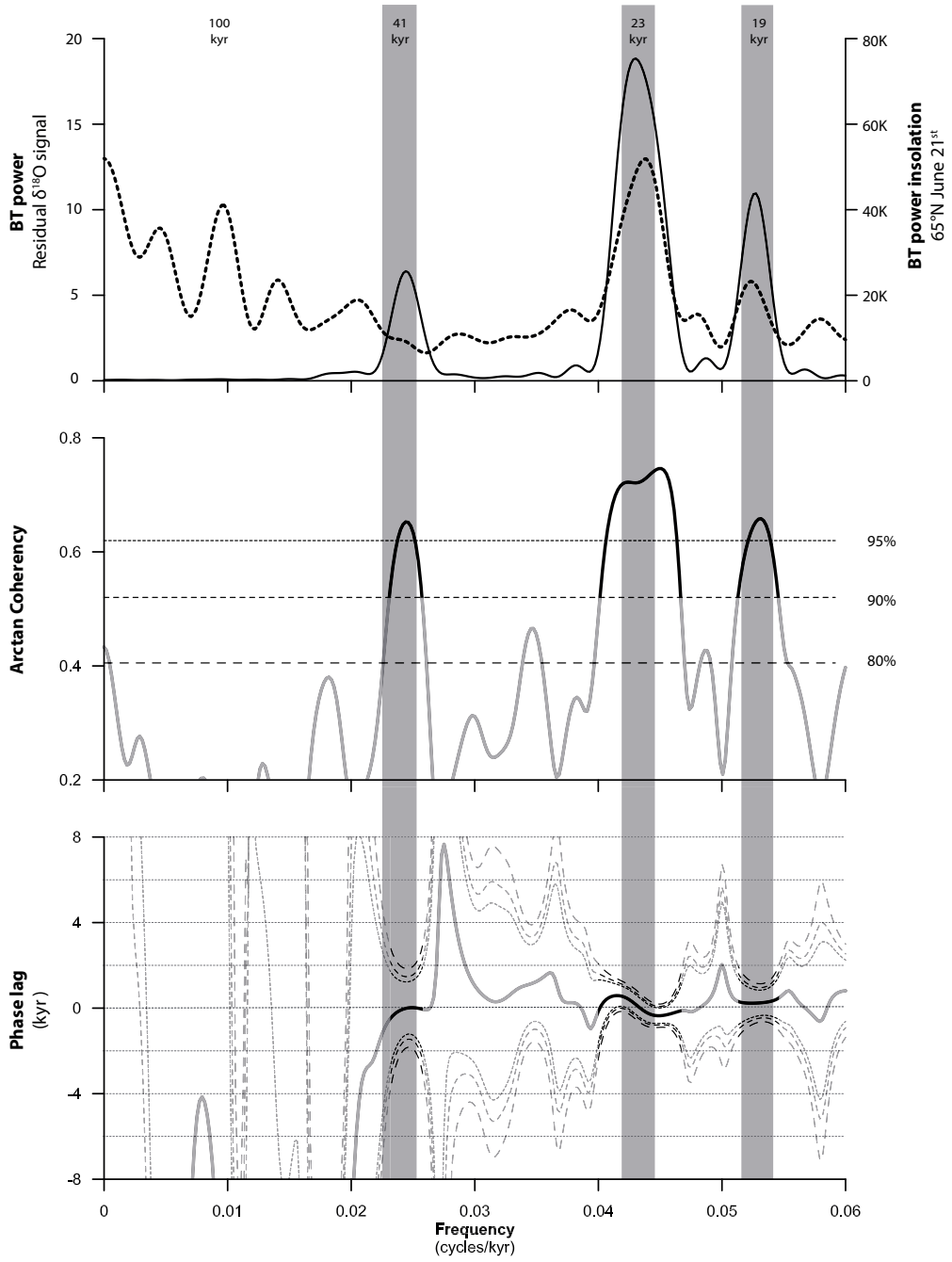

Figure 5.7: top panel: power spectrum of the residual oxygen isotope record (dashed line) and of 65°N June 21st insolation (black line). Modest power at 100 and 19 kyr, dominant power at the 23 kyr spectral band. No power is present in the 41 kyr band. Middle panel: coherency between the residual isotope record and insolation. Powerful (>95%) coherence in the obliquity (despite the low power) and both precession bands. Bottom panel: minimal phase difference between the residual isotope record and insolation, in kyr.

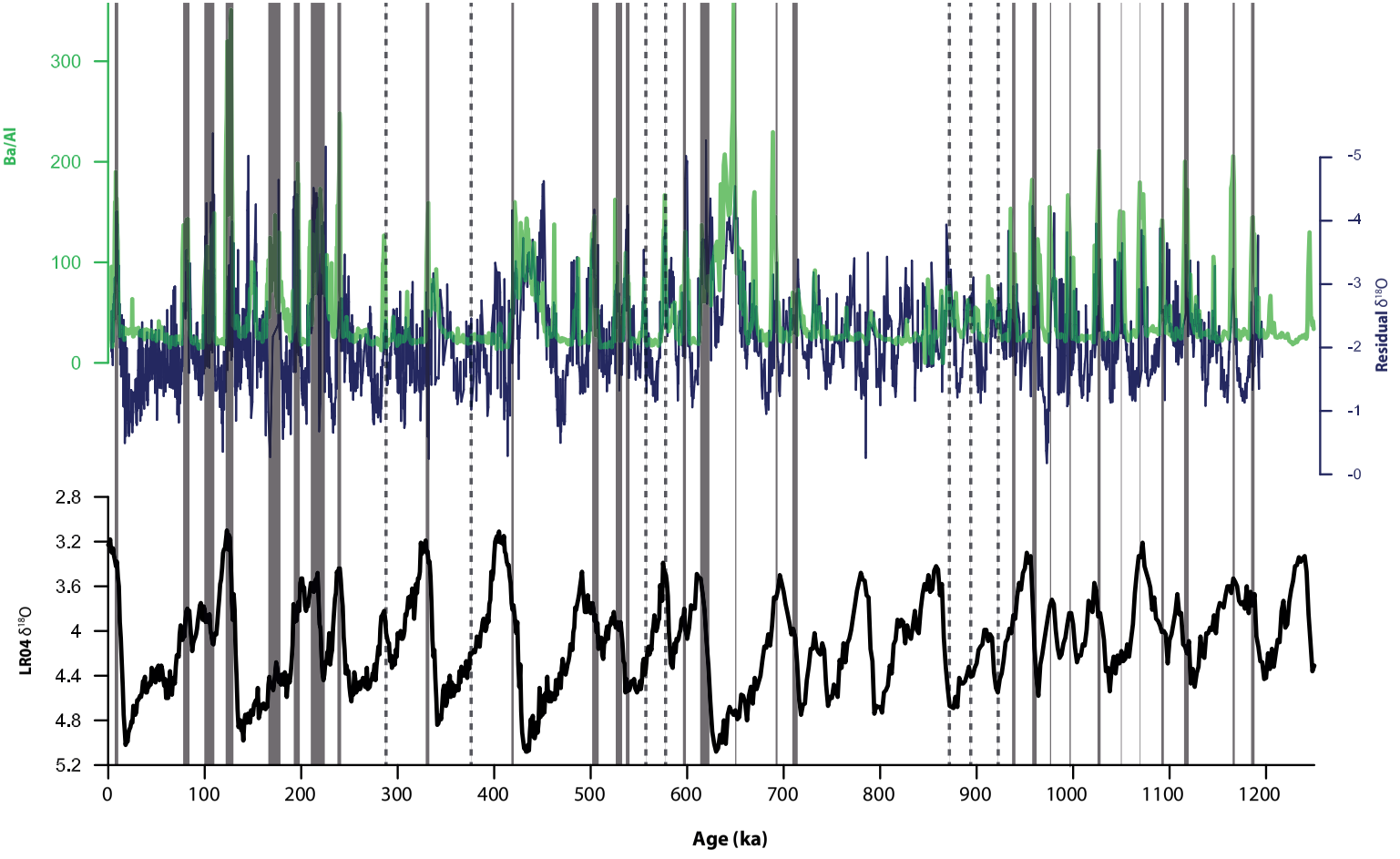

Figure 5.8: The residual isotope record (dark blue) plotted together with the ODP 967 and 968 Ba/Al record (green). Sapropels are indicated by vertical grey bars. The LR04 benthic stack (Lisiecki and Raymo, 2005) is plotted in the bottom as a reference for climate conditions and an indication of sea level changes.

signal, although the former is less linear with its clear threshold response. The residual isotopes lead the Ba/Al signal, coinciding with or slightly leading sapropel deposition. Cross spectral analysis between the Ba/Al record and the residual isotopes indicates a phase difference of ~1.8 kyr in both precession frequencies. This might in part be due to the skewed response of Ba/Al, with the highest values in the top part of the deposits (figure 5.9). This could draw power towards the upper end of the excursions. However, detailed inspection of the (less skewed) shorter lived excursions also suggests the Ba/Al to generally lag the isotopic residual curve. Ba/Al excursions are thus found at the top of freshwater episode deposits (i.e. sapropels).

For the deepest/oldest part of the record, the correlation is very clear with a set of sapropels (S18-28) deposited, each accompanied by a peak in Ba/Al and a distinctive excursion in the residual isotopic record (figure 5.8). Between 700 and 900 ka, there is a conspicuous lack of sapropel deposits due to the exceptionally low amplitude of insolation forcing during this interval. Most prominent are the extreme excursions in Ba/Al that occur after 700 ka. First in MIS 16 (~650 ka), and again in MIS 12 (~450ka), these excursions go far beyond the normal response of Ba/Al, both in amplitude and duration, to any of the variability recorded in the rest of the record (figure 5.8). This will be discussed in §5.4.3.

5.4 Discussion

5.4.1 Quicker sapropel formation in the Middle and Early Pleistocene

In the new sapropel chronology for ODP 967 based on the Ti/Al age model, there are no major discrepancies between our age estimates and those of Emeis et al (2000) due to the attribution of sapropels to different insolation cycles. The exceptions are sapropels S26 and S33, for reasons discussed in the previous section. What is striking, however, is the generally older estimates, indicating a more immediate response to insolation forcing of sapropels in the Middle- and Early Pleistocene.

We work from the assumption that the ~3 kyr lag between sapropels and insolation forcing is the overprint of North Atlantic cold events delaying the onset of the monsoon response (Ziegler et al., 2010). As yet it is unclear when large scale cold events related to Heinrich events started to occur (Hodell et al., 2008). Arguably, the smaller ice sheets of the Early- and Middle Pleistocene would not generate events of the magnitude seen during the last glacial cycles. The more immediate response of sapropels would seem to be in good agreement with this notion.

However, the 2.7 kyr tuning lag between insolation and monsoon response was kept constant while constructing our Ti/Al chronology. The reason for this is that is the uncertainty about the presence of large scale cold spells in the Early Pleistocene, since evidence for cold spells is present throughout the record of Hodell et al. (2008) back to almost 1.4 Ma. Despite the 2.7 kyr lag assumed in our tuning the sapropels are estimated to be on average ~2 kyr older than the estimates of Emeis et al. (2000), and to hardly lag insolation forcing. We infer that there must have been a phase shift between the ocean response as reflected by sapropel deposition, and terrestrial response as reflected by the Ti/Al record. This could also be due to a misallocation of the sapropel borders or oxidation of the top of older sapropels. However, spectral cross-correlation between the Ti/Al and Ba/Al records confirms a similar phase difference in the interval 950-1400 ka, where no phase difference whatsoever is found in the top 340 ka.

Both the terrestrial and oceanic record are in principle driven by the activity of the North African Monsoon. Therefore, rather than a change in the monsoon response to insolation, we argue that the eastern Mediterranean basin must have been more susceptible to stratification in the

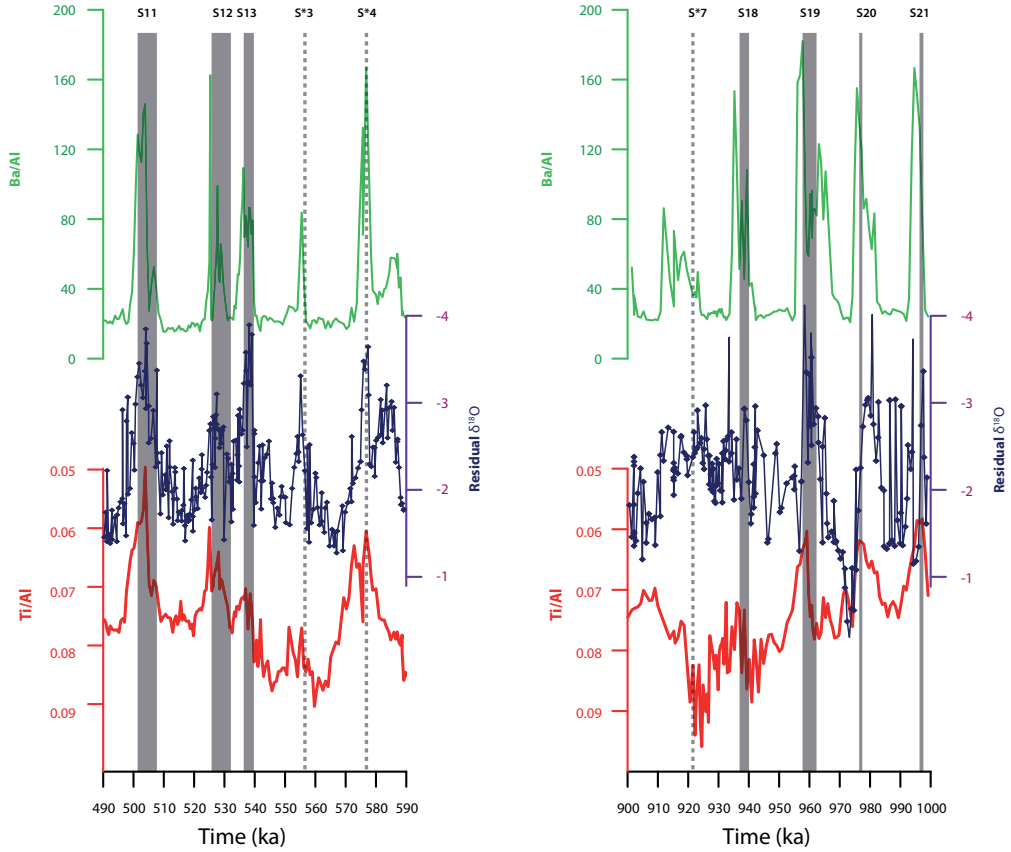

Figure 5.9: Top: the ODP 967 and 968 Ba/Al record (green); middle: the residual isotope record (dark blue); bottom: the Ti/Al record (red). Sapropels are indicated by vertical grey bars.

Early- and Middle Pleistocene. This would cause an earlier onset of sapropel formation, causing the midpoint of sapropels to be located deeper in the sequence. The resulting age estimates would be correspondingly older despite a 2.7 kyr lag of the monsoon to insolation as assumed in our tuning. Such an interpretation is in line with the finding of Lourens et al. (1996) that the alternation of thick and thin sapropel beds – reflecting the interference of precession with obliquity – correspond best to a 3 kyr lag to insolation forcing.

An alternative interpretation of these results is for the lag of Ti/Al to have increased earlier in the Pleistocene. Considering that the oceanic proxies – the sapropels, the Ba/Al ratio, organic carbon, and the residual benthic isotope record – behave consistently with each other, it seems that the Ti/Al record is the only one deviating. We interpret the Ti/Al record to represent Saharan aridity, related to the activity of the North African monsoon. But the residual isotopes with their salinity overprint should also reflect the North African monsoon. Yet these proxies exhibit diverging responses in the Early Pleistocene. Perhaps the Ti/Al record reflects or incorporates a different signal from just the summer monsoon, such as a winter signal influencing the storm tracks of the Mediterranean region. Or the North African monsoon affects the Nile catchment (mostly Sudan) differently from the Sahara, which could also influence the entire sapropel mechanism independently from the Ti/Al record. We can find no satisfactory answer to this quandary. There is

no direct evidence against the Ti/Al record reflecting the North African monsoon, and we therefore maintain it as the primary base of our age model.

5.4.2 Results of the residual signal

It is clear that Mediterranean surface ocean conditions are dominated by the influence of precession. While the planktonic record shows 100 kyr variability to carry the most power (figure 5.4), deduction of the global eustatic sea level component (i.e. the benthic oxygen isotope values) leaves the 23 kyr cycle as by far the most influential (figure 5.7).

The complete absence of 41 kyr power in the spectrum of the residual isotope record suggests that all 41 kyr variability in Mediterranean surface the ocean is derived from the global ice volume signal. This would seem plausible enough considering the low latitude setting of the record, rendering the expected influence of obliquity small. Yet it has been shown many times (Hilgen, 1991; Lourens et al., 1996; Larrasoaña et al., 2003; chapter 2) that the direct influence of obliquity on North African climate and the Mediterranean region is unmistakable. Such a signal is expected as a modulation of the salinity effect on the residual $\delta^{18}O$. The absence of 41 kyr power could be related to nonlinearity in the proxy response. For example largest salinity drops during the most extreme precession minima and related monsoon precipitation maxima might not be picked up by G. *ruber*, which supplies our $\delta^{18}O$. This could result in a cap on the salinity signal recorded in the residual $\delta^{18}O$, obscuring the 41 kyr modulation. Alternatively, the absence of 41 kyr variability in the $\delta^{18}O$ residual record might in part also be related to the strong coupling to the summer season. Whereas other proxies such as Ti/Al potentially reflect a more annually integrated signal with a stronger influence of the winter season.

The 23 kyr signal in the residual record is the most powerful in the spectrum, and therefore the most robust. This signal seems to coincide with, or slightly lead, sapropel depositions (figure 5.8). This would be expected from the model of Rossignol-Strick (1985) where a low salinity 'lid' on the surface ocean causes the stagnation of deep water and triggers sapropel deposition. Our analyses with the Mediterranean residual surface $\delta^{18}O$ signal thus confirm this aspect of the Nile Hypothesis.

The zero lag found between the 23 kyr signal and insolation is the result of removing the benthic component – which has a considerably larger lag: 6.0 kyr (chapter 3) – from the surface water signal. This result seems to suggest an immediate response to 65°N June 21st insolation of the surface ocean, once compensated for the eustatic component of the water. This would be in line with the model results of Tuenter et al. (2005), which also indicate an in-phase response in the absence of ice sheets. Upon closer inspection, however, the 23 kyr signal is not constantly in phase with insolation. In fact, considering how closely the signal is related to sapropel formation, the results of §5.4.1 also have bearing on this issue. In the last 800 kyr the residual signal slightly lags insolation (±0.8 kyr), whereas in the interval before 800 ka – when the shift in phase of sapropels becomes evident – the signal leads insolation by ±1.7 kyr on average. Both results are in agreement with the slight lead that the residual signal was observed to have over sapropel deposition.

5.4.3 Changing Mediterranean circulation during MIS 12 and 16

The high levels of Ba/Al deposited during MIS 12 and 16 would suggest large scale deposition of organic matter, but there is no indication of enrichment in organic matter in either interval. Sapropels, of which there are several within these intervals, do not appear to be more developed: they are not thicker nor richer in organic material than outside these intervals. At the same time, it is evident that the large scale deposition of Ba is somehow related to a shift in circulation: the

residual isotopic signal exhibits equally extreme excursions at the same intervals (figure 5.8). An additional indicator is that these intervals occur during the two most prominent glacials of the Pleistocene, where sea levels dropped by ~120 m compared to modern day levels (Bintanja et al., 2005; Rohling et al., 2009; Elderfield et al., 2012). This suggests that the extreme glacial conditions affected Mediterranean circulation, somehow triggering large-scale organic matter deposition while still ventilating the deep sea enough to break down the deposited material. These conditions are due to either a climatological effect or the direct result of the significant change in sea level associated with these glacials.

Hypothethically, a substantial drop in sea level could have affected circulation of the eastern Mediterranean basin considerably by restricting the exchange of water with the western basin through the shallow Strait of Sicily. The present day circulation features inflow of low salinity waters over the relatively broad surface (top ~100m) of the Strait, while Levantine Intermediate Water is exported through the narrow sections below (Astraldi et al., 2002). A sea level drop of more than 100 m, as during the major glacials after ~700 ka, would cause the shallows around Tunesia and Sicily to fall dry. This would confine all the flow to the very narrow channels 100 m below current sea level, accommodating much less exchange and greatly increasing friction. In such a scenario, the drop in sea level would be a direct cause for reduced deep water export by restricting the outflow of LIW and especially EMDW. We speculate that such a mechanism could explain the very large contrast between sea surface and deep water $\delta^{18}O$ in MIS 12 and 16 without the presence of a monsoon-induced freshwater lid. Modelling the exchange through the Strait of Sicily under low sea level conditions could provide more insight on this matter.

A shift in eastern Mediterranean circulation and a reduction in the export of nutrient rich deep water could result in much more efficient trapping of nutrients in the basin. This could increase production, resulting in the deposition of more organic material on the seafloor. However, in contrast to the situation during sapropel deposition, this organic matter would be degraded because enough oxygen is supplied to the seafloor to break down the increased supply. This might explain the high barium content of the deposits during these extreme glacial stages.

An alternative explanation may be sought in the findings of Kemp et al. (1999). Their study of sapropel 5 in the Late Pleistocene reveals high abundances of diatoms in the depositions, of the mat-forming rhizosolenid species. Their work suggests that blooms of these and other diatoms abound during sapropel formation. The colonial nature of these diatoms makes for efficient export of organic matter during supposed winter mixing episodes. Also, the rhizosolenids purportedly benefit from symbiosis with nitrogen fixating bacteria, allowing them to bloom under oligotrophic conditions. It is possible that limited circulation (Rohling et al., 2015) during the extreme glacials MIS 12 and 16 created the ideal circumstances for these diatoms to bloom, while still providing enough oxygen for the breakdown of the organic matter in the sediment. This would also reconcile the high barium levels with the absence of appreciable amounts or organic matter in the sediment.

While either model above may or may not adequately explain the extreme barium levels and deep sea-surface contrast, it doesn't explain why these are the only instances where they occur. We do see a similar response, to a much lesser degree, in MIS 10 (figure 5.8), but not in MIS 2 or 6. In fact, the only other intervals where remotely similar excursions are found occur in the cold interval between MIS 7.1 and 7.3 and on the descent into glacial values from MIS 7 to MIS 6. However, the global climate circumstances under which these last intervals occur are very different, and their intensity and duration are as well. Since we can find no factor linking them to the intervals of intense barium deposition in MIS 12 and 16, we consider them a separate anomaly. Meanwhile, from the absence of such depositions in MIS 2 and 6 we can only infer that the change

in circulation must be extremely sensitive to a particular threshold. MIS 12 and 16 are, after all, slightly heavier (i.e. slightly more glaciated) than the other glacials (Lisiecki and Raymo, 2005).

While the Red Sea reconstruction indicates levels of ~115 m below present day levels for the LGM, levels were 5-10 m lower in MIS 12, and remained low for a much longer period (Grant et al., 2014; Rohling et al., 2014). The duration of MIS 2 sea level at critical depths might have been too short for a new circulation pattern to establish itself or to significantly influence deep water composition and oxygenation. We note here that Grant et al. (2014) find only fractionally lower sea levels during MIS 12 than during MIS 2 in the Red Sea. Rohling et al. (2014) do not conclusively find lower sea levels during MIS 12 and 16 using their reconstruction based on the Mediterranean. In fact, these intervals are discarded as anomalous 'sapropel like' deposits due to their abnormal planktic isotope behavior as well as the strong Ba/Al excursions. Rohling et al. (2014) base their sea level estimates on a model of Gibraltar Strait flow. We argue that the particular bathymetry of the Sicilian Strait may have exerted additional, if not dominant, hydraulical control over the eastern Mediterranean during the most extreme periods low sea level. This possible caveat should not affect their sea level reconstructions for most of the record: Rohling et al. use numerous controls to constrain their sea level predictions. However, they themselves already note that MIS 12 and 16, as well as a small interval in MIS 14, from their eastern Mediterranean reconstruction are regarded less reliable. We assert that the particular intervals of very low sea level in the Late Pleistocene must indeed be considered unreliable until the mechanism behind these anomalies is fully understood.

5.5 Conclusions

The new MedStack presented here is an improvement on the one published by Lourens (2004), both in resolution and age model. Used in combination with the benthic isotope record of this same site (reflecting global ice volume and deep sea temperature) we gain insight into Mediterranean circulation changes over the course of the Pleistocene. The large contrasts found during, or just prior to, sapropel deposition agree well with the Nile Outflow/stratification hypothesis of Rossignol-Strick (1985) for sapropel formation.

We find remarkably elevated Ba/Al levels during MIS 12 and 16, not accompanied by organic matter deposits. The planktic and benthic isotope records indicate a high salinity and/or temperature contrast between the deep sea and surface ocean during these intervals. Possibly, extremely low sea level during MIS 12 and 16 forced a different circulation pattern in the eastern Mediterranean.

On the basis of our Ti/Al age model, we find that sapropel deposition does not lag insolation forcing with a constant 3 kyr. This lag was shorter, on average, in the Middle Pleistocene than it was in the '100-kyr world' of the Late Pleistocene. We observe a phase shift between the oceanic proxies (Ba/Al, isotopes, C-org) and the land-based Ti/Al proxy, which is persistently tuned with a 2.7 kyr lag to insolation.

Acknowledgements: This project was financially supported by NWO-ALW (project number 865.10.001). We acknowledge the Ocean Drilling Program in general, and Walter Hale and the Bremen Core Repository specifically for the samples used in this study. This work was initiated by L.J. Lourens. Lab work was performed by the other authors, and analyses by T.Y.M. Konijnendijk. T.Y.M. Konijnendijk wrote the manuscript, with contributions of the other authors.

De ervaring leert dat model-data vergelijkingsstudies een enorme impuls geven om te komen tot een kwantitatieve interpretatie van proxy-gegevens en een synthese van verschillende soorten proxies.

Nanne Weber

Chapter 6

Methane variations on orbital timescales: a transient modeling experiment

Methane (CH_4) variations on orbital timescales are often associated with variations in wetland coverage, most notably in the summer monsoon areas of the Northern Hemisphere. Here we test this assumption by simulating orbitally forced variations in global wetland emissions, using a simple wetland distribution and CH_4 emissions model that has been run on the output of a climate model (CLIMBER-2) containing atmosphere, ocean and vegetation components. The transient climate modeling simulation extends over the last 650 000 yr and includes variations in land-ice distribution and greenhouse gases. Tropical temperature and global vegetation are found to be the dominant controls for global CH_4 emissions and therefore atmospheric concentrations. The relative importance of wetland coverage, vegetation coverage, and emission temperatures depends on the specific climatic zone (boreal, tropics and Indian/Asian monsoon area) and timescale (precession, obliquity and glacial-interglacial timescales).

Despite the low spatial resolution of the climate model and crude parameterizations for methane production and release, simulated variations in CH_4 emissions agree well with those in measured concentrations, both in their time series and spectra. The simulated lags between emissions and orbital forcing also show close agreement with those found in measured data, both on the precession and obliquity timescale. We find causal links between atmospheric CH_4 concentrations and tropical temperatures and global vegetation, but only covariance between monsoon precipitation and CH_4 concentrations. The primary importance of the first two factors explains the lags found in the CH_4 record from ice cores. Simulation of the dynamical vegetation response to climate variation on orbital timescales would be needed to reduce the uncertainty in these preliminary attributions.

published as: Konijnendijk, T.Y.M., Weber, S.L., Tuenter, E., Weele, M. van, 2011. Methane variations on orbital timescales: a transient modeling experiment. *Climate of the Past* 7, 635–648 DOI: 10.5194/cp-7-635-2011

6.1 Introduction

As a greenhouse gas, methane (CH_4) is a forcing factor for climate (Wang et al., 1996). Vice versa, methane concentrations are also subjected to climate changes via changes in natural CH_4 production rate. The most important natural source of CH_4 is anaerobic decomposition of organic material in wetlands (Fung et al., 1991). Global wetland extent, together with more local factors influencing CH_4 production and release such as temperature and vegetation (Gedney et al., 2004), is therefore key to understanding variations in the atmospheric CH_4 concentration in the period before anthropogenic influences.

Variations in CH_4 concentration have been substantial during the late Quaternary. Spahni et al. (2005) found an increase in the Epica Dome C (EDC) ice core record of ~360 parts per billion by volume (ppbv) to ~690 ppbv during the transition from Last Glacial Maximum (LGM; 21.000 yrs before present) to the Early Holocene. Long-term oscillations in the CH_4 record have been linked to variations in insolation caused by orbital forcing, particularly to the 23,000 yr (23 kyr) precession component (e.g. Ruddiman and Raymo, 2003). Strong 41 kyr and 100 kyr components are apparent also in the record (Loulergue et al., 2008). These oscillations lag their respective forcing considerably. Ruddiman and Raymo (2003) devised an age model for the Vostok ice core by tuning the CH_4 signal to low latitude mid-July insolation with no additional lag. Their target curve, which is dominated by precession, effectively lags 21 June 65°N insolation by ~1.6 kyr. They also point out that the CH_4 signal has the same delayed phase as northern ice sheets at the obliquity timescale.

The exact nature of the link between insolation and variations in past atmospheric CH_4 concentration is a much-debated topic (Schmidt et al, 2004). The most common view on CH_4 variations at orbital timescales is that Northern Hemisphere (NH) extratropical (boreal) emissions are mainly influenced by changes in temperature, while tropical emissions are governed by changes in precipitation, i.e. monsoon intensity (Blunier et al, 1995). The land-sea temperature contrast that forces monsoon systems is sensitive to changes in insolation, in particular the 23 kyr cycle which therefore greatly influences the strength of monsoon systems (Kutzbach et al., 2008).

Given that the bulk of emissions originates from the tropical zones with a modest contribution from the extra-tropical NH, and negligible Southern Hemisphere (SH) emission (Walter et al., 2001; Prigent et al, 2007), it seems likely that changes in atmospheric CH_4 concentrations are primarily forced by changes in monsoon intensity (Chappellaz et al., 1990). However, Crowley (1991) noted that past atmospheric CH_4 concentrations compared just as favorably to reconstructed mid-latitude temperatures as they do to simulated Asian monsoon intensity. Therefore, changes in boreal emissions may well be the cause of the observed 23 kyr oscillation in atmospheric CH_4.

Modeling studies have recently been performed to investigate global wetland area and associated CH_4 emissions during the LGM (Kaplan, 2002; Valdes et al., 2005; Kaplan et al., 2006; Weber et al., 2010), thus implicitly focusing on the effects particular to a glacial termination. Here we perform a 650,000 year transient modeling experiment, with the aim to examine the climatic origin of orbital cycles in atmospheric methane. Focus is on the precession and obliquity (41 kyr) cycles. Questions that we want to address are whether the observed cycles in CH_4 originate in the tropics, in the boreal zone and/or specifically in the Indian/Asian monsoon area; which climatic parameters play an important role in each of these regions; and how we can interpret the lags that have been found in the measured data with respect to the orbital forcing.

Wetland CH_4 emissions over the last 650,000 years are derived from a transient climate simulation with an atmosphere-vegetation-ocean model of intermediate complexity (CLIMBER-2). The climate model output is used to force an off-line model that computes the global distributions of wetland area and CH_4 emissions (TRENCH: TRansient Emissions of Natural CH_4). §6.2 describes the models used. In §6.3 we analyze simulated emissions and examine the relative contribution to emission variations of the tropics, the boreal zone, and the Indian/Asian (I/A) monsoon area. The influence of changes in temperature, vegetation and hydrological processes is analyzed for each of the three regions. In §6.4 we discuss the results, compare model output to observational data, and draw conclusions.

6.2 Models and methods

6.2.1 The climate model

As a basis for simulating CH_4 emissions, the CLIMAte and BiosphERe model (CLIMBER-2, Petoukhov et al., 2000) was used. This is a coupled atmosphere-ocean-vegetation model of intermediate complexity that is suitable for long simulations due to its fast turnaround time. The model consists of a statistical-dynamical atmosphere, which resolves the large-scale flow that arises due to spatial temperature gradients. It parameterizes atmospheric transports due to synoptic-scale variations in a sophisticated manner (Petoukhov et al., 2000), but it does not contain the weather events themselves. The other components are a 3-basin zonally averaged ocean, including sea ice, and a terrestrial vegetation model VECODE (VEgetation COntinuous DEscription; Brovkin et al., 1997). The latter computes the fraction of the potential vegetation in a grid cell (i.e., grass, trees, and bare soil) as a function of the annual sum of positive day-temperatures and the annual precipitation. The atmospheric model of CLIMBER-2 has a resolution of 10° in latitude and 51.43° in longitude.

With CLIMBER-2 we performed a climate simulation for the interval 650 kyr BP to present, using orbital forcing (Laskar, 2004). Time-varying Northern Hemisphere (NH) ice sheets and greenhouse gas concentrations (GHG) are prescribed. The volumes of the Laurentide and the Eurasian ice sheet were obtained from a 3-dimensional ice sheet model coupled to a model of deep-ocean temperature (Bintanja et al., 2005). This model was forced by marine benthic oxygen isotopes (Lisiecki and Raymo, 2005) and was run in an inverse mode resulting in timeseries of the Laurentide and Eurasian ice sheet volumes. These volumes were translated into a surface area and height based on the ICE-5G distribution for the LGM until present (Peltier, 2005), set on the spatial grid of CLIMBER-2. Sea level effects due to changes in ice volume are not considered in this study. The increased capacity of continental flats falling dry for wetlands could partially compensate for the loss of boreal wetland area due to ice cover (Weber et al., 2010). However, this effect is difficult to simulate within the CLIMBER-2 grid and it is likely a minor factor in comparison to the main climate factors that are considered in this study.

GHG concentrations (CO_2 and CH_4) were derived from EPICA Dome C, with the EDC3 timescale (Lüthi et al., 2008; Loulergue et al., 2008). For the last 500 years we used values from several sources (Robertson et al., 2001). The total greenhouse gas forcing is dominated by CO_2. Therefore, the simulated climate is only determined by the measured CH_4 concentration variations to a very limited extent. The CLIMBER-2 simulation is described in detail by Weber and Tuenter (2011).

For the present purpose of estimating wetland CH_4 emissions over orbital timescales it is relevant to assess the model's sensitivity to the different forcings involved. These include both internal forcing mechanisms, such as ice sheets and greenhouse gases, as well as external orbital forcing. Compared to General Circulation Models (GCMs), the main drawback of CLIMBER-2 is obviously its coarse resolution and associated parameterizations of small-scale dynamical processes. CLIMBER-2 is however successful in simulating cold climates like the LGM (Ganopolski et al., 1998a), showing a similar sensitivity and response pattern as comprehensive GCMs to the separate impacts of large continental ice sheets and reduced greenhouse gases (Schneider von Deimling et al., 2006). Also, the strength of the NH monsoon during an orbitally forced period like the mid-Holocene lies within the range simulated by GCMs (Ganopolski et al, 1998b; Braconnot et al., 2007). Leads and lags with respect to the orbital forcing were also found to be similar to those found in more complex models (Tuenter et al., 2005; Kutzbach et al., 2008). CLIMBER-2 thus

seems capable of adequately representing climatic change in response to different forcings, albeit only at a large spatial scale.

6.2.2 CH_4 emissions model

The wetland and CH_4 emission model TRENCH is driven off-line by 100-yr averaged monthly output from CLIMBER-2. The monthly output permits the analysis of seasonal variations in wetlands and CH_4 emissions. TRENCH consists of two consecutive components: a wetland extent algorithm and a CH_4 emission algorithm. The wetland location algorithm follows the approach originally proposed by Kaplan (2002), and uses climate variables from CLIMBER-2 that are known to influence wetland formation. Wetland existence is determined based on soil moisture and soil temperature. Wetlands are assumed to exist only during months when the soil temperature is above freezing point. When, in addition, a soil moisture threshold (5% of maximum saturation) is reached, a grid cell is assumed to support wetlands. The fraction of a grid cell covered by wetland is linearly related to the soil moisture value derived from CLIMBER-2 as follows:

$$C_{wet} = a * M * (1 - I) \quad (1)$$

Where C_{wet} is the fraction of wetland in a grid cell, a is a tuning factor, M is the soil moisture, and I is the fraction of a grid cell covered with land ice. Resulting grid cell fractions are multiplied with the land surface area in a grid cell to obtain wetland area in km^2. We assume that orography does not play a role at the present spatial resolution, as a grid cell always contains sufficient flat terrain to support wetlands when climatic conditions allow this. The wetland algorithm was tuned to obtain a reasonable geographical distribution of wetlands and a plausible value for worldwide wetland extent in km^2, which is comparable to values in literature.

The CH_4 emission algorithm of TRENCH is based on Gedney et al. (2004), who propose a simple model for emissions dependent on wetland fraction, soil carbon content, and temperature. The temperature sensitivity is expressed in the form of a Q_{10} factor. In the present model we compute time-varying emissions for each grid cell as follows:

$$E = k * C_{wet} * V * Q_{10}^{T/10} \quad (2)$$

Here E is the CH_4 emission (in Tg CH_4 of a given grid cell at a certain time step and month, k is a tunable constant, C_{wet} is the fraction of wetland in a grid cell as calculated in the wetland distribution model (Eq. 1), and V a vegetation factor. The temperature sensitivity is expressed in the form of a Q_{10} factor, with T the soil temperature in degrees Celsius.

The Q_{10} is a temperature-dependant variable itself, because the efficiency of CH_4 production changes with temperature (Gedney et al., 2004). In literature, values for Q_{10} vary between 1.7-16 (e.g. Walter and Heimann, 2000). Most studies converge at values around 2-4, but large differences remain as a result of different locations and covarying processes involved when calculating in the Q_{10} value (Segers, 1998). Studies estimating Q_{10} values often perform measurements on one or more wetland sites. Because of the global scale of modeling and simplicity of the basic emission model in this study, a range of Q_{10} values may be plausible. The base value $Q_{10}(T_0)$ – the Q_{10} at 0°C – was set at 2.0, at which value the distribution of CH_4 emissions over boreal wetlands (north of 30°N)

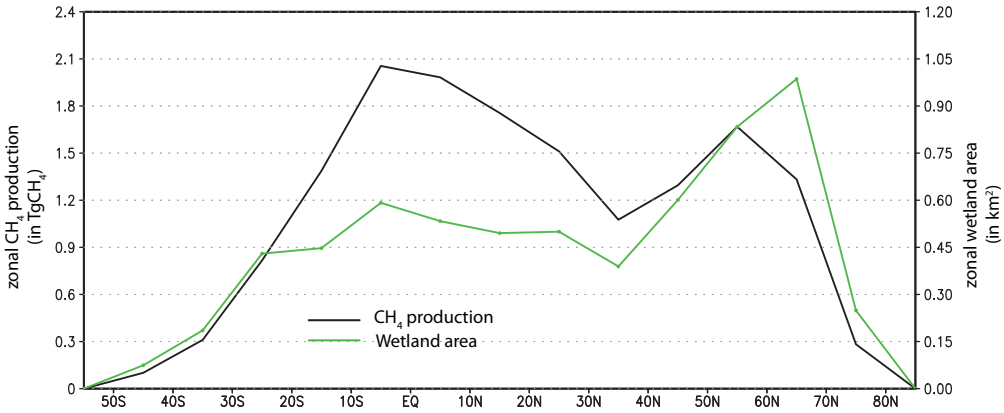

Figure 6.1: TRENCH simulated PIH wetlands during the month of maximum wetland extent (green line), and emissions (black line), both integrated zonally and by 10° latitude belts.

and tropical wetlands (latitudes between 30°N and 30°S) agrees with previous observational and modeling studies.

Wetland CH_4 production also depends on the soil carbon content, which is basically the amount of decomposable organic material in the substrate (Christensen et al., 2003). As this is not simulated by the present version of CLIMBER-2, we used the grass and trees vegetation cover fractions F_{grass} and F_{trees}, provided by VECODE, as the best estimate. In addition to the production of organic material, vegetation related root systems are important for the transport of CH_4 to the surface (Rice et al., 2010). Trees have more extensive root systems than grass and the litter that falls off trees provides more organic material than grass. For these reasons we added the two vegetation fractions, attributing 50% more weight to F_{trees} than to F_{grass}, to form the vegetation factor V. The results were not found to be sensitive to the exact percentage value.

The k factor was chosen to obtain global annual emissions of ~150 Tg CH_4 for the Pre-Industrial Holocene (PIH; 1850 AD). This target value is based on estimates of contemporary wetland emissions by Houweling et al. (2000) and Chen and Prinn (2006). TRENCH was thus tuned to reproduce the basic features of wetland distribution and CH_4 emissions for the PIH. In order to assess model performance, the results for the LGM were compared to those of earlier studies using GCMs.

6.2.3 Model performance for the PIH and LGM

The calculated maximum global wetland extent for the PIH occurs in June and is 6.3 10^6 km^2. During minimum inundation, which occurs in December, the total wetland area is 3.6 10^6 km^2. Taking into account that PIH wetlands were possibly ~20% larger than today due to destruction by agriculture (Chappellaz et al., 1993), this agrees with contemporary estimates based on satellite data of 5.9 10^6 km^2 and 2.1 10^6 km^2, respectively (Prigent et al., 2007). Boreal wetlands (annual average) make out 38% of the global annual mean, which is consistent with estimates for the present (Lehner and Döll, 2004; Prigent et al., 2007). Simulated wetland extent peaks in high northern latitudes (45°N-65°N), while extensive wetlands are also found in the tropics (figure 6.1).

Total simulated annual emissions amount to 151 Tg CH_4, of which 35 Tg (23%) originates in boreal wetlands and 116 Tg (77%) in the tropics. This distribution is in agreement with many previous observational and modeling studies, which find that 15-37% of the global emissions

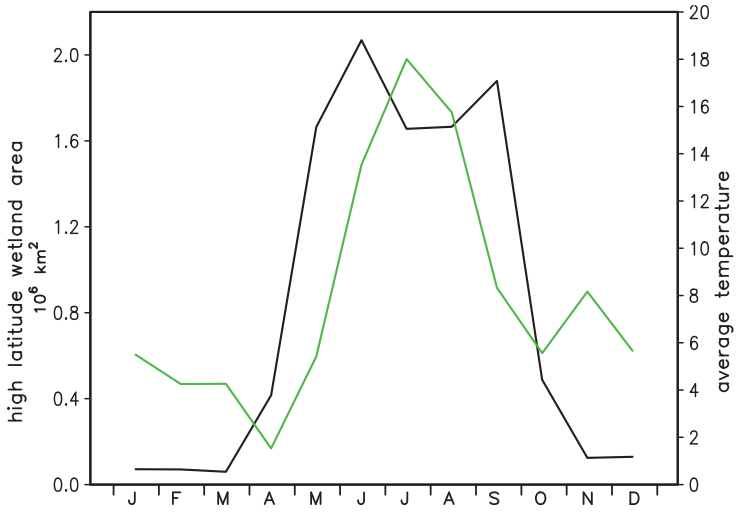

Figure 6.2: Seasonal variation of high (55–75N) latitude boreal wetland extent (black line) and emission temperature (defined as the average soil temperature of grid cells emitting CH_4; green line) during the PIH.

comes from boreal wetlands and 56-85% originates in tropical wetlands (Cao et al., 1996; Walter et al., 2001; Valdes et al, 2005). Boreal wetland area peaks during early summer when snowmelt rates surge, but the average temperature is still low (figure 6.2). Together with the limited emission season this makes the higher latitudes a less efficient source of CH_4 than the tropics. Therefore, the peak in simulated wetland extent in the high latitudes only translates in a moderate level of emissions (figure 6.1).

Global wetland area during the LGM is at its maximum in June with 5.3 10^6 km^2 and at its minimum in December with 3.3 10^6 km^2, a decrease of 17% in the annual-mean compared to the PIH. Boreal wetlands make up ~26% of the annual global mean, shifting the main component of wetland extent towards the tropics. This change of distribution is caused by the presence of large continental ice sheets at high latitudes and a relatively dry Eurasian mainland during the LGM due to generally reduced precipitation. There is a decrease in global CH_4 emissions between the PIH and LGM to 118 Tg CH_4/yr (21%). Tropical emissions are reduced by 12%, while boreal emissions drop by 58%. Previous GCM-based modeling studies have found similar moderate reductions in global emissions of 16-29% (Kaplan, 2002; Valdes et al., 2005; Kaplan et al., 2006) as well as stronger reductions of 29-42% (Weber et al., 2010).

A large cooling occurs in higher latitudes during the LGM. For example, Wu et al. (2007) reconstructed a 10°C surface cooling in the Northern Hemisphere (NH), while only minor to moderate cooling takes place in the tropics: 0-3°C. This is accurately simulated by CLIMBER-2 (figure 6.3). The strong cooling of the boreal zone limits the ability of large areas to sustain wetlands during most of the year due to the temperature constraint (§6.2.2). This temperature-effect is larger than the direct loss of wetland area by ice cover. Additionally, the decreasing temperature has a negative impact on vegetation growth. Figure 6.3 shows that vegetation cover was strongly diminished in the LGM with respect to the PIH in boreal latitudes, while there is little change in the tropics.

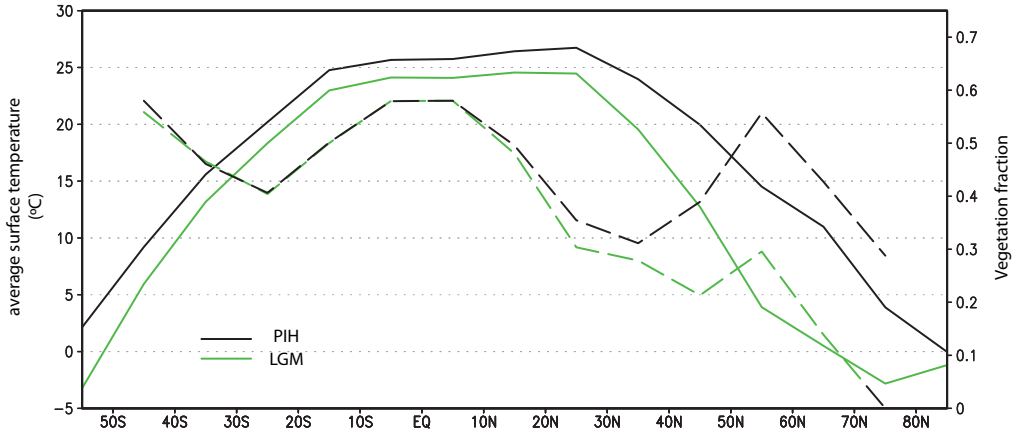

Figure 6.3: CLIMBER-2 simulated PIH temperature (solid black line) and LGM temperature (solid green line) for the NH summer months, and annual-mean grid-box vegetation factor (section 2.2) during the PIH (dashed black line) and LGM (dashed green line). Note that the vegetation factor is a weighted average of tree cover (60%) and grass cover (40%). All data are integrated zonally and by 10° latitude belts.

6.3 Main sources and controls of wetland methane emissions

6.3.1 Simulated emissions in the transient run

Figure 6.4 shows timeseries of the forcings used in the transient run, namely ice volume, greenhouse gas variations and insolation at 65°N as an illustration of the orbital forcing. We also show the global mean values of the main climatic parameters, as derived from CLIMBER-2, determining wetland CH_4 emissions, wetland extent and the emission temperature (average temperature over grid cells emitting CH_4), as well as the vegetation cover. All parameters show variations on multiple (orbital) timescales. Simulated temperature and vegetation changes, together with the varying wetland distribution, were used to compute total annual and global CH_4 emissions. These were found to vary between 116 and 167 Tg/yr. In figure 6.5 the global CH_4 emissions are compared to the atmospheric CH_4 concentrations derived from EDC. The EDC3 curve shows pronounced sub-orbital variability, which is absent from the simulated curve. This is because CLIMBER-2 lacks internally-generated variations on these timescales. Simulated climate and vegetation are driven by the applied forcings, which vary on orbital timescales. The longer-timescale variations (>3 kyr) in both curves correspond very well (r = 0.79).

As wetlands are the main natural source, wetland CH_4 emissions for a large part determine atmospheric concentrations during this period. Therefore we directly compare measured concentrations and simulated wetland emissions here. Spectra of the two time series were determined using Analyseries (Pailliard et al., 1996). Both spectra (figure 6.6) indicate a strong 100 kyr signal and significant influence of 41 kyr oscillations. Precession related features (i.e. 23 kyr) show a stronger signal in the model results than in the measured data. However, differences in the relative importance of spectral peaks in measured concentrations and simulated global emissions could be due to lifetime variations that cannot be accounted for in the present model set-up. The atmospheric CH_4 lifetime was tentatively diagnosed from the measured concentrations and simulated total wetland emissions. Assuming a constant biomass burning source of 40 Tg CH_4/yr (Fisher et al., 2008) and additional covarying sources, like ruminants, termites and geological sources, amounting to 30 Tg CH_4/yr during the PIH (Denman et al., 2007), we find that lifetimes vary between ~5.5 year during periods of low CH_4 concentrations, and ~9 year during periods

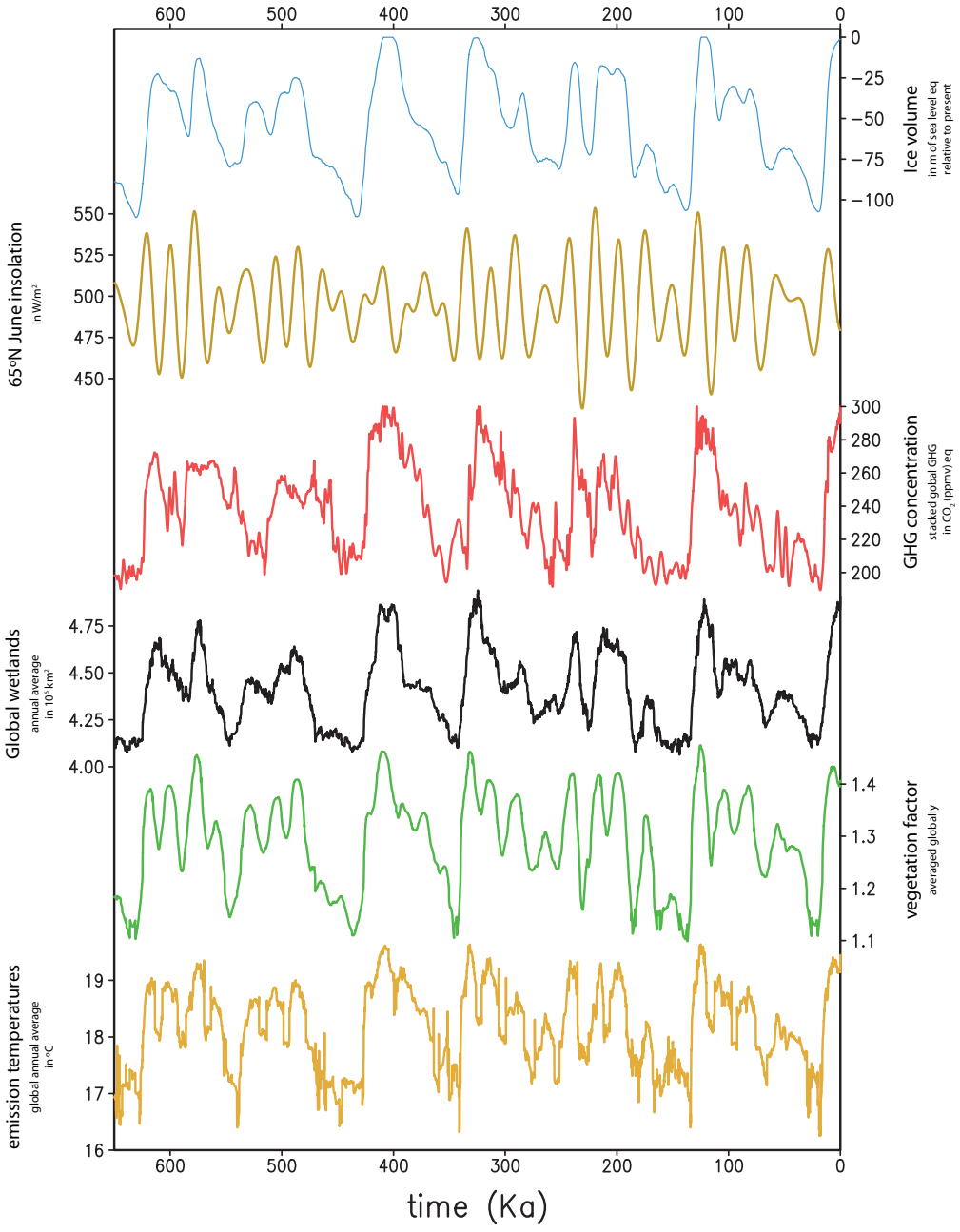

Figure 6.4:Transient forcings (top graphs) for CLIMBER-2 and the resulting wetland extent, vegetation factor and mean emission temperature (lower graphs).

of high CH_4 concentrations. These are reasonable values, which support our conclusion of close correspondence between the measured and simulated timeseries.

In order to further analyze the origin of simulated wetland emissions we separately consider three regions (figure 6.7): the areas influenced by the I/A summer monsoon, the boreal area north of 30°N, but excluding the East Asian monsoon grid box, and the tropical area, 30°S-30°N, excluding the remaining monsoon-dominated grid boxes. The I/A monsoon is analyzed separately as this area is generally assumed to be an important source of wetland emissions (Kutzbach et al., 2008). Moreover, this area is found to exhibit different behavior from the equatorial tropics where shifts in the Intertropical Convergence Zone (ITCZ) determine whether wetlands can exist or not. The bulk of global emissions (72% during the PIH) are emitted from the tropics. The boreal zone and the monsoon areas contribute the remainder (18% and 9% respectively). The spectra for the individual regions (figure 6.6) show that they each have a typical timescale behavior, as mentioned above. Emissions from the I/A monsoon area are primarily controlled by precession, with little to no influence from 100 kyr and 41 kyr. Boreal emissions mainly reflect 41 kyr and 100 kyr signals, while tropical emissions contain a strong precession signal and significant power at the 41 kyr and 100 kyr frequencies.

The EDC3 record for CH_4 and the time series for simulated global emissions, as well as those of the separate regions, were band pass filtered using Analyseries (Pailliard et al., 1996) at 21 (±2.5) kyr and 41 (±3.5) kyr. The filtered signals were then cross correlated to the astronomical precession index and obliquity parameter, respectively (Laskar, 2004). The measured EDC3 derived methane concentration is found to lag the orbital forcing by 2.0 kyr on the precession timescale and by 5.5 kyr on the obliquity timescale (table 6.1). For the simulated global emissions lags are 1.3 kyr for precession and 5.3 kyr for obliquity, respectively, (figure 6.8). We consider this a very close match given that climate models are generally not successful in reproducing lags found in measured data (e.g. Ziegler et al., 2010). Lags are longest for emissions from the boreal zone and smallest for emissions from the monsoon areas, with intermediate lags for tropical emissions (table 6.1).

6.3.2 Factor Analyses

The next step is to analyze the climate and vegetation factors that control variations in simulated CH_4 emissions and the simulated lags. First we define a total modification factor F_{tot} as follows:

$$F_{tot}(t) = E(t)/E_{PIH} \quad (3)$$

Where E denotes annual emissions, t is time and E_{PIH} denotes annual emissions during the PIH. According to Eq. 2 there are three individual factors determining the total emission changes, namely changes in wetland cover (Fc), in vegetation cover (Fv) and in temperature (Ft). To compute individual modification factors for each grid box, one term in Eq. 2 was set at its transient value and the other two terms were set at PIH values. The results were then divided by the emissions of that grid box for the PIH. Eq. 4 shows this factorial calculation for wetland cover (Fc):

$$Fc(t) = k * C(t) * V_{PIH} * Q_{10}{}^{T/10}{}_{PIH}/E_{PIH} \quad (4)$$

Where k is the unaltered tunable constant, C(t) is the transient wetland cover, V_{PIH} is the vegetation cover and $Q_{10}{}^{T/10}{}_{PIH}$ is the temperature dependence, both fixed at their PIH values. For each grid box F_{tot} is equal to Fc * Fv * Ft. The results from the factor analysis are averaged globally and for the three separate zones defined above using a weighted average. By weighing the modification

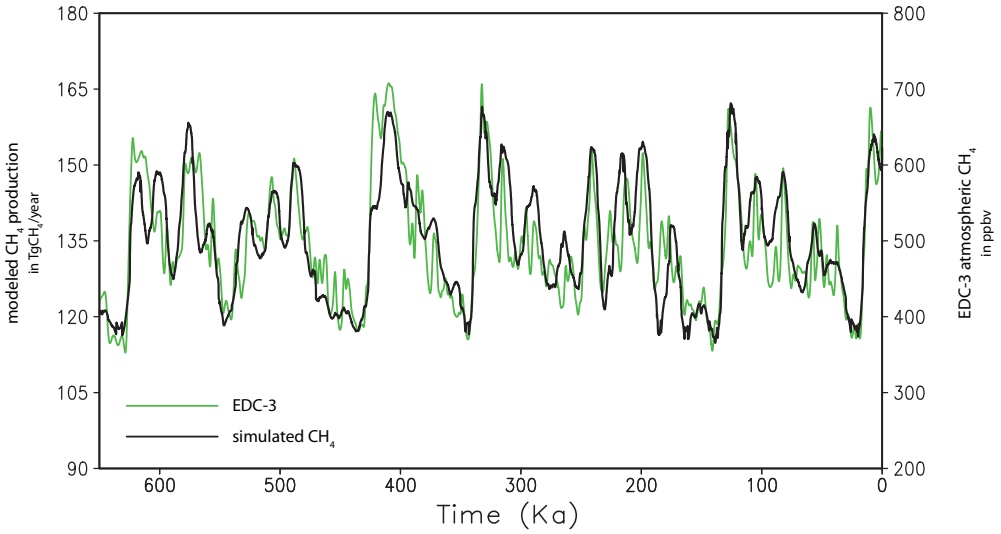

Figure 6.5:Epica Dome C atmospheric CH_4 concentrations (green line; in ppbv), low pass filtered for timescales longer than 3 kyr, and TRENCH simulated annual global CH_4 emissions (black line; in $TgCH_4$).

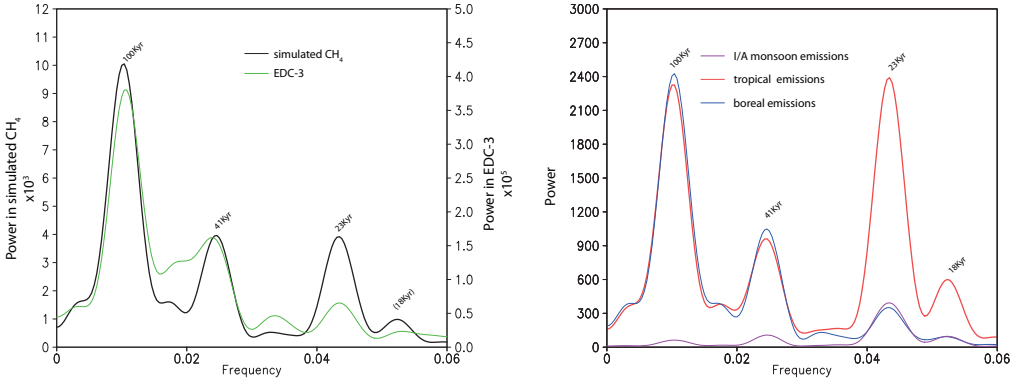

Figure 6.6: (left) Spectra for the Epica Dome C atmospheric CH_4 concentrations (green line) and the TRENCH simulated annual global CH_4 emissions (black line), both computed over the time series extending from 650 kyr to 0 kyr BP. (right). Spectra for the time series of the separate emissions from the tropical zone (red line), the boreal zone (blue line) and the I/A monsoon areas (violet line); the areas are depicted in fgure 6.7.

Table 6.1:Lags with respect to the orbital forcing in ice cover, greenhouse gases and EDC3 atmospheric CH_4, in the TRENCH simulated global and regional emissions and in the global modification factors. Lags are computed by searching for the optimum correlation between the forcing (precession or obliquity) and a given variable, band pass filtered at 21 kyr or 41 kyr, respectively. Zero phase is set at minimum precession and maximum obliquity, which each correspond to an insolation maximum for the NH. The correlation value is displayed next to the lag.

Factor	precession	correlation	obliquity	correlation
Ice cover	4.7	-0.86	7.1	-0.94
GHG	-	-	6.0	0.91
EDC3	2.0	0.78	5.5	0.95
Global emissions	1.3	0.93	5.3	0.96
boreal emissions	2.5	0.88	6.3	0.97
tropical emissions	0.7	0.95	4.4	0.96
Indian/Asian monsoon emissions	0.5	0.95	2.6	0.96
Global modification factor	1.1	0.94	4.7	0.97
Global wetland modification factor	2.1	0.88	3.2	0.95
Global vegetation modification factor	0.5	0.94	3.2	0.97
Global temperature modification factor	2.1	0.87	6.9	0.96

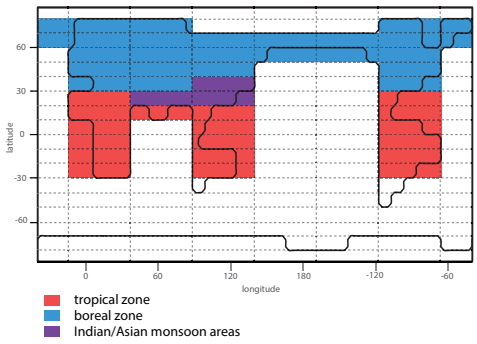

Figure 6.7: definition of the tropical (red), boreal (blue) and Indian/Asian monsoon (pink) zones. Emissions from these three zones are separately analyzed.

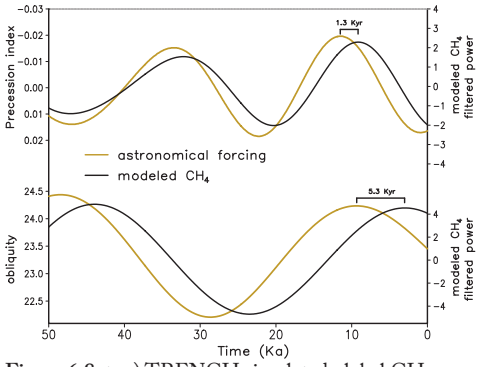

Figure 6.8: top) TRENCH simulated global CH_4 emissions, band pass filtered for 21 kyr (±2.5kyr) and the precession index, and (bottom) TRENCH simulated global CH_4 emissions, band pass filtered at 41k (±3 kyr), and the obliquity parameter. Lags between forcing and response are indicated for each timescale.

factors of each grid box according to their PIH emissions in the averaging process, skewing effects of extreme modifications in low-emission cells such as in high boreal latitudes are countered.

Timeseries of the modification factors (figure 6.9) show that temperature is the dominant control both for tropical and boreal emissions, with vegetation as a secondary role. During cold periods wetland extent is a reducing factor in the boreal zone, but an amplifying factor in the tropics, possibly related to reduced evaporation. However, the effect is small in both zones and almost cancels out in the global mean. Wetlands coverage is only an important factor in the I/A monsoon region, together with vegetation changes.

Spectral analyses (figure 6.10) show that precession-related variability is dominated by vegetation changes in the tropics and in the I/A monsoon region, while in the boreal zone a combination of temperature and vegetation changes play a role. This results in global emissions dominated by vegetation at the precession timescale, with a smaller impact from temperature. At

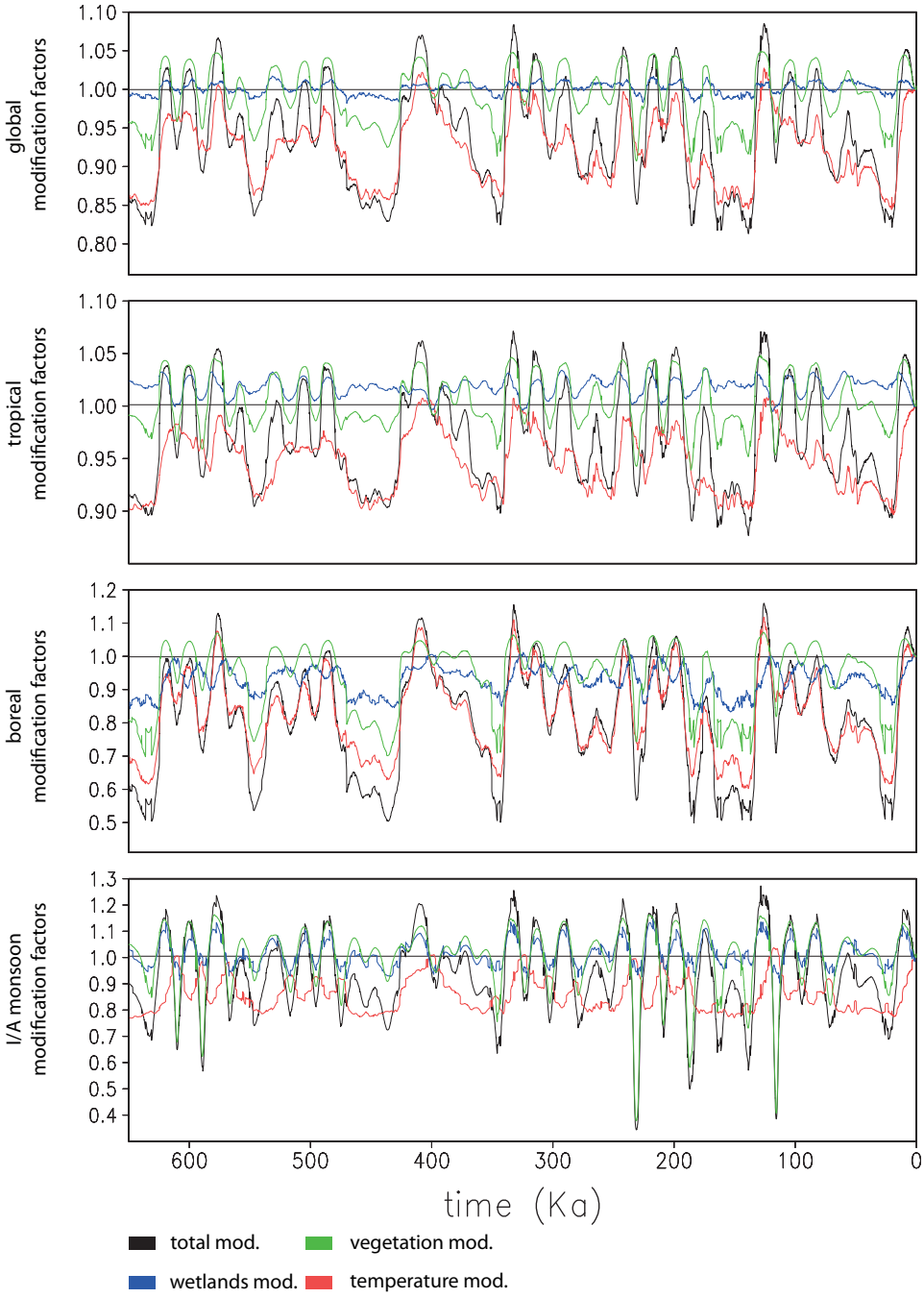

Figure 6.9: time series of the modification factors, as defined in §6.3.2, for the entire globe and for the tropical, boreal and Indian/Asian monsoon areas separately.

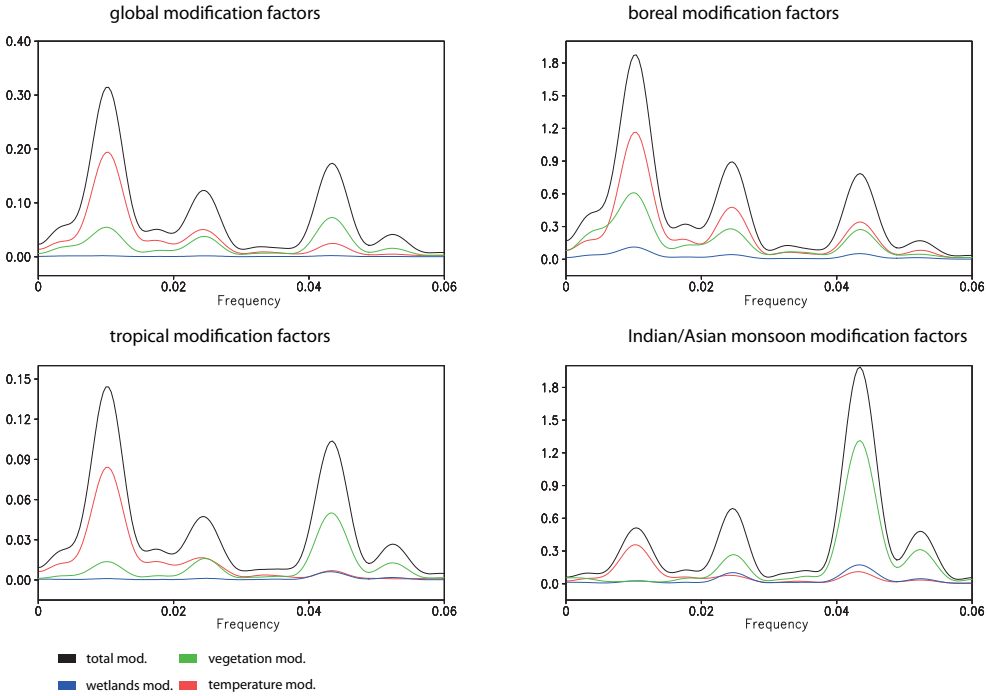

Figure 6.10: spectra of the modification factors (see §6.3.2) for the entire globe, and for the tropical, boreal and Indian/Asian monsoon areas separately.

the obliquity timescale temperature and vegetation are equally important in global emissions, which reflect both boreal and tropical results. Vegetation only dominates in the I/A monsoon area. The 100 kyr variations in global emissions are primarily determined by temperature, which is a global phenomena present in all three zones.

To summarize, at the precession timescale vegetation is the dominant control of global methane emissions, with temperature as a secondary control. The dominance of vegetation control originates primarily from the tropics. There is also a clear impact of vegetation in the I/A monsoon area, but these constitute only a small part of the global emissions. At the obliquity timescale temperature and vegetation play equally important roles. The temperature changes are almost completely in phase with ice volume minima/greenhouse gas maxima. Vegetation changes lag summer insolation maxima by ca. 1 kyr for precession to 2-4 kyr for obliquity (table 6.1). This reflects the strong influence of hydrological processes, which respond quasi-instantaneously to the orbital forcing, on vegetation. For both temperature and vegetation lags tend to be longer in the boreal zone than in the tropics (table 6.1). The combined effect of temperature and vegetation, explains the lags that are found between simulated methane emissions and the orbital forcings.

6.4 Summary, discussion and conclusions

We have simulated wetland CH_4 emissions over the last 650,000 yrs using a simple wetland distribution and CH_4 emissions model coupled off-line to the atmosphere-ocean-vegetation climate model CLIMBER-2. The resulting simulated global emissions show a close similarity to the measured EDC3 timeseries of atmospheric CH_4 concentrations, both in spectra and in lags

with respect to the orbital forcing. Diagnosed CH_4 lifetimes vary between ~5.5 and 9 yr on glacial-interglacial timescales, with 8.2 yrs as estimated for the PIH. This is consistent with data (Fisher et al., 2008) and model studies that include atmospheric chemistry (Lelieveld et al., 1998).

Global emissions are dominated by emissions from the tropics. However, in contrast to the general assertion that monsoon intensity is of primary importance (Chappellaz et al., 1990; Blunier et al., 1995) we find that temperature and vegetation changes are the main drivers. The I/A monsoon area is too small in size to contribute substantially to global emissions. As hypothesized by Crowley (1999), monsoon precipitation and global emissions do co-vary, but there is no causal link in our model. For the remainder of the tropics, wetland extent exerts little control on emissions. Tropical temperature variations are found to be small, about 2-4 °C on glacial-interglacial timescales in agreement with proxy data (Farrera et al., 1999). However, such variations are significant as methanogenesis is much more sensitive to temperature changes at the high average temperatures in the tropics than at the lower average temperatures at high latitudes (compare Eq. 2).

The present results show that temperature and vegetation are the dominant controls of orbital-scale variations in global wetland CH_4 emissions, while wetland extent plays a minor role. This is supported by a recent modeling study, based on an eight-member ensemble of GCM simulations for the LGM, which also found temperature and vegetation as the main controlling factors (Weber et al., 2010). In the latter study wetlands exhibited southward shifts in the cold LGM climate, related to a southward shift of the mid-latitude storm tracks and the ITCZ. This caused the effect of changes in wetland distribution to cancel out in the global mean. Here we find a shift from the boreal to the tropical zone. This larger-scale pattern is likely related to the coarse resolution of CLIMBER-2 and the fact that the atmospheric dynamics are simplified, so that storm tracks are not resolved. This is a shortcoming of the present simulation. However, it does not seem to affect our main conclusion on the primary role of temperature and vegetation.

Orbital cycles in vegetation have been found in many studies based on pollen data, for example for tropical South America (Hooghiemstra et al., 1993), Southeast Asia (Tsukada, 1996), Europe (Tzedakis et al., 2009) and North America (Whitlock and Bartlein, 1997). These studies indicate large shifts in vegetation presence and cover type. The vegetation model used in the present study only very crudely resolves such shifts. Nevertheless, we believe that our results on the role of vegetation are qualitatively valid although precise quantitative estimates are not possible using CLIMBER-2.

Finally, our results provide a plausible explanation for the lags found in the measured EDC3 curve with respect to the orbital forcing. Atmospheric CH_4 concentrations have previously been related to monsoon precipitation (Ruddiman and Raymo, 2003). Here we find that lags in the CH_4 record are very likely due to temperature and vegetation effects rather than monsoon precipitation. The former two factors have a phasing in-between insolation maxima and ice sheet/greenhouse gas minima. This results in lags that are very close to those found in measured CH_4 data, both at the precession and obliquity timescale. In contrast, simulated monsoon precipitation has zero lag at the precession band (Weber and Tuenter, 2011). This is inconsistent with any proxy-based estimate, as proxy records which have been interpreted as reflecting Indian/Asian summer monsoons have been found to lag precession by lags varying from 3 kyr (Wang et al., 2008) to considerably longer lags of up to 8 kyr (Clemens and Prell, 2003). Process-based modeling of proxies seems a necessary step to substantiate a reinterpretation of proxy records (Ziegler et al., 2010; Clemens et al., 2010) and to resolve this mismatch among different proxy data as well as between simulated and measured records.

Appendix I

The cores of ODP Site 967 (Holes A-D) lined up by CR at 550 nm over the revised composite depth of chapter 2. The composite splice is depicted in a bold line: bold intervals in the individual cores are used for the composite

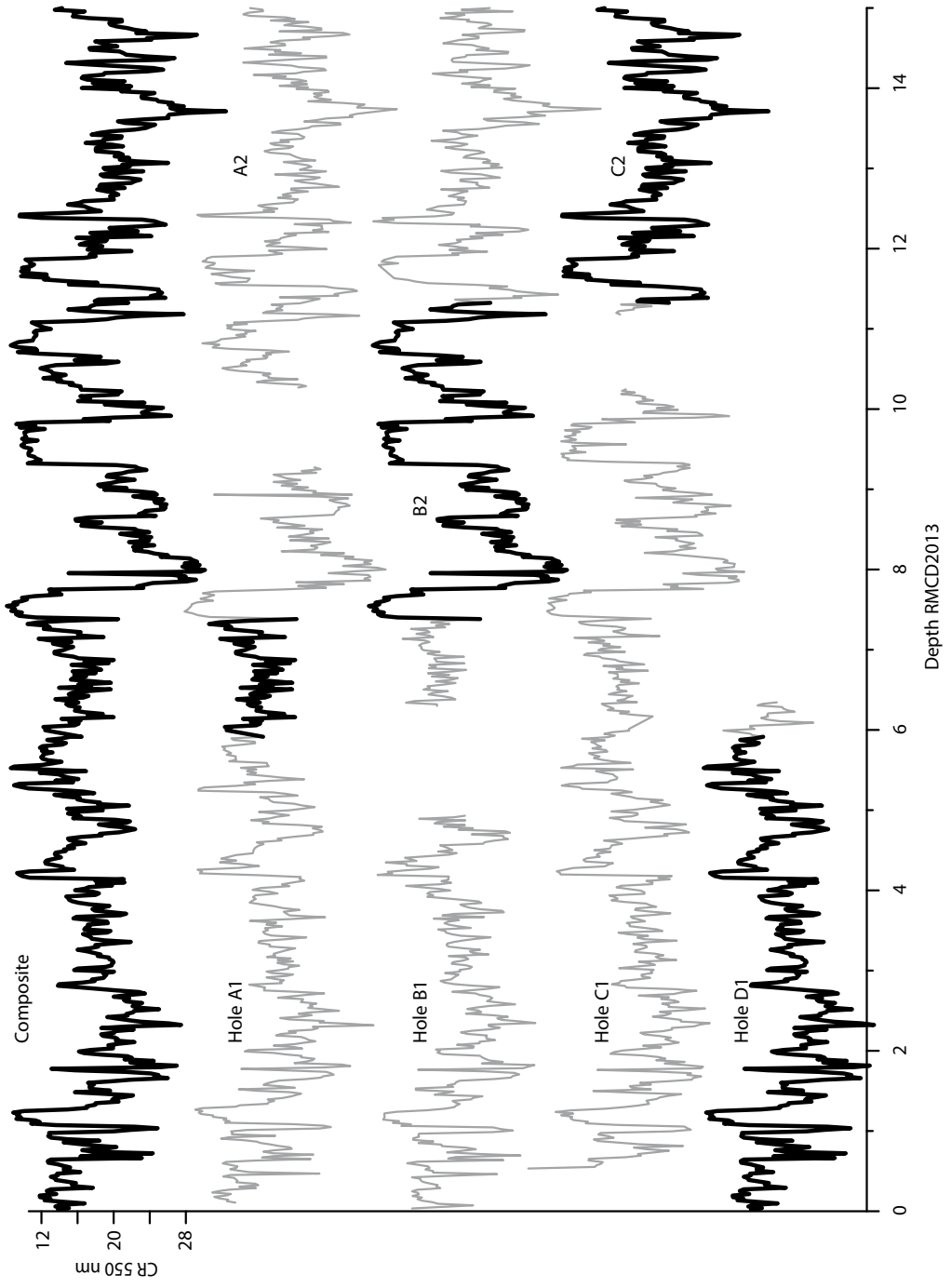

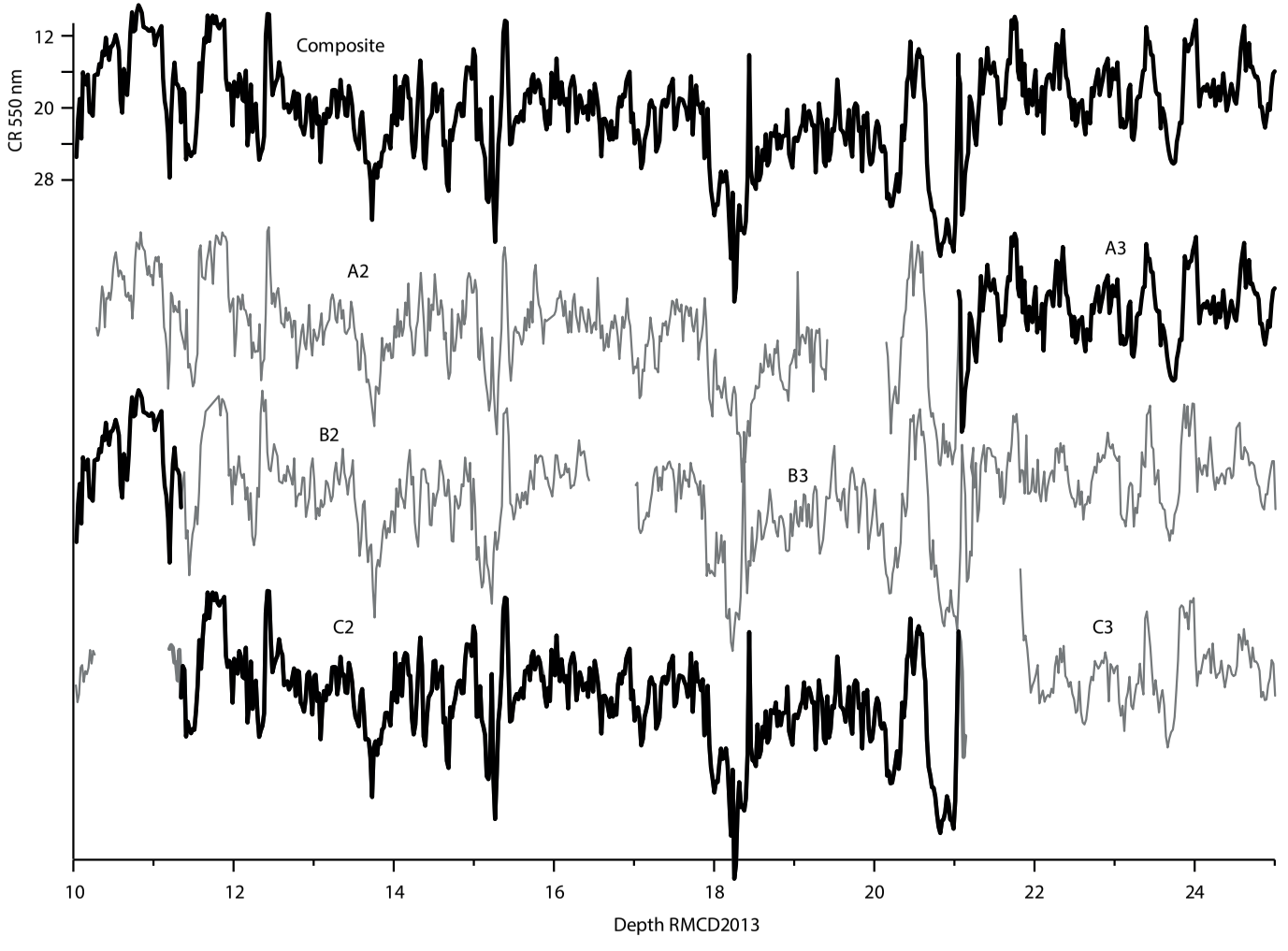
Composite
A2
A3
B2
B3
C2
C3
CR 550 nm
12
20
28
10
12
14
16
18
20
22
24
Depth RMCD2013

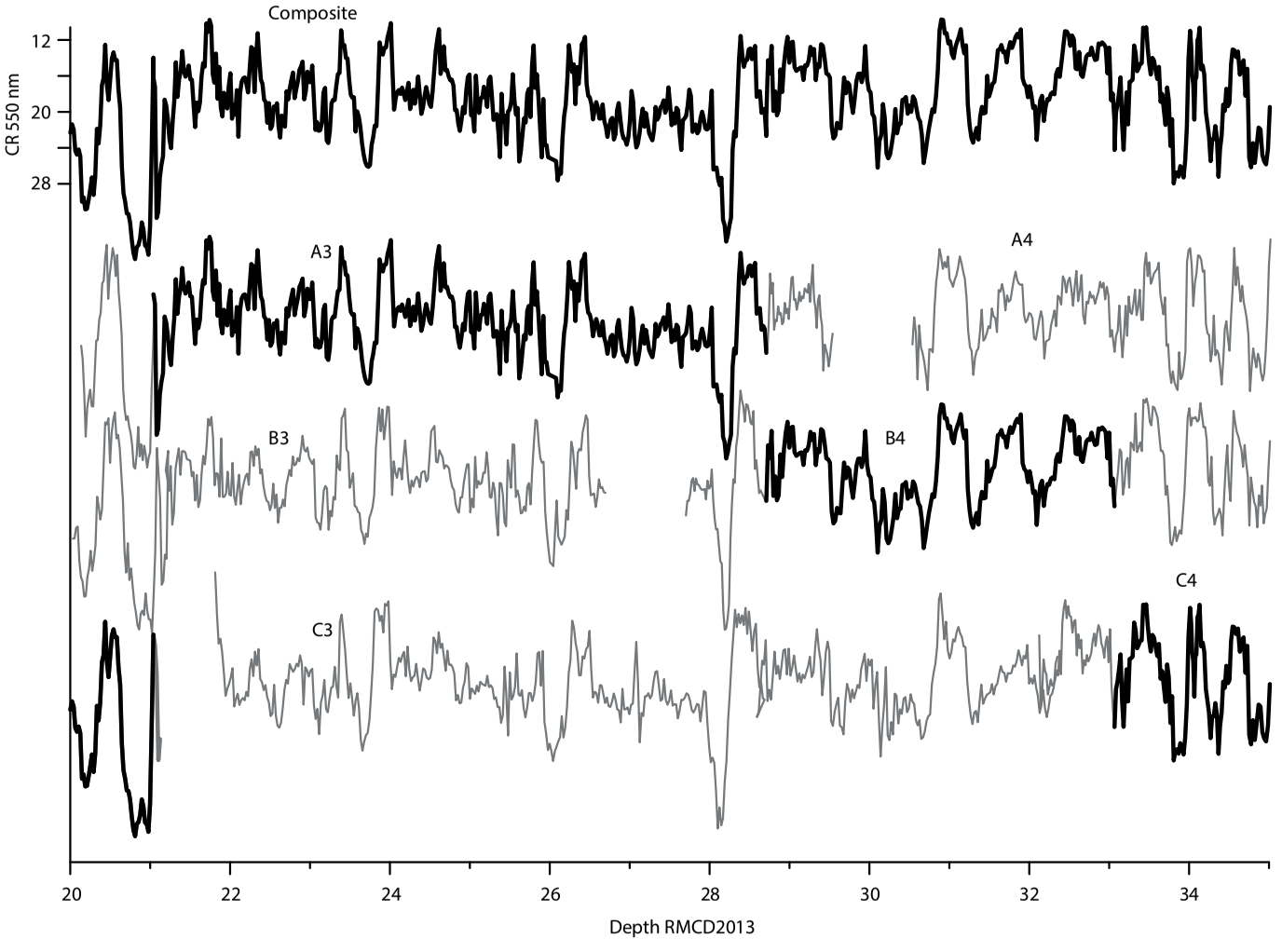
Composite
CR 550 nm
12
20
28
A3
A4
B3
B4
C3
C4
20
22
24
26
28
30
32
34
Depth RMCD2013

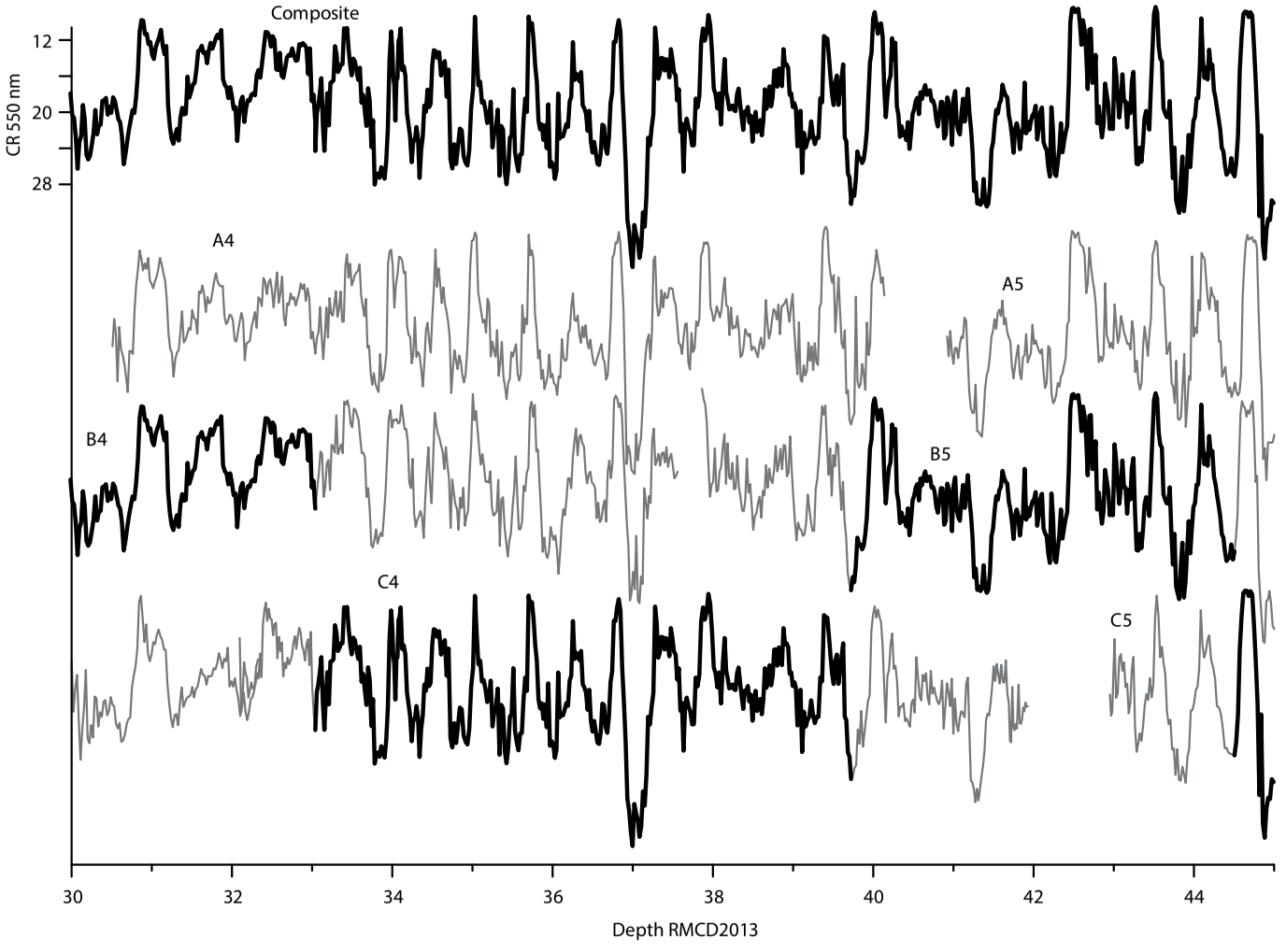
Composite
CR 550 nm
12
20
28
A4
A5
B4
B5
C4
C5
30
32
34
36
38
40
42
44
Depth RMCD2013

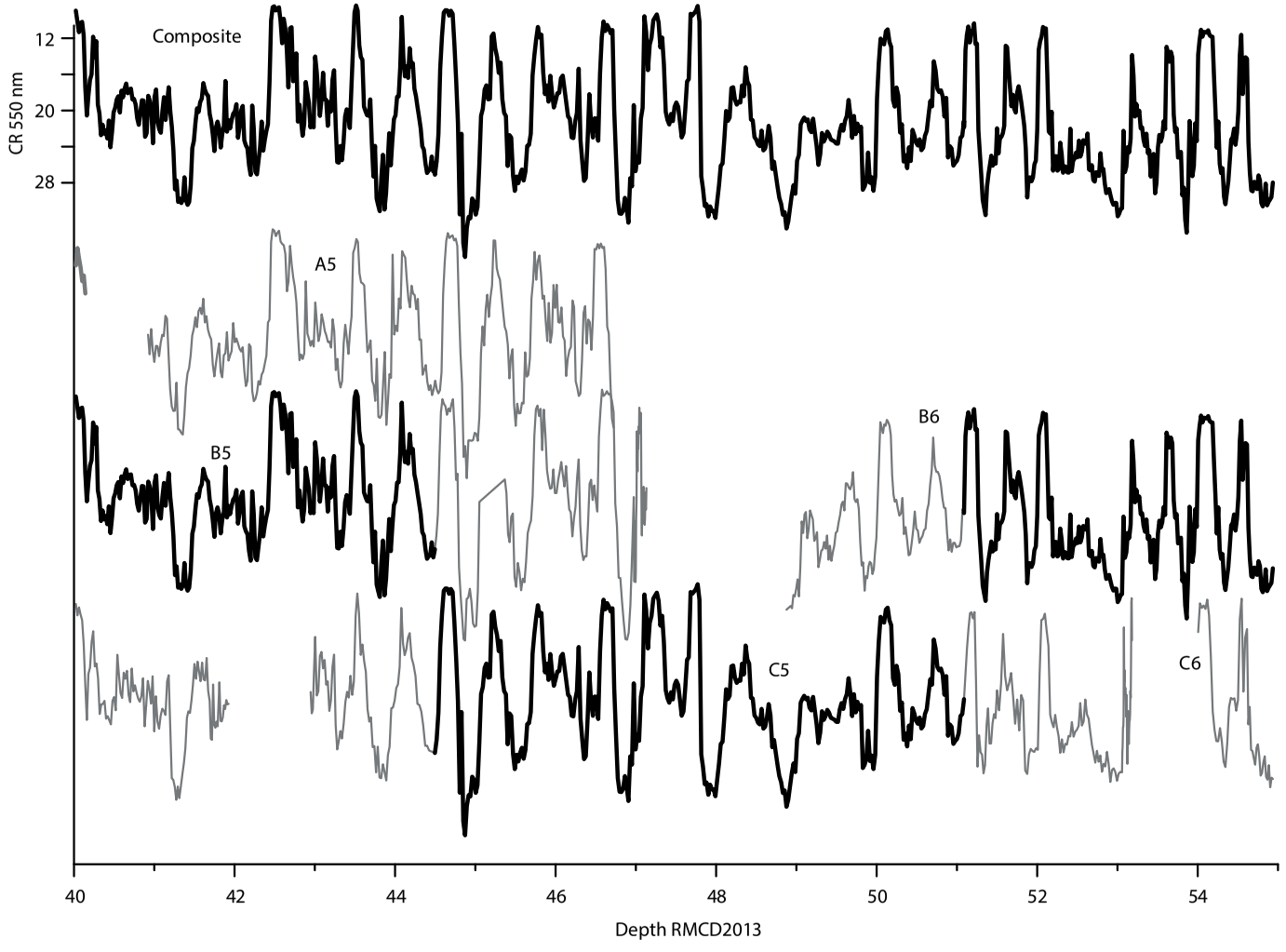
Composite
A5
B5
B6
C5
C6
CR 550 nm
12
20
28
40
42
44
46
48
50
52
54
Depth RMCD2013

Appendix II

Table of the ODP Site 967 splice, adapted from Sakamoto et al. (1998)

site	hole	core	type	section	top	mbsf	rmcd2013
967	D	1	H	1	2	0.02	0.020
967	D	1	H	5	6	6.06	5.915
967	A	1	H	4	144	5.94	5.915
967	A	1	H	5	138	7.38	7.382
967	B	2	H	1	108	6.38	7.382
967	B	2	H	4	44	10.24	11.324
967	C	2	H	1	16	9.66	11.324
967	C	2	H	7	52	19.02	21.039
967	A	3	H	1	100	19.80	21.039
967	A	3	H	6	114	27.44	28.699
967	B	4	H	1	114	25.44	28.699
967	B	4	H	4	58	29.38	33.050
967	C	4	H	1	106	29.56	33.050
967	C	4	H	6	10	36.10	39.722
967	B	5	H	2	38	35.68	39.722
967	B	5	H	5	74	40.54	44.497
967	C	5	H	2	2	39.52	44.497
967	C	5	H	5	148	45.48	51.097
967	B	6	H	2	114	45.94	51.097
967	B	6	H	5	94	50.24	54.949

Appendix III

tie points used to fit the composite of ODP Site 968 to the revised ODP Site 967 splice and merge the data into a continuous dataset.

968 tie points							967 tie points						
correlated feature	H	Core	T	Sec	Top (cm)	Depth (mbsf)	hole	core	type	section	top	mbsf	967-composite
-	A	1	H	1	6	0,06	D	1	H	1	68	0,68	0,68
Bottom S1	A	1	H	1	86	0,86	D	1	H	1	126	1,26	1,26
Top S3	A	1	H	4	92	5,42	D	1	H	3	118	4,18	4,18
Bottom s3	A	1	H	4	128	5,78	D	1	H	4	20	4,7	4,70
Bottom s4	A	1	H	5	94	6,94	D	1	H	4	98	5,48	5,48
Bottom s5	B	2	H	2	44	7,34	B	2	H	1	134	6,64	7,76
Precursor s5	B	2	H	2	92	7,82	B	2	H	2	2	6,82	7,94
Bottom s6	B	2	H	4	106	10,96	B	2	H	3	42	8,72	9,84
Bottom s7	B	2	H	5	102	12,42	B	2	H	4	16	9,96	11,08
bottom s8	B	2	H	6	76	13,66	C	2	H	1	68	10,18	11,88
Top s9	A	2	H	4	38	13,88	C	2	H	1	116	10,66	12,36
Top S'	A	2	H	5	128	16,28	C	2	H	2	110	12,1	13,80
Top s10	A	2	H	6	106	17,56	C	2	H	3	114	13,64	15,34
-	A	2	H	7	80	18,80	C	2	H	4	44	14,44	16,14
-	A	2	H	CC	18	18,99	C	2	H	4	56	14,56	16,26
-	A	3	H	1	72	19,22	C	2	H	5	70	16,2	17,90
-	A	3	H	1	100	19,50	C	2	H	5	92	16,42	18,12
Bottom s11	A	3	H	1	148	19,98	C	2	H	5	122	16,72	18,42
-	A	3	H	2	140	21,40	C	2	H	6	30	17,3	19,00
-	A	3	H	3	32	21,82	C	2	H	6	58	17,58	19,28
-	A	3	H	3	100	22,50	C	2	H	6	96	17,96	19,66
-	A	3	H	3	102	22,52	C	2	H	6	98	17,98	19,68
-	A	3	H	3	134	22,84	C	2	H	6	134	18,34	20,04
Top s12	A	3	H	4	20	23,20	C	2	H	7	2	18,52	20,22
Mid s12	A	3	H	4	40	23,40	C	2	H	7	22	18,72	20,42
-	A	3	H	4	104	24,04	A	3	H	1	124	20,04	20,96
-	A	3	H	4	112	24,12	A	3	H	1	130	20,1	21,02
-	A	3	H	5	44	24,94	A	3	H	2	52	20,82	21,74
-	A	3	H	5	64	25,14	A	3	H	2	68	20,98	21,90
Mid sa	A	3	H	5	94	25,44	A	3	H	2	106	21,36	22,28
-	A	3	H	6	116	27,16	A	3	H	3	102	22,82	23,74
Top sb	A	3	H	6	128	27,28	A	3	H	3	112	22,92	23,84
Bottom sb	A	3	H	6	148	27,48	A	3	H	3	128	23,08	24,00
-	A	3	H	CC	20	28,34	A	3	H	4	34	23,64	24,56

Appendix IV

Table of turbidites removed from the combined splice of ODP Site 967 and 968. Note that only Site 967 featured turbidites to be removed. This appendix includes the turbidites found in the extended record (chapter 5)

					mbsf		rmcd2013			
site	core	sect.	top	bot	top	bot	top	bot	MIS	Age (ka)
967	A3	5	17	20	24.97	25.00	26.23	26.25	17/18	709.0
967	A3	5	23	41	25.03	25.21	26.28	26.46	17/18	714.0
967	A3	5	91	99	25.71	25.80	26.96	27.05	18.1	736.9
967	A3	6	71	101	27.01	27.31	28.27	28.57	19/20	785.7
967	B4	1	131	145	25.61	25.75	28.91	29.06	20	804.7
967	B4	3	7	15	27.37	27.45	30.85	30.94	21/22	864.9
967	B4	3	109	125	28.39	28.55	31.98	32.16	23	902.2
967	B4	3	147	149	28.77	28.79	32.40	32.42	23/24	911.9
967	B4	4	3	15	28.83	28.95	32.45	32.60	23/24	915.3
967	C4	2	5	11	30.05	30.11	33.51	33.60	25	942.1
967	C4	2	62	66	30.62	30.66	34.06	34.09	25/26	960.9
967	B5	2	72	77	36.02	36.07	40.06	40.11	35/36	1186.8
967	B5	2	85	93	36.15	36.23	40.18	40.26	35/36	1192.5
967	B5	3	32	37	37.12	37.17	41.14	41.19	36/37	1225.2

Appendix V

Table of sapropel ages in the ODP 967/968 splice according to the Ti/Al age model. This is an extended version of table 2.3, which includes the data of chapter 5.

Emeis et al. (2000)				Lourens (2004)															
Sapropel[1] no. in 967	Type	i-cycle[1]	Age[1] (ka)	ODP 964[1,2] code	KC01(B)[2] code	i-cycle[2]	Age[2] (ka)	Composite 967-968[3] code.	Site	Hole	Core	sect.	top	bot	midpoint mbsf	midpoint[a] rmcd	midpoint[3,a] age	i-cycle[3]
1	SAP	2	8	SAP 1	S1	2	8.5	s1	968	A	1	1	64	84	0.74	1.18	8.3	2
*	red INTERVALS	4	35	-	-	-	-	n.i.	968	-	-	-	-	-	-	-	-	-
a	GHOST?	6	55	-	-	-	-	n.i.	968	-	-	-	-	-	-	-	-	-
2	SAP	8	81	X	S3	8	81	s3	968	A	1	4	92	109	5.50	4.30	80.6	8
3	SAP	10	102	SAP 2	S4	10	101	s4	968	A	1	5	52	58	6.55	5.22	101.8	10
4	SAP	10	102	-	-	-	-	s4 precursor	968	A	1	5	76	84	6.80	5.39	107.8	10
5	SAP	12	124	SAP 3	S5	12	124	s5	968	B	2	2	4	44	7.14	7.54	125.5	12
*	red INTERVALS	14	148	-	-	-	-	n.i.	968	-	-	-	-	-	-	-	-	-
6	SAP	16	172	SAP4	S6	16	172	s6	968	B	2	4	32	104	10.74	9.72	172.0	16
7	SAP	18	195	SAP5	S7	18	195	s7	968	B	2	5	52	102	12.16	10.88	195.2	18
8	SAP	20	217	SAP6	S8	20	216	s8	968	B	2	6	10	76	13.33	11.68	216.8	20
9	SAP	22	240	SAP7	S9	22	239	s9	968	A	2	4	40	51	13.96	12.41	239.7	22
*	red INTERVALS	24	262	-	-	-	-	n.i.	968	-	-	-	-	-	-	-	-	-
*	red INTERVALS	26	288	Y	S'	26	288	s'	968	A	2	5	108	132	16.20	13.77	287.5	26
*	red INTERVALS	28	310	-	-	-	-	n.i.	968	-	-	-	-	-	-	-	-	-
10	SAP	30	331	Z	S10	30	331	s10	968	A	2	6	108	113	17.61	15.38	332.3	30
*	red INTERVALS	34	369	-	-	-	-	s[*1]	967	C	2	4	102	-	15.03	16.90	375.8	34
b	SAP	38	407	SAP8	S11	38	407	s[b]	968	A	3	1	136	149	19.94	18.32	418.9	40
11	SAP	44	461	SAP9	S12	48	502	s11	968	A	3	4	32	52	23.42	20.47	504.5	48
12	SAP	46	483	-	-	-	-	s12	968	A	3	4	130	10	24.40	21.31	527.9	50
13	SAP	48	503	SAP10	Sa	52	553	s13	968	A	3	5	30	46	24.88	21.72	538	*
*	red INTERVALS	50	529	-	-	-	-	s[*2]	968	A	3	5	100	-	25.50	22.26	556.9	52
*	red INTERVALS	52	553	-	-	-	-	s[*3]	968	A	3	6	4	-	26.04	22.73	577.3	54
14	SAP	54	575	SAP11	S*	56	596	s14	968	A	3	6	72	83	26.76	23.36	596.8	56
15	SAP	56	597	SAP12	Sb	58	618	s15	968	A	3	6	126	148	27.37	23.96	617.3	58
c	GHOST?	58	618	-	*	-	-	s[c]	967	A	3	4	4	7	23.36	24.61	650.2	60
*	red INTERVALS	60	647	-	-	-	-	n.i.	967	-	-	-	-	-	-	-	-	-
16	SAP	62	668	-	-	-	-	s16	967	A	3	4	121	124	24.53	25.78	692.3	64
17	SAP	64	690	-	-	-	-	s17	967	A	3	5	18	40	25.09	26.34	714.0	66
*	red INTERVALS	74	785	*	*	74	784	n.i.	967	-	-	-	-	-	-	-	-	*
*	red INTERVALS	76	804	-	-	-	-	n.i.	967	-	-	-	-	-	-	-	-	-
*	red INTERVALS	78	822	-	-	-	-	n.i.	967	-	-	-	-	-	-	-	-	-

Emeis et al. (2000)				Lourens (2004)														
Sapropel[1] no. in 967	Type	i-cycle[1]	Age[1] (ka)	ODP 964[1,2] code	KC01(B)[2] code	i-cycle[2]	Age[2] (ka)	Composite 967-968[3] code.	Site	Hole	Core	sect.	top	bot	midpoint mbsf	midpoint[a] rmcd	midpoint[3,a] age	i-cycle[3]
*	red INTERVALS	80	841	-	-	-	-	n.i.	967	-	-	-	-	-	-	-	-	-
*	red INTERVALS	82	862	*	*	82	861	s*[4]	967	B	4	3	22	-	27.53	31.07	870.6	82*
*	red INTERVALS	84	882	-	-	-	-	s*[5]	967	B	4	3	90	-	28.21	31.76	892.8	*
*	red INTERVALS	86	908	-	-	-	-	s*[6]	967	B	4	4	28	-	29.09	32.73	921.1	86
18	SAP	88	934	-	-	-	-	s18	967	C	4	1	142	150	29.92	33.41	937.7	*
19	SAP	90	955	SAP13	S″	90	955	s19	967	C	4	2	50	72	30.50	33.98	957.5	*
20	SAP	92	977	SAP14	Sc	92	977	s20	967	C	4	2	110	113	31.10	34.53	377.2	92
21	SAP	94	997	SAP15	*	94	997	s21	967	C	4	3	6	9	31.50	35.04	996.4	94
22	SAP	96	1027	SAP16	*	96	1027	s22	967	C	4	3	67	74	32.17	35.71	1026.0	96
23	GHOST?	98	1048	-	*	-	-	s23	967	C	4	3	121	123	32.71	36.26	1050.3	98
24	SAP	100	1070	SAP17	Sd	100	1070	s24	967	C	4	4	21	23	33.21	36.77	1069.9	100
25	SAP	102	1091	-	*	-	-	s25	967	C	4	4	67	73	33.67	37.28	1093.3	102
26	SAP	104	1111	SAP18	*	104	1111	s26	967	C	4	4	126	138	34.26	37.95	1118.4	*
27	SAP	110	1164	-	*	-	-	s27	967	C	4	5	125	132	35.75	39.41	1166.7	110
28	SAP	112	1185	SAP19	-	112	1185	s28	967	B	5	2	62	79	35.92	40.05	1186.6	112
29	SAP	122	1280					s29	967	B	5	4	15	43	38.45	42.49	1280.7	122
30	SAP	126	1315					s30	967	B	5	4	120	127	39.50	43.51	1317.4	126
31	SAP	128	1335					s31	967	B	5	5	23	33	40.03	44.08	1337.7	128
32	SAP	130	1356					s32	967	C	5	2	16	24	39.66	44.67	1358.6	
33	SAP	132	1376					s33	967	C	5	2	65	67	40.15	45.21	1380.0	
34	SAP	134	1398					s34	967	C	5	2	115	124	40.65	45.78	1401.8	

[a]Sapropel midpoints as defined by Emeis et al. (2000), their age estimate according to the Ti/Al age model
[1]Emeis et al. (2000)
[2]Lourens, 2004; retuning of KC01B, ODP 964, KC01
[3]Ziegler et al. (2010); this study
n.i.: not identified

References

Astraldi, M., Gasparini, G., Vetrano, A., and Vignudelli, S., 2002. Hydrographic characteristics and interannual variability of water masses in the central mediterranean: A sensitivity test for long-term changes in the mediterranean sea. *Deep Sea Research Part I: Oceanographic Research Papers* 49, 661-680.

Bard, E., Hamelin, B., and Fairbanks, R.G., 1990. U-Th ages obtained by mass spectrometry in corals from Barbados: Sea level during the past 130, 000 years. *Nature* 346, 456-458.

Bard, E., Rostek, F., Turon, J.L., and Gendreau, S., 2000. Hydrological impact of Heinrich events in the subtropical northeast Atlantic. *Science* 289, 1321-1324.

Bar-Matthews, M., Ayalon, A., Gilmour, M., Matthews, A., and Hawkesworth, C.J., 2003. Sea – land oxygen isotopic relationships from planktonic foraminifera and speleothems in the eastern Mediterranean region and their implication for paleorainfall during interglacial intervals. *Geochimica Et Cosmochimica Acta* 67, 3181-3199.

Bazin, L., Landais, A., Lemieux-Dudon, B., Toyé Mahamadou Kele, H., Veres, D., Parrenin, F., Martinerie, P., Ritz, C., Capron, E., and Lipenkov, V., 2013. An optimized multi-proxy, multi-site antarctic ice and gas orbital chronology (AICC2012): 120-800 ka. *Climate of the Past* 9, 1715-1731.

Berger, A. 1978. Long-term variations of daily insolation and Quaternary climatic changes. *Journal of the Atmospheric Sciences* 35(12), 2362-2367.

Bintanja, R., van de Wal, R.S.W. and Oerlemans, J., 2005. Modelled atmospheric temperatures and global sea levels over the past million years. *Nature* 437, 125-128.

Blunier, T., Chappellaz, J., Schwander, J., Stauffer, B. and Raynaud, D., 1995. Variations in atmospheric methane concentration during the Holocene epoch. Nature 374, 46-49.

Boaretto, E., Mienis, H. K., and Sivan, D., 2010. Reservoir age based on pre-bomb shells from the intertidal zone along the coast of Israel, *Nuclear Instruments and Methods in Physics Research section B* 268, 966 – 968.

Bosmans, J. H. C., 2014. A model perspective on orbital forcing of monsoons and Mediterranean climate using ECEarth. *Utrecht Studies in Earth Sciences* 055, Utrecht.

Braconnot, P., Otto-Bliesner, B., Harrison, S., Joussaume, S., Peterchmitt, J.-Y., Abe-Ouchi, A., Crucifix, M., Driesschaert, E., Fichefet, Th., Hewitt, C. D., Kageyama, M., Kitoh, A., Laîné, A., Loutre, M.-F., Marti, O., Merkel, U., Ramstein, G., Valdes, P., Weber, S. L., Yu, Y., and Zhao, Y. 2007. Results of PMIP2 coupled simulations of the Mid-Holocene and Last Glacial Maximum – Part 1: experiments and large-scale features, *Climate of the Past* 3, 261-277.

Brovkin V, Ganopolski, A., Svirezhev, Y., 1997. A continuous climate-vegetation classification for use in climate-biosphere studies. *Ecological Modeling* 101, 251-261.

Cacho, I., Grimalt, J.O., Pelejero, C., Canals, M., Sierro, F.J., Flores, J.A., and Shackleton, N., 1999. Dansgaard-Oeschger and Heinrich event imprints in Alboran Sea paleotemperatures. *Paleoceanography* 14, 698-705.

Cao, M., Marshall, S. and Gregson, K., 1996. Global carbon exchange and methane emissions from natural wetlands: Application of a process-based model, *Journal of Geophysical Research* 101, 14,399-14,414.

Carlson, A.E. and Clark, P.U., 2012. Ice sheet sources of sea level rise and freshwater discharge during the last deglaciation. *Reviews of Geophysics* 50.

Chappellaz, J., Barnola, J.M., Raynaud, D., Korotkevich, Y.S. and Lorius, C., 1990. Ice-core record of atmospheric methane over the past 160,000 years, *Nature* 345, 127-131.

Chappellaz, J. A., Fung, I. Y. and Thompson, A.M., 1993. The atmospheric CH_4 increase since the Last Glacial Maximum: 1. Source estimates, *Tellus B* 45, 228-241.

Chen, Y. and Prinn, R.G., 2006. Estimation of atmospheric methane emissions between 1996 and 2001 using a three-dimensional global chemical transport model, *Journal of Geophysical Research* 111.

Cheng, H., Edwards, R.L., Broecker, W.S., Denton, G.H., Kong, X., Wang, Y., Zhang, R., and Wang, X., 2009. Ice age terminations. *Science* 326, 248-252.

Christensen, T. R., Ekberg, A., Strom, L., Mastepanov, M., Panikov, N., Oquist, M., Svenson, B.H., Nykanen, H., Martikainen, P.J. and Oskarsson, H., 2003. Factors controlling large scale variations in methane emissions from wetlands, *Geophysical Research Letters* 30.

Clark, P.U., Archer, D., Pollard, D., Blum, J.D., Rial, J.A., Brovkin, V., Mix, A.C., Pisias, N.G., and Roy, M., 2006. The middle pleistocene transition: Characteristics. mechanisms, and implications for long-term changes in atmospheric PCO_2. *Quaternary Science Reviews* 25, 3150-3184.

Claussen, M., Bathiany, S., Brovkin, V., and Kleinen, T., 2013. Simulated climate-vegetation interaction in semi-arid regions affected by plant diversity. *Nature Geoscience* 6, 954-958.

Clemens, S.C., Prell, W.L., and Sun, Y., 2010. Orbital-scale timing and mechanisms driving Late Pleistocene Indo-Asian summer monsoons: reinterpreting cave speleotherm $\delta^{18}O$, *Paleoceanography* 25,

Crowley, T.J., 1991. Ice-age methane variations. *Nature* 353, 122-123.

De Lange, G.J., Thomson, J., Reitz, A., Slomp, C.P., Principato, M.S., Erba, E., and Corselli, C., 2008. Synchronous basin-wide formation and redox-controlled preservation of a mediterranean sapropel. *Nature Geoscience* 1, 606-610.

Denman, K.L., et al., Couplings Between Changes in the Climate System and Biogeochemistry. In: Climate Change 2007: The Physical Science Basis. Contribution of Working Group I to the Fourth Assessment Report of the Intergovernmental Panel on Climate Change [Solomon, S., et al.]. Cambridge University Press, Cambridge, United Kingdom and New York, NY, USA, 2007

Dreyfus, G., Parrenin, F., Lemieux-Dudon, B., Durand, G., Masson-Delmotte, V., Jouzel, J., Barnola, J., Panno, L., Spahni, R., and Tisserand, A., 2007. Anomalous flow below 2700 m in the EPICA dome C ice core detected using $\delta^{18}O$ of atmospheric oxygen measurements. *Climate of the Past* 3, 341 – 353.

Dupont, L., Donner, B., Schneider, R., and Wefer, G., 2001. Mid-Pleistocene environmental change in tropical Africa began as early as 1.05 ma. *Geology* 29, 195-198.

Dutton, A., Bard, E., Antonioli, F., Esat, T.M., Lambeck, K., and McCulloch, M.T., 2009. Phasing and amplitude of sea-level and climate change during the penultimate interglacial. *Nature Geoscience* 2, 355-359.

Ehrmann, W., Seidel, M., Schmiedl, G., 2013. Dynamics of Late Quaternary North African humid periods documented in the clay mineral record of central Aegean Sea sediments. *Global and Planetary Change* 107, 186-195.

Elderfield, H., Ferretti, P., Greaves, M., Crowhurst, S., McCave, I. N., Hodell, D., and Piotrowski, A. M. 2012. Evolution of ocean temperature and ice volume through the Mid-Pleistocene climate transition. *Science* 337, 704-709.

Emeis, K.C., Robertson, A., and Richter, C., 1996. paleoceanography and sapropel introduction. *Proceedings of the Ocean Drilling Program, Initial Reports*. ODP, College Station (TX).

Emeis, K., Sakamoto, T., Wehausen, R., and Brumsack, H., 2000. The sapropel record of the eastern mediterranean sea – results of ocean drilling program leg 160. *Palaeogeography, Palaeoclimatology, Palaeoecology* 158, 371-395.

Emiliani, C. 1955. Pleistocene temperatures. *The Journal of Geology*, 538-578.

Epstein, S., Buchsbaum, R., Lowenstam, H., and Urey, H. C., 1951. Carbonate-water isotopic temperature scale. *Geological Society of America Bulletin*, 62, 417-426.

Fischer, H., Behrens, M., Bock, M., Richter, U., Schmitt, J., Loulergue, L., Chappellaz, J., Spahni, R., Blunier, T., Leuenberger, M., and Stocker, T.F., 2008. Changing boreal methane sources and constant biomass burning during the last termination, *Nature* 452, 864-867.

Fontugne, M. and Calvert, S., 1992. Late Pleistocene variability of the carbon isotopic composition of organic matter in the eastern Mediterranean: Monitor of changes in carbon sources and atmospheric CO_2 concentrations. *Paleoceanography* 7, 1-20.

Fung, I., John, J., Lerner, J., Matthews, E., Prather, M., Steele, L., and Fraser, P., 1991. Three Dimensional Model Synthesis of the Global Methane Cycle, *Journal of Geophysical Research* 96, 13,033-13,065

Gedney, N., Cox, P.M., Huntingford, C., 2004. Climate feedback from wetland methane emissions, *Geophysical Research Letters* 31.

Gherardi, J., Labeyrie, L., Nave, S., Francois, R., McManus, J.F., and Cortijo, E., 2009. Glacial-interglacial circulation changes inferred from $^{231}Pa/^{230}Th$ sedimentary record in the North Atlantic region. *Paleoceanography* 24.

Gradstein, F. M., Ogg, J. G., Smith, A. G., Bleeker, W., and Lourens, L. J. 2004. A new geologic time scale, with special reference to Precambrian and Neogene. *Episodes* 27, 83-100.

Grant, K., Rohling, E., Bar-Matthews, M., Ayalon, A., Medina-Elizalde, M., Ramsey, C.B., Satow, C., and Roberts, A., 2012. Rapid coupling between ice volume and polar temperature over the past 150,000 years. *Nature* 491, 744-747.

Grant, K., Rohling, E., Ramsey, C.B., Cheng, H., Edwards, R., Florindo, F., Heslop, D., Marra, F., Roberts, A., and Tamisiea, M., 2014. Sea-level variability over five glacial cycles. *Nature Communications* 5.

Grossman, E.L. and Ku, T., 1986. Oxygen and carbon isotope fractionation in biogenic aragonite: Temperature effects. *Chemical Geology: Isotope Geoscience Section* 59, 59-74.

Harmon, R.S., Schwarcz, H.P., and Ford, D.C., 1978. Late Pleistocene sea level history of Bermuda. *Quaternary Research* 9, 205-218.

Hays, J. D., Imbrie, J., and Shackleton, N. J., 1976. Variations in the Earth's orbit: Pacemaker of the ice ages. *Science* 194, no. 4270 pp. 1121-1132

Hennekam, R., and G. De Lange (2012), X-ray fluorescence core scanning of wet marine sediments: Methods to improve quality and reproducibility of high-resolution paleoenvironmental records, *Limnology and Oceanography: Methods* 10, 991 – 1003.

Hennekam, R., Jilbert, T., Schnetger, B., and Lange, G.J., 2014. Solar forcing of Nile discharge and sapropel S1 formation in the early to middle Holocene eastern Mediterranean. *Paleoceanography* 29, 343-356.

Hilgen, F. 1991. Astronomical calibration of Gauss to Matuyama sapropels in the Mediterranean and implication for the geomagnetic polarity time scale. *Earth and Planetary Science Letters*, 104, 226-244.

Hilgen, F., Lourens, L., Berger, A., Loutre, M.F., 1993. Evaluation of the astronomically calibrated time scale for the late Pliocene and earliest Pleistocene. *Paleoceanography*, 8, 549-565.

Hodell, D.A., Channell, J.E., Curtis, J.H., Romero, O.E., and Röhl, U., 2008. Onset of "Hudson strait" Heinrich events in the eastern North Atlantic at the end of the middle Pleistocene transition (640 ka)? *Paleoceanography* 23.

Hooghiemstra, H., Melice, J.L., Berger, A., Shackleton, N.J., 1993. Frequency spectra and paleoclimatic variability of the high-resolution 30-1450 ka Funza I pollen record (Eastern Cordillera, Colombia), *Quaternary Science Reviews* 12, pp. 141-156.

Houweling, S., Dentener, F. and Lelieveld, J., 2000. Simulation of preindustrial atmospheric methane to constrain the global source strength of natural wetlands, *Journal of Geophysical Research* 105, 243-255.

Huybers, P., 2007. Glacial variability over the last two million years: An extended depth-derived age model, continuous obliquity pacing, and the Pleistocene progression. *Quaternary Science Reviews* 26, 37-55.

Huybers, P., 2011. Combined obliquity and precession pacing of Late Pleistocene deglaciations. *Nature* 480, 229-232.

Huybers, P. and Aharonson, O., 2010. Orbital tuning, eccentricity, and the frequency modulation of climatic precession. *Paleoceanography* 25.

Huybers, P. and Wunsch, C., 2004. A depth-derived Pleistocene age model: Uncertainty estimates, sedimentation variability, and nonlinear climate change. *Paleoceanography* 19.

Imbrie, J. and Imbrie, J.Z., 1980. Modeling the climatic response to orbital variations. *Science* 207, 943-953.

Imbrie, J., Hays, J.D., Martinson, D.G., McIntyre, A., Mix, A.C., Morley, J.J., Pisias, N.G., Prell, W. L., Shackleton, N. J., 1984. The orbital theory of Pleistocene climate: Support from a revised chronology of the marine $\delta^{18}O$ record. *Milankovitch and climate: understanding the response to astronomical forcing* Vol. 1, p. 269.

Imbrie, J., Berger, A., Boyle, E.A., Clemens, S.C., Duffy, A., Howard, W.R., Kukla, G., Kutzbach, J., Martinson, D.G., McIntyre, A., Mix, A. C., Molfino, B., Morley, J. J., Peterson, L. C., Pisias, N. G., Prell, W. L., Raymo, M. E., Shackleton, N. J., Toggweiler, J. R., 1993. On the structure and origin of major glaciation cycles 2. the 100,000-year cycle. *Paleoceanography* 8, 699-638.

Jouzel, J., Masson-Delmotte, V., Cattani, O., Dreyfus, G., Falourd, S., Hoffmann, G., Minster, B., Nouet, J., Barnola, J.M., Chappellaz, J. et al., 2007. Orbital and millennial Antarctic climate variability over the past 800,000 years. *Science* 317, 793-796.

Kaplan, J. O., 2002. Wetlands at the Last Glacial Maximum: Distribution and methane emissions, *Geophysical Research Letters* 29

Kaplan, J. O., Folberth, G. and Hauglustaine, D.A., 2006. Role of methane and biogenic volatile organic compound sources in late glacial and Holocene fluctuations of atmospheric methane concentrations, *Global Biogeochemical Cycles* 20.

Kemp, A.E., Pearce, R.B., Koizumi, I., Pike, J., and Rance, S.J., 1999. The role of mat-forming diatoms in the formation of Mediterranean sapropels. *Nature* 398, 57-61.

Kutzbach, J. E., Liu, X., Liu, Z., and Chen, G., 2008. Simulation of the evolutionary response of global summer monsoons to orbital forcing over the past 280,000 years, *Climate Dynamics* 30, 6, pp. 567-579.

Labeyrie, L., Waelbroeck, C., Cortijo, E., Michel, E., and Duplessy, J., 2005. Changes in deep water hydrology during the last deglaciation. *Comptes Rendus Geoscience* 337, 919-927.

Lambeck, K. and Chappell, J., 2001. Sea level change through the last glacial cycle. *Science* 292, 679-686.

Lang, N. and Wolff, E.W., 2011. Interglacial and glacial variability from the last 800 ka in marine, ice and terrestrial archives. *Climate of the Past* 7, 361 – 380.

Langereis, C., Dekkers, M., de Lange, G.J., Paterne, M., Sandvoort, P.J.M., 1997. Magnetostratigraphy and astronomical calibration of the last 1.1 Myr from an eastern Mediterranean piston core and dating of short events in the Brunhes. *Geophysical Journal International* 129, 75-94.

Larrasoana, J., Roberts, A., Rohling, E., Winklhofer, M., and Wehausen, R., 2003. Three million years of monsoon variability over the northern Sahara. *Climate Dynamics* 21, 689-698.

Larrasoaña, J. C., Roberts, A. P., and Rohling, E. J. 2013. Dynamics of green Sahara periods and their role in hominin evolution. *PloS one* 8.

Lascaratos, A., Roether, W., Nittis, K., and Klein, B., 1999. Recent changes in deep water formation and spreading in the eastern Mediterranean Sea: A review. *Progress in Oceanography* 44, 5-36.

Laskar, J., 1990. The chaotic motion of the solar system: A numerical estimate of the size of the chaotic zones. *Icarus* 88, 266-291.

Laskar, J., Joutel, F., and Boudin, F., 1993. Orbital, precessional, and insolation quantities for the earth from -20 MYR to 10 MYR. *Astronomy and Astrophysics* 270, 522-533.

Laskar, J., Robutel, P., Joutel, F., Gastineau, M., Correia, A. C. M., and Levrard, B. 2004. A long-term numerical solution for the insolation quantities of the Earth. *Astronomy and Astrophysics* 428, 261-285.

Lelieveld, J., Crutzen, P. and Dentener, F. J., 1998. Changing concentration, lifetime and climate forcing of atmospheric methane. *Tellus 50B*, 128-150.

Lemieux-Dudon, B., Blayo, E., Petit, J., Waelbroeck, C., Svensson, A., Ritz, C., Barnola, J., Narcisi, B.M., and Parrenin, F., 2010. Consistent dating for Antarctic and Greenland ice cores. *Quaternary Science Reviews* 29, 8-20.

Lisiecki, L. E., and Lisiecki, P. A., 2002. Application of dynamic programming to the correlation of paleoclimate records, *Paleoceanography* 17

Lisiecki, L.E. and Raymo, M.E., 2005. A Pliocene-Pleistocene stack of 57 globally distributed benthic $\delta^{18}O$ records. *Paleoceanography* 20.

Lisiecki, L.E. and Raymo, M.E., 2009. Diachronous benthic $\delta^{18}O$ responses during late pleistocene terminations. *Paleoceanography* 24.

Loulergue, L., Schilt, A., Spahni, R., Masson-Delmotte, V., Blunier, T., Lemieux, B., … & Chappellaz, J. 2008. Orbital and millennial-scale features of atmospheric CH_4 over the past 800,000 years. *Nature* 453, 383-386.

Lourens, L. J. 2004. Revised tuning of Ocean Drilling Program Site 964 and KC01B (Mediterranean) and implications for the $\delta^{18}O$, tephra, calcareous nannofossil, and geomagnetic reversal chronologies of the past 1.1 Myr. *Paleoceanography* 19.

Lourens, L.J., Reichart G.-J., 1996. G. Low-latitude forcing of glacial cycles. G.-J.Reichart (PhD thesis), *Geologica Utraiectina* 154, 153-168.

Lourens, L. J., Antonarakou, A.,Hilgen, F.J., van Hoof, A.A.M., Vergnaud-Grazzini, C., Zachariasse, W.J., 1996. Evaluation of the Plio-Pleistocene astronomical timescale. *Paleoceanography* 11, 391-413.

Lourens, L. J., Wehausen, R., and Brumsack, H. J., 2001. Geological constraints on tidal dissipation and dynamical ellipticity of the Earth over the past three million years. *Nature* 409, 029-1033.

Lourens, L.J., Becker, J., Bintanja, R., Hilgen, F.J., Tuenter, E., van de Wal, R.S.W., and Ziegler, M., 2010. Linear and non-linear response of Late Neogene glacial cycles to obliquity forcing and implications for the Milankovitch theory. *Quaternary Science Reviews* 29, 352-365.

Lüthi, D., Le Floch, M., Bereiter, B., Blunier, T., Barnola, J. M., Siegenthaler, U., … and Stocker, T. F 2008. High-resolution carbon dioxide concentration record 650,000-800,000 years before present, *Nature* 453, 379-382.

Mariotti, A., Struglia, M. V. Zeng, N., and Lau, K. M. 2002. The hydrological cycle in the Mediterranean region and implications for the water budget of the Mediterranean Sea. *Journal of climate* 15, 1674-1690.

Martrat, B., Grimalt, J.O., Lopez-Martinez, C., Cacho, I., Sierro, F.J., Flores, J.A., Zahn, R., Canals, M., Curtis, J.H., and Hodell, D.A., 2004. Abrupt temperature changes in the Western Mediterranean over the past 250,000 years. *Science* 306, 1762-1765.

Maslin, M.A. and Ridgewell, A.J., 2005. Mid-Pleistocene revolution and the 'eccentricity myth'. Geological Society, London, *Special Publications* 247, 19-34.

Mercone, D., Thomson, J., Croudace, I., Siani, G., Paterne, M., and Troelstra, S., 2000. Duration of S1, the most recent sapropel in the eastern Mediterranean Sea, as indicated by accelerator mass spectrometry radiocarbon and geochemical evidence. *Paleoceanography* 15, 336-347.

Milanković, M., 1930. Mathematische klimalehre und astronomische theorie der klimaschwankungen. Borntraeger.

Mix, A. C., Pisias, N. G., Rugh, W., Wilson, J., Morey, A., and Hagelberg, T. K., 1995. Benthic foraminifer stable isotope record from Site 849 (0-5 Ma): local and global climate changes. *Proceedings of the Ocean Drilling Program, Scientific Results*, College Station (TX).

Mudelsee, M. and Schulz, M., 1997. The mid-Pleistocene climate transition: Onset of 100 ka cycle lags ice volume build-up by 280 ka. *Earth and Planetary Science Letters* 151, 117-123.

Mudelsee, M. and Stattegger, K., 1997. Exploring the structure of the mid-Pleistocene revolution with advanced methods of time-series analysis. *Geologische Rundschau* 86, 499-511.

Nittis, K., and Lascaratos, A., 1998. Diagnostic and prognostic numerical studies of LIW formation. *Journal of marine systems* 18, 179-195.

Paillard, D. 2001. Glacial cycles: toward a new paradigm. *Reviews of Geophysics* 39, 325-346.

Paillard, D., Labeyrie, L., and Yiou, P., 1996. Macintosh program performs time-series analysis. *Eos Transactions Americal Geophysical Union* 77, 379.

Parrenin, F., and Paillard, D., 2012. Terminations VI and VIII (~530 and ~720 kyr BP) tell us the importance of obliquity and precession in the triggering of deglaciations. *Climate of the Past* 8, 2031-2037.

Parrenin, F., Barnola, J., Beer, J., Blunier, T., Castellano, E., Chappellaz, J., Dreyfus, G., Fischer, H., Fujita, S., and Jouzel, J., 2007. The EDC3 chronology for the EPICA dome C ice core. *Climate of the Past* 3, 485-497.

Peltier, W. R., 2004. Global glacial isostasy and the surface of the ice-age Earth: The ICE-5G (VM2) model and GRACE, *Annual Review of Earth and Planetary Sciences* 32, 111-149.

Petoukhov, V., Ganopolski, A., Brovkin, V., Claussen, M., Eliseev, A., Kubatzki, C. and Rahmstorf, S., 2000. CLIMBER-2: a climate system model of intermediate complexity, Part I: model description and performance for present climate, *Climate Dynamics* 16, 1-17

Pisias, N.G. and Rea, D.K., 1988. Late Pleistocene paleoclimatology of the central equatorial Pacific: Sea surface response to the southeast trade winds. *Paleoceanography* 3, 21-37.

Postma, G., Hilgen, F.J., Zachariasse, W.J., 1993. Precession-punctuated growth of a late Miocene submarine-fan lobe on Gavdos (Greece). *Terra Nova* 5, 438-444.

Prigent, C., Papa, F., Aires, F., Rossow, W.B. and Matthews, E., 2007. Global inundation dynamics inferred from multiple satellite observations, 1993-2000, *Journal of Geophysical Research* 112,

Ramage, C. 1971, Monsoon Meteorology. *International Geophysics Series* Vol. 15, 296 p., Academic Press, San Diego, California.

Ramsey, C.B., 2009. Bayesian analysis of radiocarbon dates. *Radiocarbon* 51, 337-360.

Raymo, M., 1997. The timing of major climate terminations. *Paleoceanography* 12, 577-585.

Reimer, P. J., and F. G. McCormac (2002), Marine radiocarbon reservoir corrections for the Mediterranean and Aegean Seas, *Radiocarbon* 44, 159 – 166.

Reimer, P.J., Baillie, M.G., Bard, E., Bayliss, A., Beck, J.W., Blackwell, P.G., Bronk, R.C., Buck, C.E., Burr, G.S., and Edwards, R.L., 2009. IntCal09 and Marine09 radiocarbon age calibration curves, 0-50,000 years cal BP, *Radiocarbon* 51, 1111 – 1150.

Rial, J. and Anaclerio, C., 2000. Understanding nonlinear responses of the climate system to orbital forcing. *Quaternary Science Reviews* 19, 1709-1722.

Rice, A.L., Butenhoff, C.L., Shearer, M.J., Teama, D., Rosenstiel, T.N. and Khalil, M.A.K., 2010. Emissions of anaerobically produced methane by trees, *Geophysical Research Letters* 37.

Robinson, A.R., Malanotte-Rizzoli, P., Hecht, A., Michelato, A., Roether, W., Theocharis, A., Ünlüata, Ü., Pinardi, N., Artegiani, A., and Bergamasco, A., 1992. General circulation of the eastern Mediterranean. *Earth-Science Reviews* 32, 285-309.

Rohling, E. J. 1994. Review and new aspects concerning the formation of eastern Mediterranean sapropels. *Marine Geology* 122, 1-28.

Rohling, E.J., 1999. Environmental control on Mediterranean salinity and $\delta^{18}O$. *Paleoceanography* 14, 706-715.

Rohling, E., Jorissen, F., and De Stigter, H., 1997. 200 year interruption of Holocene sapropel formation in the Adriatic sea. *Journal of Micropalaeontology* 16, 97-108.

Rohling, E., Grant, K., Bolshaw, M., Roberts, A., Siddall, M., Hemleben, C., and Kucera, M., 2009. Antarctic temperature and global sea level closely coupled over the past five glacial cycles. *Nature Geoscience* 2, 500-504.

Rohling, E.J., Foster, G.L., Grant, K.M., Marino, G., Roberts, A.P., Tamisiea, M.E., and Williams, F., 2014. Sea-level and deep-sea-temperature variability over the past 5.3 million years. *Nature* 508, 477-482.

Rohling, E.J., Marino, G., and Grant, K.M. 2015. Mediterranean climate and oceanography, and the periodic development of anoxic events (sapropels). *Earth Science Reviews* 143, 62 – 97.

Rossignol-Strick, M., 1983. African monsoons, an immediate climate response to orbital insolation. *Nature* 304, 46-49.

Rossignol-Strick, M., 1985. Mediterranean Quaternary sapropels, an immediate response of the African monsoon to variation of insolation. *Palaeogeography, Palaeoclimatology, Palaeoecology* 49, 237-263.

Rossignol-Strick, M., 1999. The Holocene climatic optimum and pollen records of sapropel 1 in the eastern Mediterranean, 9000 – 6000BP. *Quaternary Science Reviews* 18, 515-530.

Rossignol-Strick, M. and Paterne, M., 1997. A synthetic pollen record of the eastern Mediterranean sapropels of the last 1 Ma: implications for the time-scale and formation of sapropels. *Marine Geology* 153, 221 – 237

Rossignol-Strick, M., Paterne, M., Bassinot, F., Emeis, K., and De Lange, G., 1998. An unusual mid-Pleistocene monsoon period over Africa and Asia. *Nature* 392, 269-272.

Ruddiman, W.F. and Raymo, M.E., 2003. A methane-based time scale for Vostok ice, *Quaternary Science Reviews* 22, 141-155.

Sakamoto, T., Janecek, T., Emeis, K.-C., 1998. Continuous sedimentary sequences from the eastern Mediterranean Sea: composite depth sections. *Proceedings of the Ocean Drilling Program.Scientific results* 160, 37-59.

Schmidt, G.A., Shindell, D.T. and Harder, S., 2004. A note on the relationship between ice core methane concentrations and insolation, *Geophysical Research Letters* 31.

Schneider von Deimling, T., Held, H., Ganopolski, A., Rahmstorf, S., 2006. Climate sensitivity estimated from ensemble simulations of glacial climate, *Climate Dynamics* 27, 149-163.

Schrag, D. P., and DePaolo, D. J. 1993. Determination of $\delta^{18}O$ of seawater in the deep ocean during the Last Glacial Maximum. *Paleoceanography* 8, 1-6.

Segers, R., 1998. Methane production and methane consumption: a review of processes underlying wetland methane fluxes, *Biogeochemistry* 41, 23-51,

Shackleton, N., 1987. Oxygen isotopes, ice volume and sea level. *Quaternary Science Reviews* 6, 183-190.

Shackleton, N. J., 1995. New data on the evolution of Pliocene climate variability, in Paleoclimate and Evolution, With Emphasis on Human Origins, edited by E. S. Vrba et al., pp. 242 – 248, Yale Univ. Press, New Haven, Ct.

Shackleton, N. J., and Opdyke, N. D., 1973. Oxygen isotope and palaeomagnetic stratigraphy of equatorial Pacific core V28-238: Oxygen isotope temperatures and ice volumes on a 105 year and 106 year scale. *Quaternary research* 3, 39-55.

Shackleton, N., Berger, A., and Peltier, W., 1990. An alternative astronomical calibration of the Lower Pleistocene timescale based on ODP site 677. *Transactions of the Royal Society of Edinburgh: Earth Sciences* 81, 251-261.

Siddall, M., Rohling, E.J., Almogi-Labin, A., Hemleben, C., Meischner, D., Schmelzer, I., and Smeed, D., 2003. Sea-level fluctuations during the last glacial cycle. *Nature* 423, 853-858.

Skinner, L. and Shackleton, N., 2005. An Atlantic lead over Pacific deep-water change across termination I: Implications for the application of the marine isotope stage stratigraphy. *Quaternary Science Reviews* 24, 571-580.

Skinner, L., Shackleton, N., and Elderfield, H., 2003. Millennial-scale variability of deep-water temperature and δ^{18}Odw indicating deep-water source variations in the northeast Atlantic, 0 – 34 cal. ka BP. *Geochemistry, Geophysics, Geosystems* 4.

Spahni, R., Chappellaz, J., Stocker, T. F., Loulergue, L., Hausammann, G., Kawamura, K., Flückiger, J., Schwander, J., Raynaud, D., Masson-Delmotte, V., and Jouzel, J. 2005. Atmospheric methane and nitrous oxide of the late Pleistocene from Antarctic ice cores. *Science* 310, 1317-1321.

Stern, J.V. and Lisiecki, L.E., 2014. Termination 1 timing in radiocarbon-dated regional benthic δ^{18}O stacks. *Paleoceanography*.

Thomson, J., Higgs, N., Wilson, T., Croudace, I., De Lange, G., and Van Santvoort, P., 1995. Redistribution and geochemical behaviour of redox-sensitive elements around S1, the most recent eastern mediterranean sapropel. *Geochimica Et Cosmochimica Acta* 59, 3487-3501.

Tiedemann, R., Sarnthein, M., and Shackleton, N.J., 1994. Astronomic timescale for the Pliocene Atlantic δ^{18}O and dust flux records of ocean drilling program site 659. *Paleoceanography* 9, 619-638.

Torrence, C. and Compo, G.P., 1998. A practical guide to wavelet analysis. *Bulletin of the American Meteorological Society* 79, 61-78.

Tsukada, M., Late Pleistocene vegetation and climate in Taiwan (Formosa), *Proceedings of the National Academy of Sciences of the United States of America* 55, pp. 543-548, 1966

Tzedakis, P., 2007. Seven ambiguities in the Mediterranean palaeoenvironmental narrative. *Quaternary Science Reviews* 26, 2042-2066.

Tzedakis, P.C., Palike, H., Roucoux, K.H., de Abreu, L., 2009. Atmospheric methane, southern European vegetation and low-mid latitude links on orbital and millennial timescales, *Earth Planetary Science Letters* 277, 3-4, pp. 307-317.

Valdes, P.J., Beerling, D.J. and Johnson, C.E., 2005. The ice age methane budget, *Geophysical Research Letters* 32.

Van Santvoort, P., De Lange, G., Thomson, J., Cussen, H., Wilson, T., Krom, M., and Ströhle, K., 1996. Active post-depositional oxidation of the most recent sapropel (S1) in sediments of the eastern mediterranean sea. *Geochimica Et Cosmochimica Acta* 60, 4007-4024.

Veres, D., Bazin, L., Landais, A., Toyé Mahamadou Kele, H., Lemieux-Dudon, B., Parrenin, F., Martinerie, P., Blayo, E., Blunier, T., and Capron, E., 2013. The Antarctic ice core chronology (AICC2012): An optimized multi-parameter and multi-site dating approach for the last 120 thousand years. *Climate of the Past* 9, 1733-1748.

Waelbroeck, C., Skinner, L., Labeyrie, L., Duplessy, J., Michel, E., Vazquez Riveiros, N., Gherardi, J., and Dewilde, F., 2011. The timing of deglacial circulation changes in the Atlantic. *Paleoceanography* 26.

Walter, B.P., Heimann, M. and Matthews, E., 2001. Modeling modern methane emissions from natural wetlands: 1. Model description and results, *Journal of Geophysical Research* 106, 189-234.

Wang, W.-C., Yung, Y.L., Lacis, A.A., Mo, T. and Hansen, J.E., 1996. Greenhouse effects due to man-made perturbations of trace gases, *Science* 194, 685-690.

Wang, Y., Cheng, H., Edwards, R.L., Kong, X., Shao, X., Chen, S., Wu, J., Jiang, X., Wang, X., and An, Z., 2008. Millennial- and orbital-scale changes in the east Asian monsoon over the past 224,000 years. *Nature* 451, 1090-1093.

Wang, P., Tian, J., and Lourens, L. J. 2010. Obscuring of long eccentricity cyclicity in Pleistocene oceanic carbon isotope records. *Earth and Planetary Science Letters* 290, 319-330.

Weber, S.L, and Tuenter, E., 2011. The impact of varying ice sheets and greenhouse gases on the intensity and timing of boreal summer monsoons, *Quaternary Science Reviews 30*, 469-479.

Weber, S. L., Drury, A.J., Toonen, W.H.J. and van Weele, M., 2011. Wetland methane emissions during the Last Glacial Maximum estimated from PMIP2 simulations: Climate, vegetation, and geographic controls, *Journal of Geophysical Research* 115.

Wehausen, R. and Brumsack, H., 2000. Chemical cycles in Pliocene sapropel-bearing and sapropel-barren Eastern Mediterranean sediments. *Palaeogeography, Palaeoclimatology, Palaeoecology* 158, 325-352.

Weltje, G, de Boer, P. L., 1993. Astronomically induced paleoclimatic oscillations reflected in Pliocene turbidite deposits on Corfu (Greece): implications for the interpretation of higher order cyclicity in ancient turbidite systems. *Geology* 21, 307-310.

Whitlock C. and Bartlein, P.J., 1997. Vegetation and climate change in northwest America during the past 125 kyr, *Nature* 388, pp. 57-61.

Wolff, E.W., Fischer, H., Fundel, F., Ruth, U., Twarloh, B., Littot, G.C., Mulvaney, R., Röthlisberger, R., De Angelis, M., and Boutron, C.F., 2006. Southern ocean sea-ice extent, productivity and iron flux over the past eight glacial cycles. *Nature* 440, 491-496.

Wolff, E., Fischer, H., and Röthlisberger, R., 2009. Glacial terminations as southern warmings without northern control. *Nature Geoscience* 2, 206-209.

Wu, H., Guiot, J., Brewer, S. and Guo, Z., 2007. Climatic changes in Eurasia and Africa at the Last Glacial Maximum and mid-Holocene: Reconstruction from pollen data using inverse vegetation modeling, *Climate Dynamics* 29, 211-229.

Wüst, G., 1961. On the vertical circulation of the Mediterranean Sea. *Journal of Geophysical Research* 66, 3261-3271.

Ziegler, M., Tuenter, E., and Lourens, L.J., 2010. The precession phase of the boreal summer monsoon as viewed from the Eastern Mediterranean (ODP site 968). *Quaternary Science Reviews* 29, 1481-1490.

Samenvatting

In dit proefschrift analyseer ik veranderingen in het mondiale klimaat zowel als dat van de Mediterrane regio van de afgelopen 1.2-1.4 miljoen jaar. Hoewel er al veel onderzoek wordt gedaan en er op dit gebied al veel bekend is, valt er nog steeds een wereld te ontdekken wat betreft de oorzaken en het precieze verloop van de ijstijden en warme tijden die deze periode kenmerken. We weten sinds de publicaties van Milankovic dat de ijstijden worden beheerst door veranderingen in de baan van de aarde rond de zon. Met behulp van diepzee-sedimenten kunnen we de klimaatveranderingen proberen te reconstrueren, omdat de pakketten klei op de zeebodem een archief vormen van de dingen die jaar in, jaar uit van boven uit de waterkolom komen neerdwarrelen.

Met behulp van een massaspectrometer meten paleoklimatologen de samenstelling van foraminifera (eencellige organismen), of althans van de calciet in de minuscule schelpjes die ze achterlaten. De invloeden van temperatuur en zoutgehalte van het water veranderen de verhouding van isotopen in dit calciet (Emiliani, 1955), tussen de zware zuurstofisotoop ^{18}O, en de lichtere en veel vaker voorkomende isotoop ^{16}O. Ook de isotopenverhouding van het water zelf is belangrijk, als tijdens ijstijden significante hoeveelheden zoet water met relatief veel ^{16}O wordt opgeslagen op het vasteland, in de vorm van ijs. Dit alles wordt vastgelegd in de schelpjes van individuele forams: planktonische forams reflecteren de omstandigheden in de oceaan dicht onder de oppervlakte, waar ze leven. Benthonische forams reflecteren de diepere oceaan, waar de temperaturen en zoutgehalte minder veranderlijk zijn en het ijsvolume dus een relatief duidelijker signaal geeft (Shackleton, 1987). Nadat Hays et al. (1976) de theorie van Milankovic definitief bewezen door aan te tonen dat de veranderingen in isotopen inderdaad samenhingen met veranderingen in de baan van de aarde (de zgn. Milankovic-cycli), is door achtereenvolgend werk (Imbrie&Imbrie, 1980; de voornoemde Shackleton, 1987 en ook 1995; Lisiecki&Raymo, 2005: allen grote namen in dit vakgebied) steeds meer duidelijk geworden over het precieze hoe en waarom van de ijstijden.

Een problematisch aspect aan deze praktijk is dat de samenhang tussen isotopenveranderingen (klimaatveranderingen) worden verklaard door middel van Milankovic-cycli, maar dat hun leeftijd wordt geschat door ze te vergelijken met diezelfde cycli: er is geen betere manier voorhanden om een leeftijdsmodel op te stellen (d.w.z., de verhouding bepalen tussen de diepte van de sedimenten en hun ouderdom). Dus hoewel ondersteunende informatie (magnetostratigrafie, radiometrische meetpunten) de Milankovic-theorie bevestigt, berust het kader van isotopenstratigrafie deels op een cirkelredenering. Er is geen goede, nauwkeurige methode waarop we leeftijdsmodellen voor onze diepzeekernen kunnen opstellen behalve de isotopen, en daarom is er geen goede manier waarop we onze aannames kunnen testen over de samenhang tussen klimaatveranderingen en de astronomische cycli van Milankovic.

Met mijn onderzoek naar de sedimenten van enkele kernen uit het Middellandse Zeegebied (boorlocaties 967 en 968 van het Ocean Drilling Program) hoop ik een bijdrage te leveren aan dit vraagstuk. De dataset is uniek, omdat er nog nooit een studie is gepubliceerd naar benthonische isotopen in hoge resolutie uit dit gebied. Daarnaast heb ik ook gekeken naar planktonische isotopen, en naar de chemische samenstelling van het sediment. Met behulp van dat laatste probeer ik een leeftijdsmodel voor de dataset te creëren dat onafhankelijk is van de isotopen die ik gemeten heb. Ik baseer dat op de ratio tussen twee elementen (titanium en aluminium), die indicatief is voor de activiteit van de moesson op het nabije Noord-Afrikaanse continent (Lourens et al., 2001). Aangezien de kracht van de moesson sterk afhangt van m.n. de precessiecyclus (een Milankovic-

component), kan ik hiermee de precisie van de astronomische leeftijdsmodellen bereiken zonder daarvoor een beroep te hoeven doen op de isotopen die ik gemeten heb. Allicht doe ik hiermee zelf ook aannames over de respons van het Afrikaanse klimaat op de astronomische cycli. Maar dit zijn andere aannames dan die van de bestaande leeftijdsmodellen. Daarmee vormt dit onderzoek een basis om de bestaande leeftijdsmodellen voor isotopenveranderingen (en dus de ijstijden) te toetsen door middel van mijn eigen leeftijdsmodel en de gemeten isotopendata uit de Middellandse Zee.

In hoofdstuk 2 beschrijf ik hoe ik uit de twee verschillende boorlocaties (ODP 967 en 968) één samenhangende dataset heb gemaakt. Ik beschrijf in detail het opzetten van een leeftijdsmodel door de Ti/Al gegevens te correleren aan de precessiecyclus. Ik leg uit hoe het verwijderen van turbidieten (sedimentologische verstoringen) uit de dataset in zijn werk gaat. Daarna ga ik in op sapropelen, een belangrijk regionaal fenomeen waar veel over geschreven is binnen de paleoklimatologie. Het nieuwe leeftijdsmodel zet ook dit verschijnsel in een nieuw licht. In dit hoofdstuk blijkt dat sapropelen, in tegenstelling tot de heersende opvatting onder wetenschappers, geen constante reactiesnelheid hebben op de veranderingen in de aardbaan (de Milankovic-cycli). Bovendien toon ik aan dat, bij het ontbreken van sapropelen, overige methodes zoals kleurenpatronen in de boorkern een nog minder betrouwbare bron zijn om leeftijdsmodellen op te baseren.

In hoofdstuk drie presenteer ik onze benthonische isotopendata van de laatste 1.2 miljoen jaar. Ik vergelijk onze data met de LR04 dataset (Lisiecki&Raymo, 2005), die toonaangevend is voor paleoklimatologisch werk uit de Atlantische, Indische, en Stille Oceanen. Ik analyseer de verschillen tussen de schattingen op basis van mijn leeftijdsmodel met die van hen, die gebaseerd zijn op directe correlatie met de Milankovic-cycli. Ik bediscussieer ook de aannames in mijn leeftijdsmodel, en de onzekerheden rond isotopendata uit de Middellandse Zee. Uit de resultaten blijkt dat enkele overgangen flink bijgesteld zouden moeten worden, aannemende dat de Mediterrane gegevens geloofd mogen worden.

In hoofdstuk vier ga ik kort in op de lokale invloeden op onze isotopendata en hoe het signaal van het snelle afsmelten van de laatste ijstijd (±10.000 jaar geleden) in de Middellandse Zee eruit ziet. Ik vergelijk onze benthonische isotopendata met een andere dataset die van een nabije, ondiepere locatie afkomstig is met een andere watersamenstelling, en met gegevens van verschillende locaties uit de overige oceanen van de Aarde. Hierbij richt ik me in het bijzonder op de vraag of het signaal in de Middellandse Zee er hetzelfde uitziet als in de overige oceanen; met andere woorden, of ik de verschillende datasets wel één op één met elkaar mag vergelijken. De verschillen blijken zeer mee te vallen, vooral in het licht van de observatie dat de verschillen wereldwijd groter zijn dan men op basis van het werk van Lisiecki&Raymo (2005) zou vermoeden.

In hoofdstuk vijf presenteer ik een herziene versie van de planktonische dataset MedStack: een compilatie van verschillende bronnen van planktonische isotopendata uit de Mediterrane regio. In de nieuwe versie is de data afkomstig uit ODP 967 en 968 toegevoegd en het leeftijdsmodel herzien op grond van de schattingen in hoofdstuk twee. Ik gebruik deze nieuwe en verbeterde dataset om schattingen te doen over het zoutgehalte in het water aan de oppervlakte van de Middellandse Zee. Dit is van groot belang voor de vorming van sapropelen, waar ik mijn isotopische meetgegevens dan ook op betrek. In dit hoofdstuk komen de verschillende databronnen – benthonische en planktonische isotopen, geochemische analyses, sapropelen – en hun onderlinge samenhang bij elkaar.

In hoofdstuk zes presenteer ik de uitkomsten van een studie die ik heb gedaan met behulp van klimaatmodellen. Dit hoofdstuk staat enigszins los van de andere omdat het werk is wat ik tijdens

mijn afstudeerstage op het KNMI deed, en het als enige gebruik maakt van klimaatmodelleren. Het hangt wel samen met de rest van het proefschrift omdat het ingaat op vragen naar de activiteit van de moessons in reactie op Milankovic-cycli. In deze studie gebruik ik de uitdraai van het model CLIMBER-2, dat een robuust model is hoewel de resolutie erg laag ligt. Omdat moessons zulke grootschalige fenomenen zijn, worden ze door CLIMBER goed nagebootst ondanks het feit dat de Middellandse Zee binnen een enkele grid cell valt (Braconnot, 2007). Het voordeel van de lage resolutie is dat honderdduizenden jaren aan klimaatverandering kunnen worden gesimuleerd zonder een supercomputer nodig te hebben om het door te rekenen.

Ik gebruik het gesimuleerde klimaat van CLIMBER als input voor een eigen programma om de uitstoot van het sterke broeikasgas methaan (CH_4) te modelleren. Mijn model bootst na hoe het klimaat de hoeveelheid 'wetlands' beïnvloedt: natte en drassige gebieden, zoals veen, waar veel plantenmateriaal in groeit om vervolgens na afsterven van de plant onder water te worden verteerd. Bij deze anaërobe processen (verteerprocessen waar geen lucht bij komt) wordt door bacteriën CH_4 geproduceerd, afhankelijk van de temperatuur, het natte areaal, en de hoeveelheid beschikbaar plantaardig materiaal. Het model simuleert deze CH_4-uitstoot, waarna ik de uitkomsten vergelijk met atmosferische concentraties zoals die zijn gemeten aan luchtbelletjes in het eeuwenoude Antarctische ijs. Deze resultaten zijn zeer bevredigend, en ik gebruik de uitkomsten van het model vervolgens om te analyseren of het bulk van de CH_4-uitstoot voortkomt uit de koelere noordelijke regionen (Toendra's) dan wel de warmere moessongebieden in de tropen.

Acknowledgements

God knows one cannot do a PhD on their own. Many people deserve credit for helping me the last years, more than I can mention in this short section, the most-read part of the thesis. Let alone do them justice with mere words on paper. Nevertheless, I will do some of them the courtesy of expressing my profound gratitude. Luc, you have it for granting me the chance to do this PhD, for your guidance as a supervisor and help in the research and the writing, for pointing out interesting questions and issues to explore, and for the freedom to do something else instead. Martin, you were there to help, despite your busy life with family, migrating back to the Netherlands, and the many international projects that you are involved in. I thank you for your coaching, your vital input and expertise, and your reflections on how to deal with difficult situations. I thank Nanne Weber, whom I remember as a sharp-minded but warm, involved supervisor despite everything during my time at the KNMI, and who set me on the path to do this research.

I would like to thank my colleagues, for many great and stimulating conversations on a great many topics: Frits, Wilma, Hemmo, Ivo, Antonio, Christian, Hans, Anneke, Jan, Jan-Willem, and everyone visiting the 3rd floor NE coffee corner. Also, no lab in the world would function without people who actually know what they are doing, to run them. So I owe a lot to Arnold, Dominica, Geert, Jan, Rob, Ton, and Otto, for patiently explaining what to do and what not to do, and for making everything better when things were bad. This is very much true also for Marjolein, who is always helpful and cheerful, and who facilitates so much of the department that one wonders how she gets it all done in just the 24 hours of any given day.

Students, Arno, Simon, Malou, Robin, Shaun, Joep, and collaborators, who contributed to the research and the writing with data, ideas, and suggestions. The running group, with Anne, Mathilde, Paul, José, Rick, Tom, and many more, who provided a welcome outlet when my mind was tired and my muscles atrophied. My fellow PhD students, Stefanie, Cindy, Maria, whom I will fondly remember working alongside with. Helen and Vittoria especially, my paranymphs, who shared an office with me for four years as well as bits of interesting gossip now and then, and whom I secretly feared would each finish their PhD's well before me because they are so much brighter and work so much harder. (That goes for you too, Stef, but with you I had a much safer head start). Thank you for the good memories of times we were celebrating, and for commiserating when times were rough. And Margreet, the tea/coffee buddy I loved to hang out with most of all: thank you for saving me from work all those hours.

Lastly, I would like to thank those who form the basis for my existence and who are the giants on whose shoulders I lean. My family, my mother Christine, my sister Lianne, my brother Sean, and my love Anne. Thank you for being there.